Dissertation

submitted to the
Combined Faculties for the Natural Sciences and for Mathematics
of the Ruperto-Carola University of Heidelberg, Germany
for the degree of
Doctor of Natural Sciences

presented by

Diplom Physicist Dániel Apai
Born in: Szeged, Hungary

Oral examination: 26th May 2004

Exploring the Environment of Young Stars: Disks, Companions and Clusters

Referees: **Prof. Dr. Thomas Henning**
Prof. Dr. Matthias Bartelmann

Abstract

This thesis aims to further our understanding in four important, strongly related topics of star formation: Disk evolution, stellar multiplicity, FU Ori phenomenon and the formation of massive stars. The main results are the following: 1. By applying the novel method of polarimetric differential imaging and the NACO/VLT instrument we probe one of the closest circumstellar disks in the planet-forming age at scales of our inner Solar System. 2. Our adaptive optics survey discovers six companion candidates to young stars. The most interesting one is close to the well-known outburst star FU Ori and is a good candidate for being the outburst trigger. 3. We identify the second-closest cluster of young stars around the intermediate-mass star HD 104237, with at least three of them showing signs of disks. 4. The first global picture on the prototypical massive star-forming region IRAS 09002-4732 is provided and its stellar content, reflection nebula, compact H II region and globular dust filaments are analysed. 5. The first multi-epoch radial velocity survey of very young, embedded massive stars is presented. Two massive close binary stars are identified. The radial velocity measurements show large differences explainable only if substantial fraction of the young massive stars are close binaries. This high intrinsic binarity rate is naturally explained by the coalescence-type formation of massive stars.

Zusammenfassung

Diese Arbeit hat die Erweiterung unseres Verständisses in vier wichtigen, eng verwandten Themenbereichen der galaktischen Sternentstehung zum Ziel: Entwicklung von Akkretionsscheiben, Mehrfachsternsysteme, FU Ori-Phänomene und die Entstehung massereicher Sterne. Die wesentlichen Ergebnisse der Arbeit sind: 1. Durch die Anwendung der neuen Methode differentieller polarimetrischer Abbildungen konnten jene Teile der nächstgelegenen zirkumstellaren Scheiben beobachtete werden, deren aufgelöste Skalenlänge derjenigen unseres inneren Sonnensystems entsprechen. 2. Bei einer Durchmusterung mit Hilfe von adaptiver Optik wurden sechs Objekte gefunden, die wahrscheinlich Begleiter junger Sterne sind. Der interessanteste dieser Kandidaten befindet sich bei dem bekannten "Ausbruch"-Objekt FU Ori. Der neugefunden Begleiter stellt vermutlich den Auslöser dieser Ausbrüche dar. 3. In der Umgebung von HD 104237 wurde der zweit-nächstgelegene Haufen junger Sterne identifiziert. Mindestens drei Haufenmitglieder zeigen Anzeichen einer zirkumstellaren Scheibe. 4. Zum ersten mal wird ein umfassendes Bild der prototypischen Sternentstehungsregion IRAS 09002-4732 gezeichnet. Dabei werden die enthaltenen Sterne ebenso analysiert wie der Reflektionsnebel, das kompakte HII-Gebiet und die ausgedehnten Staubfilamente. 5. Es wird die erste multi-epochalen Radialgeschwindigkeitsdurchmusterung sehr junger, eingebetteter massereicher Sterne vorgestellt. Hierbei konnten zwei enge, massereiche Doppelsysteme identifiziert werden. Große Radialgeschwindigkeitsschwankungen vieles Systeme weisen daraufhin, daß ein beträchtlicher Teil der massereichen jungen Sterne engen Doppelsystemen angehört. Dies könnte sich unkompliziert aus dem Szenario der "Koaleszenz"-Entstehung massereicher Sterne ergeben.

Contents

Acknowledgement

Chapter 1

Introduction

From the earliest times on man sought answers to some apparently simple questions: *What are stars and planets? What is their influence on our life? How were they formed or created? What is their future?* The advances during the last two centuries led us to understand the nature and evolution of the stars, and ultimately their final fate. However, their origin together with the related question of planet formation remains probably the last major unexplored question of galactic astronomy.

What hinders our understanding here is that the rapid process of stellar birth remains hidden in the depth of light-obscuring dark clouds of dust and gas – the same material from which the stars form. Understanding the formation process requires looking into these stellar cradles, which was for long time outside the capabilities of the astronomical instrumentation.

The new generation of instruments working at infrared and radio wavelength regimes, as well the x-ray detectors provided the means to observe the new-born stars dimmed by their natal clouds. However, the stellar birth turned out to be a much more complex and dynamic process than expected beforehand and is still beyond our complete understanding. The last decade and the coming years brought and will bring powerful new instruments and detailed computer simulations to clarify the open questions of star formation.

This thesis presents results from some of the newest instruments and techniques which pushed further the current observational limits in an attempt to answer some of the major open questions of star formation. Before moving to the first part of the work we summarize here our current concept of star formation, discuss the main open questions and briefly overview the goals of the thesis.

1.1 Formation of Stars: The Current Picture

The modern picture of star formation has been developed gradually in the second half of the 20th century, largely as the result of the revolution in the radio and infrared instrumentation. The observations demonstrated that low-mass stars form in a less complex environments than the massive ones and therefore our current star formation picture is

based low-mass objects.
The current paradigm of low-mass stellar birth starts with a giant molecular cloud, in which the thermal and gravitational instabilities form dense and compact cloud cores (Elmegreen 1991). The cores contract and evolve quasi-statically into a $1/r^2$ density configuration over timescales in the order of $\sim 10^6$ yr Shu (1991). This density distribution remains through the quasi-static contraction of the cloud core (see Fig.1.1 for an illustration). The quasi-static contraction continues until the central concentration becomes sufficiently high and a rapid inside-out collapse takes place. The infall wave propagates outward at the local sound speed, while the collapsing core maintains a self-similar density profile (Shu 1977). This isothermal infall continues, until the central regime becomes optically thick. As thermal timescales of the protostar exceeds the sound crossing time, the runaway increase of the central density is halted. The Kelvin-Helmholtz timescale, on which the protostar reaches the internal thermal equilibrium, is proportional to the square of the protostar's mass $\sim GM_*^2/R_*L_*$. For low-mass stars ($M_* < 3M_*$) the Kelvin-Helmholtz timescale exceeds the typical accretion timescales and therefore they often end their accretion before reaching the main sequence (see Fig. 1.1). In contrast, massive protostars quickly reach the main sequence, while still accreting mass from the infalling envelope.

1.2 Caveats and Challenges

In spite of the general success of the star formation model described above and the substantial effort put in this field during the recent decade, we can not yet answer some of the fundamental questions of the star formation process. We list here the most important ones:
1. Angular momentum problem, outflows and jets: The simple contraction of a typical molecular cloud core with a diameter of $\sim$ 0.1 pc into a few Solar radii sphere results in a body spinning a factor of $\sim 10^{13}$ times faster than its original rotation rate. For any realistic set of initial parameters such a rapid rotation would break up the star. Accretion through a disk, however, allows loss of angular momentum from the system while transporting most of the mass inwards if an effective viscosity is present (see, e.g. Lynden-Bell and Pringle 1974). The nature and the properties of this viscosity is not yet well understood. An additional way of the system to expel angular momentum can be via high velocity outflows and jets observed from protostars and young stellar objects, but the physical process driving these outflows has not yet been unambiguously identified (Bachiller 1996; Reipurth and Bally 2001).
2. Accretion rates & FU Ori objects: Several independent line of evidence prove that the star formation – even low-mass star formation – happens rapidly on a time scale of 10^5 years. However, recent measurements of the mass accretion rates find typical values of 10^{-7}–10^{-10} $M_\odot$/yr in the Orion high-mass star forming region (Robberto et al. 2003) and 10^{-8} $M_\odot$ in the Large Magellanic Cloud (Romaniello et al. 2004). At this rates, the formation of a typical Solar-type star would take at least a hundred times longer than observed. The conclusion that the quiescent accretion process is occasionally interrupted

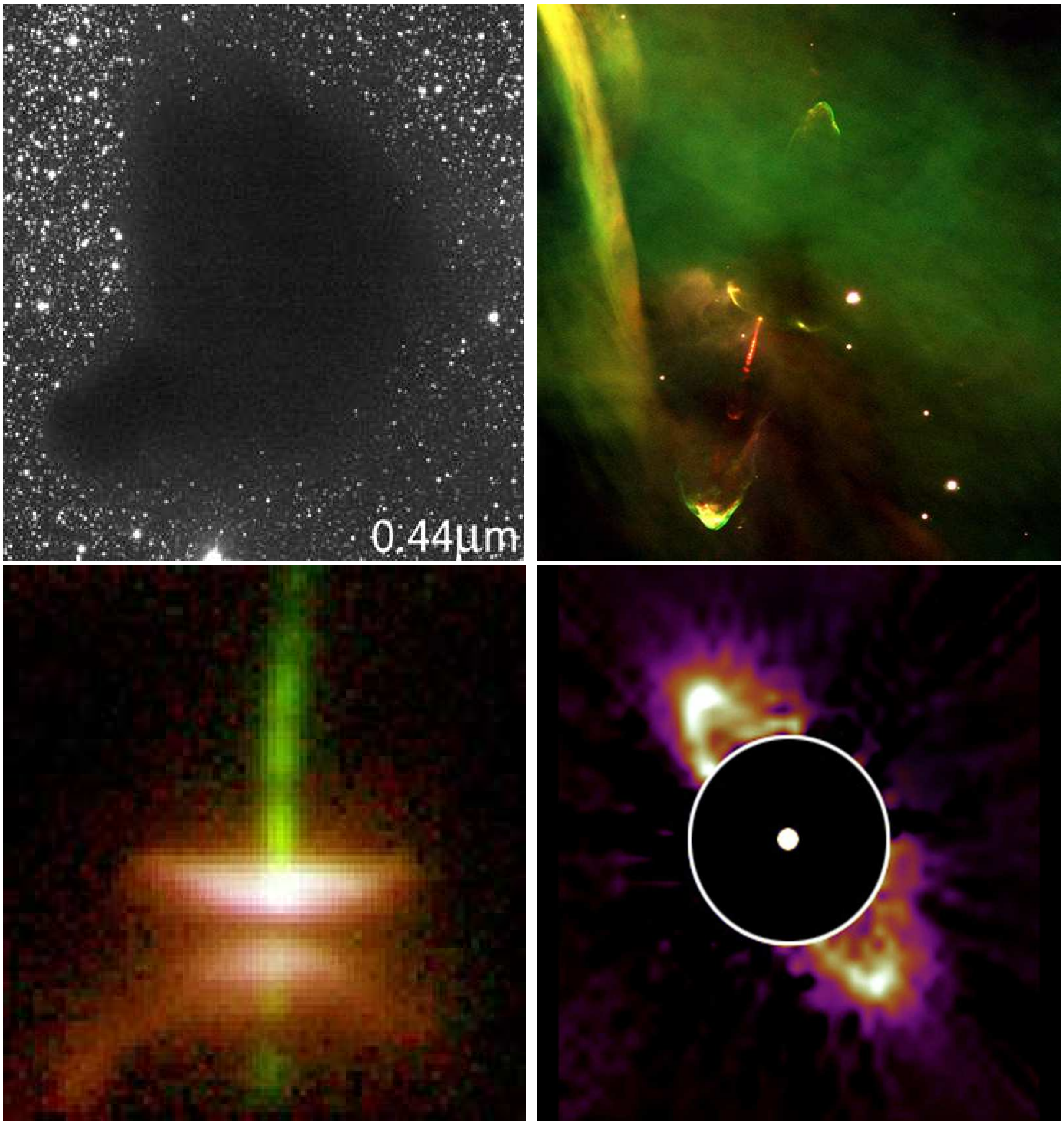

Figure 1.1: Illustration of the main phases of stellar birth. *Upper left:* The silhouette of the dark cloud B68 believed to be on the verge of gravitational collapse (Alves et al. 2001). *Upper right:* Protostar candidate HH-34 marked by its jet in the Orion star-forming region (ESO-PR 40/99). *Lower left:* HH30, a young accreting star occulted by its own edge-on circumstellar disk (Courtesy of C. Burrows). *Lower Right:* Coronographic image of the debris disk around the main sequence Vega-type star HR4796A replenished by collisional cascades of primitive minor bodies (Schneider et al. 1999).

by short episodes of intense mass accretion, seems inescapable. The best candidates for such ongoing events are the FU Ori objects which underwent recent outbursts, believed to be the results of run-away accretion rates (for a review, see Hartmann and Kenyon 1996).

2. Binaries, multiplicity and clustering: While the natural results of the simplified model based on self-similar spherical collapse are single stars, the majority of the observed stars is member of a binary or higher-order multiple stellar system (Duquennoy et al. 1991; Duquennoy and Mayor 1991). The fact, that young stars are preferably found in associations or open clusters indicates that not only multiplicity but also clustering are intrinsic properties of the star formation process. These characteristics are even more pronounced for young massive stars, which can always be found in star-forming region or in OB-associations, with the exception of the very few run-away stars (see, e.g. Gies 1987). The formation of binary/multiple stars and stellar clusters is a fundamentally important, yet poorly understood question which puts strong constraints on the different the star formation scenarios.

3. Initial Mass Function: Numerous deep, comparative studies of different star-forming environments and young clusters aimed to derive the relative number of stars with different masses (for a review, see Meyer et al. 2000). These works proved that the general shape of the initial mass function is similar in different galactic star-forming regions. However, currently it is still strongly disputed if the initial mass function is identical at every regions of star formation. We do not yet know which, if any, parameters determine its exact shape or the upper and lower mass stellar limits.

A successful star formation model must also reproduce the observed initial mass function, as this plays a crucial role in several fields of astrophysics, from the abundance of substellar objects through starburst clusters to the total mass of galaxies.

5. Formation of massive stars: The accreting high-mass protostars rapidly reach the main sequence and emit enormous amount of radiation. Spherically symmetric calculations show that the strong radiation pressure can reverse the gravitational collapse of the envelope and efficiently halt the accretion process (Wolfire and Cassinelli 1987) when the star reaches the mass of 8-10 $M_{\odot}$. Simulations of more complicated configurations found the same basic problem (Yorke and Bodenheimer 1999). Although several scenarios have been suggested to overcome this problem, the field is strongly limited by the available observations: we have insufficient data on the evolution and properties of massive protostars and on the characteristics of the youngest massive stars.

Because of the profound impact massive stars have on their environment via their ultraviolet flux, stellar winds and heavier elements, understanding their formations in the Milky Way is an important step in improving our picture on the evolution of galaxies and the global star formation history.

6. Star formation history, Induced Star Formation and Starburst clusters: Star formation in other galaxies often happens on spatial and mass scales thousands times larger than what is observable in the "quiescent" Milky Way. Clusters concentrating thousands or tens of thousands of massive stars in a few cubic parsecs are known as starburst clusters. The abundance of the short-living massive stars proves that the star formation occurred rapidly, almost instantenously in the region. Such a process could be expected if the

formation of massive stars would induce star formation in the neighboring cloud cores. The idea of star formation "waves" proceeding through the giant molecular clouds is very attractive but still disputed (e.g. Chernin et al. 1995).
7. Disk Evolution and Birth of Planetary Systems: Observations of the infrared excess emission of young stars showed that the typical lifetime of circumstellar disks observable in the infrared is between 3 and 10 Myr (Brandner et al. 2000; Spangler et al. 2001; Zuckerman 2001). Several effects are expected to contribute to the "disruption" or disappearance of the optical/infrared disks, including the radiation pressure, photoevaporation, accretion and the coagulation and growth of dust grains. This latter process is believed to lead to the formation of planets (Lissauer 1993; Blum et al. 2000). Strongly disputed aspects are the fate of the gas content of the disks, the timescales and the efficiency of planet formation.

Answering these strongly related questions requires substantial effort from the astronomical community: not only new observations, but new instruments, simulations and methods are necessary. However, resolving these problems will also lead us toward a new star formation model, which can account for star formation on global scales, taking the stellar environment and multiplicity into account. Understanding the first million years of the circumstellar disk's evolution explains also the planet formation process.

1.3 Scientific Goals

The goal of this thesis is to observationally deepen our understanding in the four strongly related topics of disk evolution, stellar multiplicity, FU Ori phenomenon and the formation of massive stars.
The subsequent chapters investigate young stellar objects with increasing masses exploring their circumstellar material and the presence of companions. As the stellar mass increases the objects are more and more often found to be part of a multiple system.
In the second chapter we present observations of the disk around the closest low-mass young star TW Hya, which is believed to be in the planet-forming stage. The question here is the presence of disk structures (gaps, inner truncation) gravitationally induced by a possible planet-mass companion.
The third chapter mainly studies the environment of the Herbig AeBe stars, the intermediate-mass young stars. We describe our high-resolution observations discovering previously unknown stellar companion candidates to many of our targets. Detection of a companion to the star FU Ori itself, as well as the study of the newly discovered cluster around the Herbig Ae star HD 104237 is discussed.
In the fourth chapter we step from the A-type star to O-type stars and describe the multi-wavelength study of the dense and compact cluster and intracluster material that surrounds these massive stars. We show the massive stars' influence on the intracluster dust and gas.
The extreme stellar densities in compact clusters around the massive stars inspires the first multi-epoch spectroscopic search for massive binaries, which is described in the fifth

chapter. The presence and rate of close binaries among high-mass stars provides a crucial hint on their much debated formation.

Finally, the summary of the work is given highlighting the most important results.

Chapter 2

The Disk of the Low-mass Star TW Hya

Circumstellar disks are necessary for young low-mass stars to overcome the angular momentum problem linked to mass accretion, as it is also discussed in Chapter 1. The disk structure and its evolution into planetary systems is an exciting problem at the edge of the actual observational capabilities. In this chapter we will use one of the best ground-based facilities to study the closest disk in the planet-forming stage aiming to search for planet-induced disk signatures predicted by hydrodynamic simulations of disks: Gaps are being opened and shock waves follow the path of the orbiting Jupiter-mass body embedded in viscous disks (see, e.g. D'Angelo et al. 2003). Detecting these signatures is an important step in confirming that our models for planet formation and disk evolution are right and would provide a unique possibility to study a newly formed exoplanet and its interaction with the circumstellar material.

However, the investigations of protoplanetary disks require high-contrast, high-spatial-resolution imaging very close to the bright central star. Although in recent years numerous groups studied disks around nearby stars at their planet-forming age with the HST, instrumental limitations do not allow to probe the disk structure at scales similar to our inner Solar System. The technique of polarimetric differential imaging (PDI) as described by Kuhn et al. (2001) is capable of tracing scattered (i.e. polarized) light from a circumstellar disk very close to the central star. This promising method enhances the contrast between the disk and the star and, thereby, might be important to detect the detailed inner structure of protoplanetary disks.

The basic idea of the PDI is to take the difference of two orthogonally polarized, simultaneously acquired images of the same object in order to remove all non-polarized light components. The non-polarized light consists mainly of the central star's light and the speckle noise, which is – close to the star – the dominant noise source of ground-based observations at optical and near-infrared wavelengths (Racine et al. 1999). After this subtraction only the polarized light, such as scattered light from the disk, is left over.

To explore the potential of this technique for planet formation studies as well as to demonstrate the NACO/VLT platform capabilities we targeted the 8 Myr old (Webb et al. 1999) and very close (56 ± 7 pc, Wichmann et al. 1998) classical T Tauri star TW Hya (RA: $11^{\mathrm{h}}01^{\mathrm{m}}51.9^{\mathrm{s}}$ Dec:$-34°42'17''$ J2000). At the visual wavelength regime TW Hya shows a polarization variability between 0-3% (Mekkaden 1998). Being an excellent target for planet formation studies, during the past few years several attempts have been made to image its disk as close as possible to the star and to identify possible disk structures (Krist et al. 2000; Weinberger et al. 2002). In addition, the presence of a giant planet was predicted (Calvet et al. 2002) from modeling the spectral energy distribution (SED) (see also Steinacker and Henning 2003). The first application of the PDI to TW Hya by Potter (2003a,b) made use of the 36 element curvature sensing Adaptive Optics (AO) system Hokupa'a (Graves et al. 2000), of the Gemini North telescope. This H-band data set probed the circumstellar material closer than $0.5''$to the star.

In the following we describe the first results obtained with the PDI technique and the 188 element Shack-Hartmann AO system NACO, which is attached to the Nasmyth B port of the VLT UT4.

2.1 Observations and Data Reduction

2.1.1 NACO Observations

The observations were carried out in April 2002 during the commissioning of the NACO/VLT system (Mekkaden 1998; Rousset et al. 2003; Hartung et al. 2000) in the Ks band. In order to simultaneously measure two orthogonal components of the polarized light, a Wollaston prism was introduced in the light path. The Wollaston prism splits the light into an ordinary and an extraordinary beam (*o*- and *e*-beam), separated by $3.5''$ in the Ks-band. To eliminate the instrumental polarization and to increase the signal-to-noise ratio (SNR) of the data, a redundant data set with Wollaston angles of 0°, 45°, 90° and 135° was acquired. Each of these images has a field of view (FOV) of $3'' \times 29.4''$ sampled with a pixel size of $0.027''$/pixel. At every Wollaston position a 3-point dithering was applied with steps of about $9''$ along the field of view to allow sky subtraction and to reduce the influence of bad pixels. No additional off-source sky frames were taken.

To ensure the high dynamic range needed for disk analysis, we repeated the complete set of these observations with defined integration times of 0.4 s and 30 s. The total time spent on the source was 24 s and 1800 s in the short and long exposure series, respectively. As the TW Hya saturated the detector, the AO-performance can not be accurately measured. However, based on simulations with the NAOS Preparation Software v1.62 we estimate a typical Strehl-ratio of 50% for these observations.

2.1.2 Data Reduction

The data reduction was carried out using self–developed IDL routines. First, every frame was manually inspected and those showing reflections or electronic ghosts were excluded from further reduction. Hot pixels were efficiently removed by a 3.5-sigma filtering process.

The raw images were sky subtracted and flat field corrected. The sky frame was calculated individually for each group of images taken with the same polarization angle. Following these basic corrections, the ordinary and extraordinary peaks of the individual exposures were centered and extracted. To remove all of the non-polarized intensity (mainly from the central star) we subtracted images of ordinary polarization from those of extraordinary polarization. The fine alignment of the individual images before subtraction and co-addition was carried out by a two-level Gaussian fitting procedure (see also Section 2.4).

The subtraction process gives the orthogonal Q_i and U_i Stokes components, i standing for the number of dithering positions. For the 4 angles of the Wollaston prism we thus derived the values for Q_i^0, U_i^{45}, Q_i^{90} and U_i^{135} (see, e.g. Huard 1997). Using the redundancy of our data set we derived the Q and U mean polarization vectors:

$$Q = \sum_{i=1}^{3} \frac{(Q_i^0 - Q_i^{90})}{2} \quad \text{and} \quad U = \sum_{i=1}^{3} \frac{(U_i^{45} - U_i^{135})}{2}$$

and the polarized intensity:

$$PI = \sqrt{\frac{Q^2 + U^2}{2}}.$$

This reduction procedure was repeated independently on both the long and the short exposure series, resulting in the PI_{Short} and PI_{Long} polarized intensity maps.

Due to the brightness of TW Hya, the inner regions of the raw frames exceeded the regime of linear detector response. These data points ($r < 0.06''$ in the short exposure series and $r < 0.45''$ in the long exposure series) were excluded from the data reduction and further analysis. The field of view (FOV) was limited to $\sim 3''$ by the field mask. During the dithering process slight movements perpendicular to the dithering directions occurred. Since the resulting FOV is the intersection of the FOVs of the individual frames, the final field of view was reduced to $\sim 0.54''$ and $\sim 1.43''$ for the short and long exposure series, respectively.

To characterize the surface brightness distribution of the disk we measured the radial profile of the polarized intensity, derived from 3-pixel-wide apertures, roughly equivalent to the full width at half maximum (FWHM) of the point spread function (PSF).

2.2 The Hydra Pipeline

The data reduction described above was carried out by the self-developed IDL-pipeline *Hydra*. In the following we describe some technical details of the pipeline and the IDL environment, while in the next section we discuss the principles of the signal analysis.

We developed the *Hydra* pipeline with the goal to have an easily reconfigurable, robust reduction tool for differential polarimetric work. The pipeline uses external configuration files to set all relevant parameters. Several alternative methods are included for most of the reduction steps, which also proved to be very important for the tests of the pipeline.

The main *Hydra* script allows two levels of data reduction: First, the basic reduction of the raw frames for each data set for each combination of the object, Wollaston prism angle and exposure times. The second level combines the prepared P_i and Q_i images into the final P, Q and PI images. In the flow chart in Fig. 2.1 we show the concept of the *Hydra* script.

Every raw frame first enters into a basic reduction process which carries out the bad pixel removal, truncation of non-linear pixels, sky subtraction and flat field correction. The sky frame is constructed by taking the minimum of the pixels for a given data set. The next step is finding the two beams separated by the Wollaston prism. The ordinary and extraordinary beams are then extracted in the form of rectangular subimages from each science frame. The inner, saturated regions can optionally be masked out at this point. Before differencing the beams of orthogonal polarization, the most critical step of the pipeline (see below) is executed, namely the re-centering. The pipeline provides several combinations of two-dimensional Gaussian fitting and cross-correlations in order to align the beams to the highest possible accuracy. Optionally resampling of the images is possible to reduce the loss of information from sub-pixel shifts and image rotations. After the alignment, the extraordinary beams are subtracted from the extraordinary ones and then combined. The resulting Q_i and P_i images are rotated according to the position angle FITS keyword to reconstruct their celestial orientation. As the final step of the first level the rotated images are saved in the directory of the intermediate results.

The second level of *Hydra* is separately launchable to spare the significant processor time necessary for accomplishing the first level. If the intermediate results are already calculated, they are loaded. The main function of the second level is to combine the intermediate and already aligned images. This combination is carried out according to the principles described above. At this point any images manually flagged for rejection are excluded from the combination and further data reduction. In the first step the images are averaged into the Q and U polarization components and then the polarization intensity image is calculated.

Several other scripts are used to build a running environment for the main script and to provide further analytical functions. The script *Headmaster* is the highest-level program that executes the *Hydra* script for each of the four data sets. After the completion of the data reduction the *Headmaster* script launches the data analysis scripts described below, such as *SSAT*, *pltord*, and also creates the relevant figures and comparisons to the HST data.

Our data reduction uses two major methods to analyse the results: the radial polarization intensity plots constructed by the script *plotrd* and the *SSAT* tool for the inspection of the polarization components Q and U. *Plotrd* consists of a cycle azimuthally averaging the normalized intensity in increasing annuli around the chosen centre and plots it against the radius. By fitting a line on the logarithmically plotted results *plotrd* also derives the exponent of the power-law function approximating the surface brightness slope. This script builds strongly on the script *aper* of the *astrolib* IDL package. *Plotrd* also contains an option for internal validation by the injection of an artifical data set with known radial slope.

The *SSAT* script is a somewhat more complicated procedure which was developed especially for probing the polarization signal in this data set. It uses an angular masking and a distance masking script (*angmask* and *dist_circle*) to integrate the fluxes of the image in sectors of annuli. An example for its output is shown in the right panel of Fig. 2.2. The normalized intensity in the given bins is plotted against the angle between west and the given sector. The script also provides a possibility to compare the data with an expected (theoretical) distribution. The amplitude of the fitted curve, i.e. cosine can be compared to the standard deviation of the background pixels to characterize the signal strength in the images. Beside the above described scripts, several others have been developed and used as the environment for the *Hydra* pipeline.

After the assembly of the pipeline we ran extensive tests to probe the stability of the solutions and to understand the nature of potential artifacts. The structure and the configuration files allowed a well-documented and effective testing of the pipeline.

2.3 Signal Analysis

For detecting the polarization signal as close as possible to the star a very careful data inspection is essential – residuals from the subtractions as well as sub-pixel misalignments between the individual frames are the dominant noise sources. While the scalar PI image contains no information on the direction of the polarization, the Q- and U-components are projections of the polarization vector and thus show a sinusoidal modulation with the angle in respect to the polarization direction of the Wollaston-prism (i.e. a maximum at the angles parallel to the polarization direction of the Wollaston prism and a minimum perpendicular to it). In the case of axisymmetrically distributed dust this modulation leads to the *butterfly* pattern as shown in the right panel of Fig. 2.2 and described in Kuhn et al. (2001). By using the information about the polarization orientation and by comparing this pattern to what is expected from an axi-symmetric light scatterer, we can better discriminate between noise and signal.

The right panel of Fig. 2.2 shows the Q-component of the polarization signal radially integrated (over 5-degree bins) in an annulus between $0.75''$ and $1.0''$ from the long exposure series. A very similar, but $\pi/2$-shifted modulation is evident in the U-images. The clearly sinusoidal modulation arises from the strong polarization signal. When probing the extent of the polarized circumstellar material, we looked for the presence of a similar pattern (phase- and frequency-correct sinusoidal modulation) as a function of radial distance from TW Hya.

We found an extended polarization pattern with a high signal-to-noise ratio between 0.5 and $1.4''$ distance from the star in both the Q and U long exposure images. In the short exposure images we identified light-scattering material between $0.2''$ and $0.4''$ from TW Hya in both the Q- and U-components. Inspection of the higher signal-to-noise Q-component (short exposure) showed this pattern also between $0.1''$and $0.2''$ (see the left panel of Fig. 2.3).

In order to estimate the contrast ratio between the polarized and the unpolarized fluxes we compared the fluxes of the direct images (after sky subtraction and bad pixel removal)

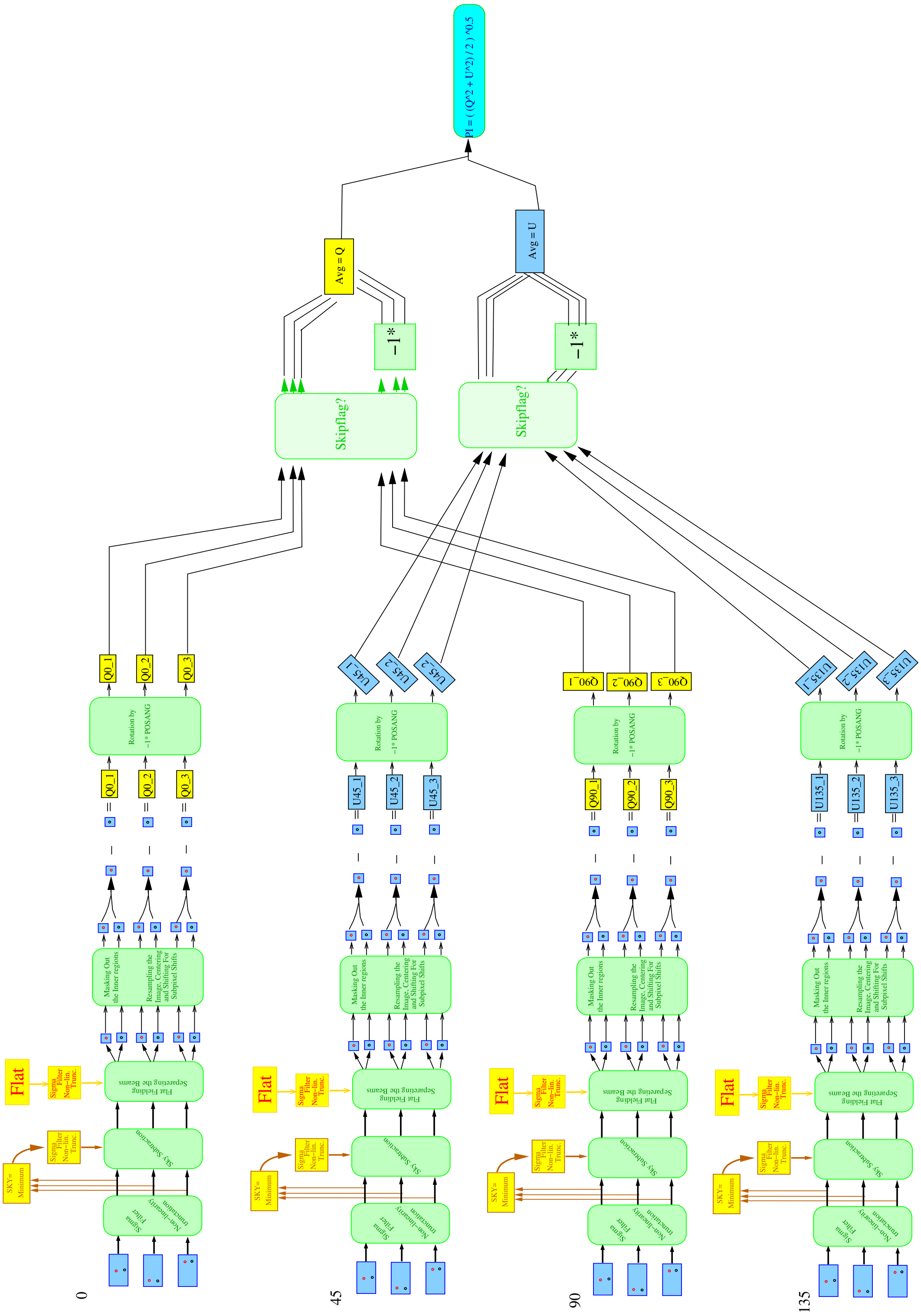

Figure 2.1: Flowchart illustrating the working principle of the Hydra pipeline.

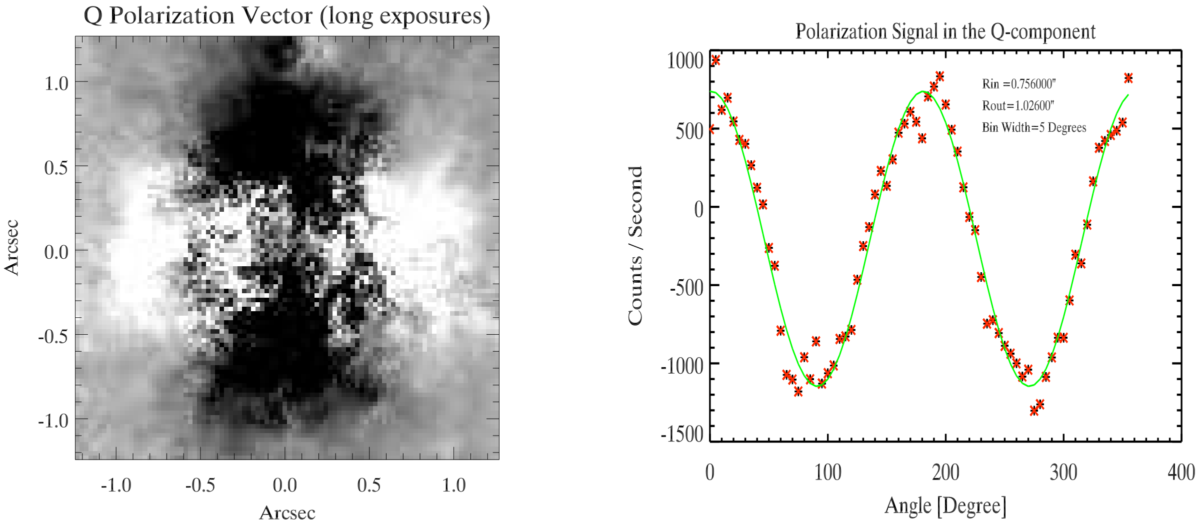

Figure 2.2: *Left panel:* The characteristic *butterfly* pattern of an extended polarized source around TW Hya in the Q_{Long} image. This pattern can be identified between $0.5''$ and $1.4''$ from the star on both the Q- and U (long exposure) images. The image is centered on TW Hya. *Right panel:* Counts in the Q-component of the polarization vector as a function of position angle in an annulus between $0.75''$ and $1''$ from the long exposure series. The asterisks mark the data points averaged over 5 degree bins, while the curve is the best fitting frequency-fixed cosine. The strong sinusoidal modulation indicates that the light-scattering dust is distributed nearly axisymmetrically around the light source.

to the amplitude of the fitted cosine. The typical contrast ratios are $F_{P/U}$ $\simeq$1% and $F_{P/U}$ $\simeq$3.5–4% for radii of $r = 0.1'' - 0.3''$ and $r \simeq 1''$, respectively.

2.4 Reliability Tests and Confirmation

To confirm our results, we analysed the Q- and U-components of the PDI data set of the PSF-comparison star GSC 07208-00319, which was observed and reduced in an identical way to the TW Hya data set. In this case neither polarized emission in the PI image nor any sign of sinusoidal modulation in the Q- and U-band images could be found (see right panel of Fig. 2.4).

We also conducted extensive tests to check the reliability of our data reduction and analysis toolkit. During these test runs the effects of the following errors were investigated: sub-pixel shifts between the individual frames, different centering, interpolation, and flat field normalization methods. For each test run the complete data reduction and analysis has been executed both for TW Hya and the PSF comparison star.

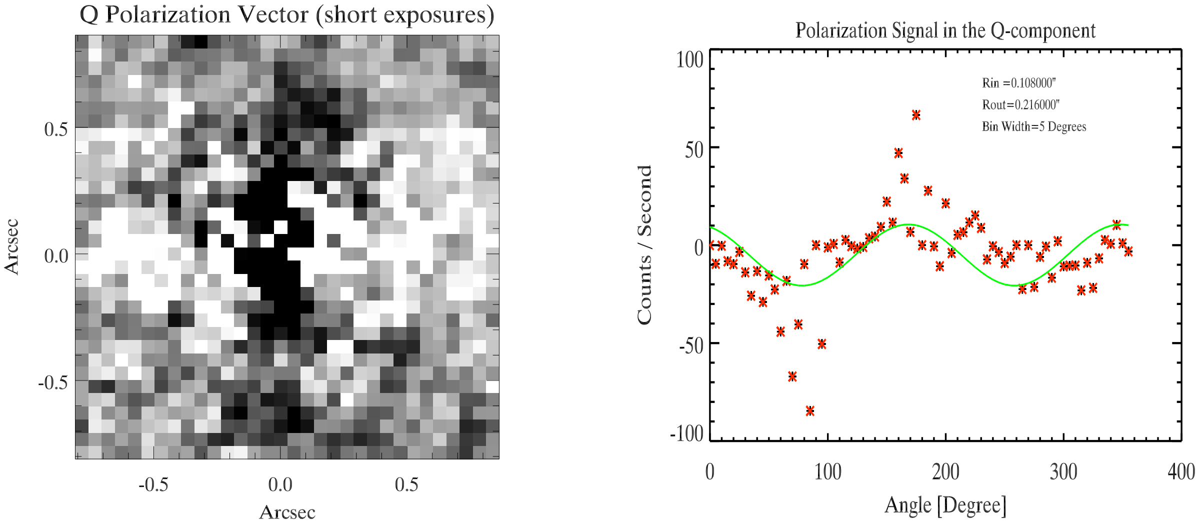

Figure 2.3: *Left panel:* Same as left panel of Fig. 1 but for the the Q_{Short} image. The polarization pattern can be identified between 0.1″ and 0.4″ on the short exposure image. *Right panel:* Same as Fig. 2.2 for an annulus between 0.1″ and 0.2″ from the short exposure series. The sinusoidal modulation (with correct phase and frequency) shows the presence of light-scattering dust as close as 0.1″ to the star. For a comparison of the residuals from the PSF-comparison star plotted in the same scale, see right panel of Fig. 2.4.

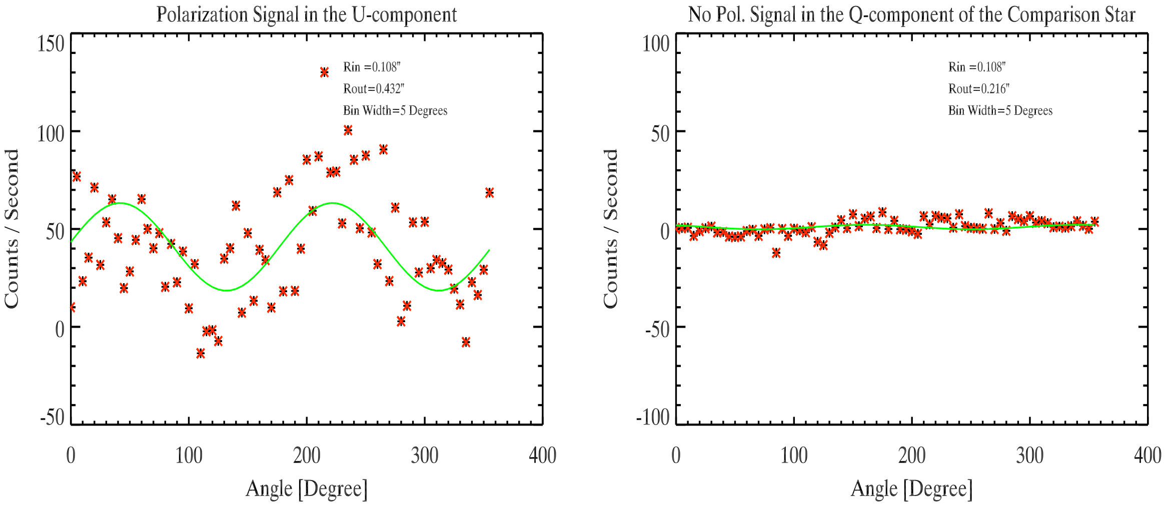

Figure 2.4: *Left panel:* TW Hya Short U image – pol. signal between 0.1″ and 0.4″. *Right panel:* Similar plot for the PSF comparison star GSC 07208-00319. No polarization signal visible (the plot range and analysis parameters are set to be the same as for the right panel in Fig. 2.3).

As the possible sub-pixel misalignments might produce a bipolar, positive-negative pattern mimicking the butterfly pattern of the extended polarization signal, special care was taken to investigate their effects on our results. In order to simulate centering problems, we have introduced normally distributed random shifts with FWHMs of 0.2, 0.5, 1.0 and 1.5 pixels *after* the centering step. The sinusoidal modulation of the TW Hya short exposure frames gets strongly distorted and asymmetric even for the sub-pixel misalignments (0.2 and 0.5) and the pattern is completely disrupted for misalignments as large as 1 or 1.5 pixels. The short exposure images of the PSF comparison star start to show a sinusoidal modulation, but its frequency is *one half* of that of the polarization signal. These images show, in fact, offset negative and positive peaks which can easily be discriminated from the butterfly pattern shown in Fig. 2.2. The long exposure images are less sensitive to sub-pixel misalignment but are noticeably distorted in the case of large (1 or 1.5 pixel) centering errors.

In order to explore the influence of systematic errors in the centering procedure we have introduced fixed shifts of 0.1 and 0.2 pixels after our centering procedure. We found that systematic centering errors as small as 0.1 pixels lead to a strong positive-negative pattern and the disruption of the polarization signal. These systematic errors produced similar pattern for the PSF comparison star as reported for the case of random shifts and can, therefore, not resemble the correct polarization pattern.

Additional tests included the comparison of centering methods based on cross-correlation and on Gauss fitting, bilinear and cubic interpolations at the rotation of the images, as

well as the local and global normalization of the flat field images. We found that the Gauss-fitting centering, the bilinear interpolation and the individual normalization of each stripe in the Wollaston-masked flat field leads to the highest signal-to-noise ratios.
These test runs proved that the strongest noise sources in the reduction procedure are the sub-pixel misalignments and the flat field errors. We found no combination of the artificially introduced errors that could create a false (phase- and frequency-correct) sinusoidal modulation and thus could lead to the misinterpretation of our data set.
Chromatic effects from the Wollaston prism could also lead to slight differences between the o- and e-beams and thus to an imperfect subtraction. However, the $\mathrm{MgF_2}$ prism used in the CONICA camera introduces a relative displacement of only 86 mas between the blue and red edge of the broad K-band (CONICA Manual). In the narrower Ks-band this effect is even smaller and is therefore not expected to influence the PDI observations.
As TW Hya and the PSF star were observed in very similar airmass ranges (1.02 – 1.08 and 1.09 – 1.22) and seeing conditions ($0.6''$), we expect that any atmospheric effect leading to a false polarization signal would effect the PSF comparison images in the same way. Since there is no evidence for such an atmospheric influence in the comparison images (see right panel of Fig. 2.4), we exclude atmospheric chromatism as a possibility to mimic PDI signals.
The examination of the data reduction, possible instrumental and atmospheric effects led us to conclude that the extended polarization signal in our images indeed originate from the light scattering on the circumstellar dust around TW Hya.

2.5 Results

imaging observations, we obtained Ks-band images of the circumstellar disk around the classical T Tauri star TW Hya, which probe the disk structure closer to the star than any previous observation. Our diffraction limited PDI of TW Hya shows an extended butterfly pattern (see Figs. 2.2, 2.3) characteristic for a spatially resolved axisymmetric light scattering source. This pattern is present between $0.5''$ and $1.4''$ on the long exposure Q- and U-images and between $0.1''$ and $0.4''$ in the short exposure images. The observations of the regions closer than $0.1''$ to the star and between $0.4''$ and $0.5''$ do not have sufficient SNR for a reliable analysis. The SNR of the data set is sufficiently high to plot the azimuthally integrated Ks-band surface brightness density distribution between $0.5''$ and $1.4''$ (see Fig. 2.5).

2.6 Discussion

2.6.1 Scattering

The presence of the extended polarization signal across our FOV confirms the existence of light scattering material. The sinusoidal modulation of the Q- and U-images confirms the centrosymmetric polarization pattern. The fact that we detected such emission even as

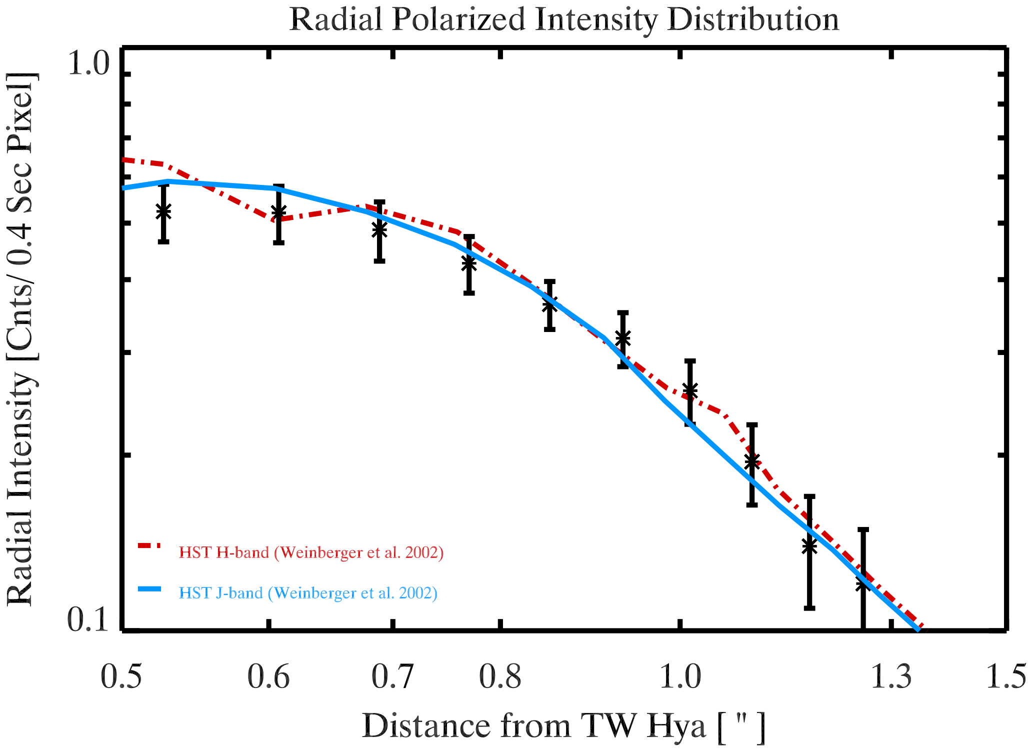

Figure 2.5: Relative radial polarized intensity distribution of the TW Hya disk between 0.5″ and 1.4″. The asterisks mark our 3-pixel-binned Ks-band PDI data, while the solid and dashed curves show the J- and H-band surface brightness distributions from Weinberger et al. (2002). Although the surface brightness is not equivalent to the PI, applying an arbitrary offset shows the similar behaviour of the three curves. The slope change around 0.8″ has been found already by Krist et al. (2000) and Weinberger et al. (2002). The error bars represent the combined errors from the PSF-comparison residuals and the statistical errors of each annulus.

close as $\sim$0.1″ ($\sim$6 AU) to TW Hya is the first direct evidence that its dust disk extends so far in. This detection does not support the model of Krist et al. (2000) who proposed the presence of an inner 'dark' zone ($r \simeq 18$ AU $= 0.3''$) with suppressed flaring angle, necessary to explain the exceptional brightness of the TW Hya disk.

Based on the modeling of the SED, Calvet et al. (2002) predicted the presence of a mostly dust-evacuated inner gap at $r < 3 - 4$ AU ($r < 0.07''$). Such a gap could be a tell-tale signpost of a massive planet in close orbit around TW Hya and would be of high importance. However, our commissioning data do not allow to draw any definite conclusions on the existence of this feature.

2.6.2 Radial Profile and Slope Change

In Fig. 2.5 we show the comparison of the radial polarized intensity derived from our PDI observation and (arbitrarily shifted) radial surface brightness profiles measured by the HST (Weinberger et al. 2002). Although these measurements probe different quantities at different wavelengths (Ks and J, H, respectively) a remarkable similarity is evident between the radial slopes. Based on this similarity, we conclude that the polarization degree is nearly independent of the radius and thus the polarized intensity characterizes the surface brightness. Thus, the PDI method can lead to contrast enhancement without the loss of information.

The radial surface brightness profile between 0.9″ and 1.4″ can be well fitted by a power-law function $I_{\mathrm{Ks},1} \propto r^{-3.1\pm0.3}$. This is slightly steeper than the $I_{\mathrm{J,H}} \propto r^{-2.6\pm0.1}$ behaviour found by Weinberger et al. (2002) at 1.1 and 1.6 μm, for the region between 0.8″ and 2.7″. To place our results in context, we compare them to surface brightness slopes predicted by simple analytical approximations (e.g. Whitney and Hartmann 1992). These approximations consider only isotropic scattering and simple geometric effects and do not include wavelength-dependent terms. The predicted surface brightness power-law exponent for an optically thick, geometrically thin disk is -3, while for a flaring disk an exponent of -2 is expected. Our Ks-band results in the $0.9'' < r < 1.4''$ region support the flat disk geometry or a very small flaring. However, the surface brightness slope is determined by an intricate interplay between many disk and dust parameters and is not a conclusive measure of the disk geometry.

As to underline this statement, a strong, gradual change in the brightness profile around 0.8″ from TW Hya is evident. The annulus between $0.5'' < r < 0.7''$ is characterized by the very gentle surface brightness behaviour of $I_{\mathrm{Ks},2} \sim r^{-0.9\pm0.2}$. The slope of the curve is even less steep than that expected from a flared disk (Whitney and Hartmann 1992).

Although the radial brightness slope is strongly influenced by the disk geometry, slope changes can have different origins. Even though a detailed analysis of the reasons of the slope changes is beyond the scope of the current work, we refer to some of them. The most obvious one is an actual change in the surface density slope of the disk, translating into a slope change in the surface brightness. Such clear-cut changes might be the results of external or internal perturbation of the disk by a companion or a massive planet as seen in the case of HR 4796A (see, e.g. Boccaletti et al. 2003).

A second cause might be the change of the flaring angle and through this the change in the illumination of the disk's surface. Alternatively, a radial dependence of the scattering cross section of the dust grains might introduce modulations in the surface brightness profile. Disentangling the effects of these processes requires high-angular resolution observations at longer wavelengths.

We note, that this change in the slope at 0.8″ has been detected previously at shorter wavelengths by HST direct imaging and coronographic studies (Krist et al. 2000; Weinberger et al. 2002), together with other slope changes in the outer parts (>1.4″) of the disk.

Our data were acquired during the commissioning of the NACO instrument and suffer from high detector noise and limited AO performance. The current performance of NACO is expected to result in roughly five times better SNR. The first results of a PDI survey of the TW Hya Association are presented by Huélamo and Brandner (2004).

For future PDI observers it might be important to point out some of the limiting factors in our data set. First, the dynamic range of the data set has to be increased by applying series of different exposure times. Furthermore, the flat field calibration plays a critical role and should be carried out with great care. Finally, the necessarily saturated star will pose limitations to the accurate alignment of the individual frames, which will in practice determine the inner radius until which the polarization signal can be detected.

2.7 Summary

We presented the first high-contrast observations carried out with NACO/VLT using the PDI technique. The extended scattering pattern of TW Hya provides the first direct proof that the disk extends closer than 0.5″, up to ∼ 0.1″ (∼ 6 AU) from the star.

We derive the first Ks-band radial polarized intensity profile between 0.5″ and 1.4″. This profile strongly resembles the surface brightness profile seen at shorter wavelengths and shows as well a strong, gradual slope change around 0.8″. The polarized intensity profile between 0.9″ and 1.4″ stands close to that expected from a flat disk.

These results demonstrate the potential of the PDI technique at the NACO/VLT platform for future planet formation studies. This technique is capable of imaging a new, beforehand unaccessible regime of circumstellar disks at very high resolution. Such images can help understanding the evolution of protoplanetary disks at the scales comparable to our inner Solar System.

The findings of this chapter have also been published in a shortened form in the journal Astronomy & Astrophysics (Apai et al. 2004b). The colour version of Fig. 2.2 has appeared on the cover page of the 20th February 2004 issue.

Although TW Hya is a member of a loose co-moving association of young stars (Kastner et al. 1997) it can be well described as a single, isolated object. TW Hya and its regular, unperturbed disk is believed to be a good example of young Solar-type stars and their environment, fitting nicely to the current star formation picture outlined in Chapter 1. However, is this picture representative for the intermediate and high-mass stellar environments? In the next chapter we will apply the ALFA and NACO adaptive optics systems with contrast-enhancing methods to study the environment of these more massive stars.

Chapter 3

Environment of Young Low- and Intermediate-Mass Stars

The circumstellar disk observed around TW Hya represents the disk accretion phase and planet formation stage of young, single stars. However, large fraction of the main-sequence stars are binary or multiple systems. Additionally, it has been shown that stars with increasing masses are found more often surrounded by small clusters of low-mass stars (see, e.g. Testi et al. 1999). In order to further explore how the environment of young, intermediate-mass stars differ from the case of the isolated low-mass star TW Hya, we applied the ALFA and NACO adaptive optics systems to study some of the nearest targets. While the amount of available observing time on the ESO Very Large Telescope allowed the investigation of one target, our three long observing runs in the Calar Alto Observatory allowed us to carry out a survey of nearby young stars.

3.1 ALFA Survey of Young Nearby Stars

3.1.1 Observations

During our three adaptive optics assisted imaging campaigns in January 2002, October 2002 and June 2003 we targeted young, nearby stars with known infrared excess emission, mostly focusing on the intermediate-mass Herbig Ae/Be stars. Table 3.1 summarizes the targets, the coordinates, the dates of the observations and the exposure times in the different filters. The observations were carried out using the ALFA adaptive optics system (Hippler et al. 1998) and the near-infrared camera Omega Cass mounted at the 3.6 m telescope at the Calar Alto Observatory, Spain. The plate scale used in our observations was 0″.038 pixel^{-1}. The typical weather conditions changed between good and excellent, with optical seeing between 0″.7 and 1″.3. The observations aimed to enhance the contrast of the imaging system by the subtraction of a reference PSF from the target object. In order to compensate for the temporal variations of the PSF due to the changes in the atmosphere and in the optical system, we applied short observing *cycles*, alternating between the target and the PSF

Table 3.1: Log of the ALFA observations of young stars. The columns list the object names, coordinates, date of the observations and the exposure times in the J, H and Ks near-infrared filters.

Object Name	R. A. (J2000)	Dec. (J2000)	Date	Exposure Time [minutes] J-Band	H-Band	Ks-Band
SU Aur	$4^h\ 55^m\ 59^s$	$+30^\circ\ 34'\ 01''$	27/01/02	23	17	23
AB Aur	$4^h\ 55^m\ 49^s$	$+30^\circ\ 33'\ 04''$	26/01/02	23	23	23
V 372 Ori	$5^h\ 34^m\ 47^s$	$-05^\circ\ 34'\ 14''$	28/01/02	6	23	23
HD 31305	$4^h\ 55^m\ 48^s$	$+30^\circ\ 20'\ 16''$	26/01/02	14	6	6
HD 282737	$4^h\ 58^m\ 19^s$	$+30^\circ\ 16'\ 59''$	27/01/02	17	6	12
FU Ori	$5^h\ 45^m\ 23^s$	$+09^\circ\ 04'\ 12''$	27/10/02	11	–	5
HD 38224	$5^h\ 44^m\ 31^s$	$+08^\circ\ 38'\ 14''$	27/10/02	5	–	3
V 380 Cep	$21^h\ 01^m\ 37^s$	$+68^\circ\ 09'\ 48''$	26/10/02	11	–	–
HD 207031	$21^h\ 07^m\ 41^s$	$+68^\circ\ 15'\ 15''$	26/10/02	5	–	–
XY Per	$3^h\ 49^m\ 36^s$	$+38^\circ\ 58'\ 56''$	26/10/02	12	10	10

reference star.

Each *cycle* consisted of four dithering positions around the target with roughly 50 seconds spent at each position. We adjusted the individual detector exposure times to the brightness of the given target and set the repetition rate accordingly. Before moving to the PSF reference object we typically completed at least two full cycles on the science target.

The typical observational scheme was as follows: two cycles on the science target, two cycles on the PSF-reference object and two further cycles on the science target. The total on-source integration time for the science targets was typically about 10 minutes in each filter. These cycles were observed immediately one after the other to minimize the PSF variations. Depending on the actual circumstances we slightly adjusted our observing scheme to the individual objects. We summarize the total exposure times for the observed targets in Table 3.1.

3.1.2 Data Reduction

The basic data reduction was conducted in the standard fashion with bad pixel removal and flat field correction. The sky frame for each cycle was obtained by taking the minimum of the images at different dithering positions of a given *cycle*. This sky frame was subtracted from each individual image of a given cycle. Following this, the frames from a single cycle were combined into a mosaic image. The relative shifts of the individual frames were determined by cross-correlating the images.

In order to enhance the contrast between possible companions or circumstellar material and the bright target stars, we subtracted a brightness-scaled and positionally aligned PSF,

Table 3.2: Summary of the positive results from the ALFA imaging campaign. The companion candidate of XY Per has been reported before, our observations provide confirmation and the first accurate photometry.

Object Name	Detection Type[a]	Notes	Comp. Cand. Photometry J [mag]	H [mag]	Ks [mag]	Comments
SU Aur	EE	up to 14″				
AB Aur	EE					
V 372 Ori	CC	Sep.=9.50″	15.7	14.2	13.2	
HD 31305	CC	Sep.=0.42″	10.1	9.0	8.6	PSF for AB Aur
HD 282737	CC	Sep.=0.82″		12.3	12.6	PSF for SU Aur
FU Ori	CC	Sep.=0.55″	10.7		9.6	
HD 38224	CC	Sep.=1.08″				PSF for FU Ori
V 380 Cep	CC	Sep.=5.78″	13.3			
XY Per	C	Sep.=1.30″				

[a] Detection types: CC – Companion Candidate, EE – Extended Emission, C – Known Companion Confirmed.

known from the PSF reference star (see, also Pantin et al. 2000).

3.2 Overview of the ALFA Results

The PSF-subtraction technique significantly enhances the contrast of our observations, resulting in the detection of five new companion candidates, the confirmation of two known companion candidates and the near-infrared (NIR) imaging of the nebulosity around SU Aur and AB Aur. In Table 3.2 we summarize our detections by listing the target names, their coordinates, the types of detections and any further comments. The following sections give a more detailed description of the possible nature of five companion candidates, on the companion candidate of FU Ori and the extended emission around SU Aur and AB Aur.

3.3 Five New Companion Candidates to Young Stars

Our adaptive optics-aided near-infrared observation and the PSF-subtraction technique led to the discovery of six companion candidates in the direct vicinity of the targeted young stars. We summarize the separations from the primary stars and our broad band NIR photometry on these companion candidates in Table 3.2.

In general, two-colour (three-band) photometry is not sufficient to simultaneously constrain the luminosity class and the distance of a given star: a nearby late-type main sequence star can often show identical colours and apparent magnitudes to a distant red giant star (for details see also Sect. 3.4). Although our imaging data can not unambiguously determine the companion nature of these candidates, it is worthwhile to summarize here our observations of the companion candidates and the published observations on the young primary components.

As the companion candidate close to FU Ori has a special astrophysical significance, we will discuss this case in depth in Section 3.4. In the current Section we focus on the other five companion candidates around V 372 Ori, HD 31305, HD 282737, HD 38224 and V 380 Cep.

3.3.1 Companion Candidate to the Youngest Vega-type star

The star V 372 Ori is widely known to show significant far-infrared excess emission, indicative of the presence of substantial circumstellar dust. Long-term optical photometry, however, proves that the star is not varying its flux by more than ~ 0.1 magnitudes (Bibo and The 1991). The unvarying brightness, together with the absence of nebulosity and the lack of emission lines (Blondel et al. 1993) excludes this star from the group of classical Herbig Ae stars. Manoj et al. (2002) proves that V 372 Ori is a member of the Orion Nebula Cluster and thus is not older than $\sim$1 Myr. They argue that the lack of NIR excess emission together with the FIR excess suggest that this star is one of the youngest examples of the Vega-type stars.

A substantial effort was put in identifying any companions of V 372 Ori: the early spectroscopic studies of Levato and Abt (1976) showed that this star is a double-lined spectroscopic binary with components of B9.5V and A0.5 spectral types. The NIR speckle observations of Preibisch et al. (1999) found, however, no close companion with a detection limit of 10.73 K-mag at $0.3''$ from V 372 Ori.

Our ALFA observations display a faint companion candidate with a relatively wide $9.5''$ separation and at a position angle of PA=199.7°. The NIR photometry of the possible candidate is shown in Tab. 3.2. In order to constrain the nature of the candidate, we compared its NIR colours and brightness to those of main sequence and giant stars (Wegner 1994; Bessell and Brett 1988). We found that the NIR photometry is consistent with a highly reddened (A_k=1.7–1.8 mag) O6V–A2V spectral type star at $1 - 16$ kpc distance or an M5V–M6V spectral type star at about 150 pc.

The colours also suggest strong NIR excess emission (see Fig. 3.1), thus arguing for a young star with circumstellar material, which in turn makes the possibility of a nearby, late-type star even more probable.

3.3.2 Companion Candidates to Three Reference Stars

The PSF-subtraction technique requires observing PSF-stars as similar as possible to the science targets in terms of spectral type, apparent brightness and celestial position. During the data reduction process three of our PSF-reference stars proved to have faint, previously

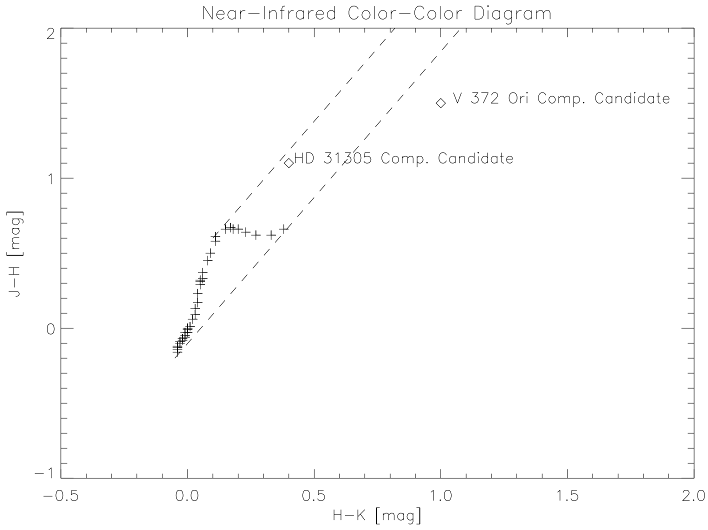

Figure 3.1: The companion candidates to V 372 Ori and HD 31305 in the near-infrared colour-colour diagram. The (J-H) and (H-K) colours of main sequence stars (Wegner 1994; Bessell and Brett 1988) are marked with + signs. The effect of interstellar reddening shifts these colours parallel to the dashed lines (Bessell and Brett 1988). The position of the companion candidate to HD 31305 can be well explained by the colours of a reddened main sequence star, while the position of the V 372 Ori companion candidate has infrared excess emission, typical to young stars (Lada and Adams 1992).

unknown companion candidates. Because our PSF-reference selection criteria favors stars at *physical* locations similar to the young stars serving as science targets, some of our PSF-reference A-stars might likely be yet unknown young stars. Although in general little is known about these objects we summarize the most relevant information here.

HD 31305 was the PSF-reference star for the observations of AB Aur. The data reduction and PSF-subtraction, however, revealed the existence of a very close companion candidate. The star HD 31305 is a less-studied A0-type star. HD 31305 is often used as a flux calibrator for relative photometric observations of AB Aur and the IRAS Point Source Catalogue (Joint IRAS Science Working Group 1988) measurements for HD 31305 show significant infrared excess emission, arguing for the existence of circumstellar dust. Given that the celestial position and the proper motion of HD 31305 is very similar to that of AB Aur, and it also shows sign of circumstellar material, we argue that HD 31305 is a very strong candidate for being a young stellar object.

An additional support to our argument is the X-Ray detection of HD 31305 with the ASCA instrument (Skinner and Walter 1998) demonstrating high chromospheric activity, a frequent characteristic of young stars.

Our ALFA observations resolve a faint, red companion candidate at a distance of $0.42''$ from HD 31305 at a position angle of 232.5°. The near-infrared colours suggest no near-infrared excess for the companion (see Fig. 3.1), and are consistent with a reddened star of A7V – F0V spectral type at the ∼160 pc distance of the Taurus-Auriga association. Alternatively, this star can also be an unrelated background giant star.

The star HD 282737 has served as PSF-star for SU Aur and its visual binary nature was previously unknown. Our ALFA observations resolved a blue point source $0.82''$ away from HD 282737. Due to the lack of complementary observation in the literature, the nature of the star HD 282737 is less known. Having a spectral type, brightness and celestial position similar to SU Aur, it is probable that HD 282737 also belongs to the Taurus-Auriga associations and is a young star. However, the IRAS Point Source Catalogue (Joint IRAS Science Working Group 1988) contains no detection for this position, arguing against the existence of substantial circumstellar material.

Since the possible companion is barely detected in the J-band, we could provide reliable photometry only in the H- and Ks-bands. The H−K colour in itself is insufficient to draw any conclusion on the nature of the object. In order to determine the spectral type of the companion candidate and to confirm its companionship further high-resolution spectroscopic observations are planned.

The star HD 38224 has been observed shortly in the J and Ks filters to provide PSF-calibration for FU Ori. The data reduction and subsequent PSF-subtraction, however, proved the visual binary nature of this object (see star 3 in Fig. 3.2). As this star has not been studied previously in detail, additional spectroscopic observations are necessary to classify both HD 38224 and its possible companion.

3.3.3 V 380 Cep and its Companion Candidate

The well-known Herbig Be star V 380 Cep was one of the primary targets of our ALFA campaign. This B2 IVe spectral type star lies at an estimated distance of 430 pc and shows strong infrared excess emission (Hillenbrand et al. 1992). Recent interferometric observations by Millan-Gabet et al. (2001) indicate the presence of a close companion with a separation of ∼10 mas. Previous spectroscopic observations also showed that this star is a spectroscopic binary (Corporon and Lagrange 1999), while visual/near-infrared observations resolved it as a wide binary (Corporon, unpublished). The details of these latter observations are, however, not known.

Our ALFA observations provide an independent discovery of the companion candidate at 5.78″. It is not clear, if Corporon had detected the same object. Due to technical problems during the ALFA observations only J-band observations are available, which is insufficient to constrain the nature of this faint companion candidate. This detection makes V 380 Cep a particularly good target for multi-colour adaptive optics follow-up observations aiming to determine if the faint source is associated to the Herbig Be star and to reveal possible further association members (see the NACO results on HD 104237 in this chapter).

3.4 FU Ori and its Companion Candidate

Our adaptive optics observations described in Section 3.1.1 led to the detection of a faint red star in the apparent vicinity of FU Ori, the prototype of the FUor outburst stars. Due to the special astrophysical importance of FU Ori and to the presence of additional data sets, we discuss in details the possible nature of the newly detected star based on near-infrared photometry and its proper motion relative to FU Ori. The photometric data are consistent with a nearby late-type main sequence star, a background giant star, and a pre-main sequence star. On the basis of the proper motion and the stellar surface density in the direction towards FU Ori, we argue that the probabilities of the first two options are very low.

3.4.1 Astrophysical Importance of FU Ori

Recent studies of low-mass stars in the star-forming regions Taurus (Gullbring et al. 1998) and Orion (Robberto et al. 2003) indicate surprisingly low accretion rates between $\dot{M} \simeq 10^{-7} - 10^{-10}$ $M_\odot$ yr^{-1}. These accretion rates are far too low to build up solar-type stars on timescales of the order of 10^6 yr, as it is expected in the current picture of low-mass star formation (see Chapter 1 or Lada 1999). An elegant alternative to the quiescent, steady accretion can be the occurrence of periodic, short events of intense accretion ($\dot{M} \simeq 10^{-4}$ $M_\odot$ yr^{-1}), during which a significant fraction of the disk mass can be accreted (Hartmann and Kenyon 1996). The well-known FUor objects (Herbig 1966, 1977) may represent this intense accretion phase of the otherwise quiescent T Tauri stars (Hartmann and Kenyon 1996). Thus, if FUor outbursts are typical to *all* T Tauri stars, these outbursts might be the dominant way of mass accretion.

Models based on the enhanced accretion rates are in general successful in explaining the observed properties of the FUor outbursts (Hartmann and Kenyon 1985; Kenyon et al. 1988), but the causes of the onset of the rapid accretion are still disputed. Suggested possibilities include thermal instabilities in the disk (see, e.g., Lin and Papaloizou 1985; Kawazoe and Mineshige 1993; Bell and Lin 1994) and perturbations from close companions (Bonnell and Bastien 1992; Clarke and Syer 1996), but up to now none of these explanations could be confirmed observationally.

However, earlier high-angular resolution observations led to the detection of companions for the FUor objects L1551 IRS 5 (Rodriguez et al. 1998) and Z CMa (Koresko et al. 1991), with a separation of 45 and 93 AU respectively. Moreover, Kenyon et al. (1993) found RNO 1B and 1C to be a FUor binary. Infrared long-baseline interferometry shows that FU Ori might have a close companion with a separation as small as 0.35 ± 0.05 AU, although these observations could be explained more naturally with the presence of a circumstellar disk (Malbet et al. 1998).

In order to avoid confusion we use the name FU Ori for the prototype star ($\alpha = 05^h45^m22''.6$, $\delta = +09^\circ04'12''$), while the term FUor stands for the class of stars named after FU Ori.

3.4.2 Detection of a Companion Candidate

Our data reduction procedure yielded the PSF-subtracted J and Ks band images of the star FU Ori (see Fig. 3.2). The central part ($r < 0''.4$) is heavily contaminated by the PSF-subtraction residuals and speckle phenomena. The residuals originate from the imperfect PSF subtraction due to the temporal variations of the PSF. The speckle pattern differences lead to the *speckle boiling* (Racine et al. 1999), resulting in a dotted noisy pattern. South-east from the FU Ori residuals an over-subtracted (negative) star is visible. This faint star is a previously unknown (visual) companion of the PSF-reference star HD 38224 (see also Sect. 3.3.2). This (visual) companion star is also identifiable on the reduced (non-PSF-subtracted) images of HD 38224, but it becomes very evident after the subtraction. We note that in the Ks band the first Airy-ring of this star is well visible.

The major result of our observations is the detection of a previously unknown star in the FU Ori images to the south of FU Ori (see Fig. 3.2). In the following we will refer to this star as FU Ori S. The following facts exclude the possibility of FU Ori S being an artifact:

1. The star has been detected in both the J and Ks bands at the same location (see panels A and B in Fig. 3.2): The position difference is less than $0''.01$ and the position angle difference is only 2.8° – within the errors of the position determination ($0''.03$; 3°).
2. The star shows an Airy-ring pattern in the Ks band image, like the (visual) companion of the PSF reference star.
3. The star is also detected at the same position, when another PSF star (HD 201731 in the J-band, XY Cep in the Ks band) from the same night is used as PSF reference. Although these PSF-stars were observed several hours before FU Ori, subtracting them from FU Ori reveals again the existence of FU Ori S.
4. Archival data from the adaptive optics (AO) system PUEO mounted on the Canada-France-Hawaii Telescope (shown in Fig. 3.3) provides independent confirmation for the

existence of FU Ori S. The co-added image was obtained through the K continuum filter ($\lambda_c = 2.260\ \mu$m, $\Delta\lambda = 0.060\ \mu$m) with a total exposure time of 11.2 seconds.

With respect to FU Ori, we derive from our ALFA images a position angle of $160.8° \pm 3°$ and a separation of $0\overset{''}{.}50 \pm 0\overset{''}{.}03$ (projected linear separation = 225 ± 14 AU) for FU Ori S. The positional error given here is dominated by the centering uncertainties of FU Ori S (around 0.5 pixels).

Accurate photometry of FU Ori S suffers from the PSF-subtraction residuals and the speckle noise. In order to reduce these effects, we used a photometric aperture as small as $0\overset{''}{.}19$ ($\simeq 1.6 \times$ FWHM). Our photometric conversion factors were deduced by applying this aperture to the stars FU Ori, HD 38224, and HD 201731 and using their 2MASS Point Source Catalogue fluxes. The error on the conversion factor in the J band is estimated to be 0.22 mag. In Ks band, due to the saturation of FU Ori and HD 201731 we can only derive the conversion factor for HD 38224. As the AO system performs better in the Ks band than in the J band, the conversion factor error in the Ks band should be smaller than that in the J band. To be conservative we adopt the error of the conversion factor in the Ks band to be the same as that in the J band. Another major uncertainty of the aperture photometry of FU Ori S comes from the speckle pattern. To estimate its influence on our photometry, we have integrated the flux of speckle noise in 18 positions over an aperture with the same diameter as used for FU Ori S. Comparing these fluxes to that of FU Ori S, we estimate an error due to speckle noise of 0.11 mag and 0.08 mag in J and Ks bands, respectively.

Based on the aperture photometry and the described error estimates, we derive an apparent brightness of J= 10.65 ± 0.25 mag and Ks= 9.64 ± 0.23 mag for FU Ori S. The apparent brightness of FU Ori is J = 6.519 ± 0.023 mag, K = 5.159 ± 0.020 mag (Cutri et al. 2003). Therefore, the brightness contrast between FU Ori and FU Ori S amounts to 4.13 and 4.48 mag in the J and Ks bands, respectively.

3.4.3 Discussion

The result of our AO observations is the identification of a faint star close to FU Ori, the prototype of the FUor stars. In the following we assume 450 pc as the distance of FU Ori. Our photometry shows the unusually red colour of FU Ori S (J - Ks = 1.01 ± 0.34) which is similar to that of FU Ori itself (J - K = 1.36 ± 0.03). Although unambiguously determining the nature of FU Ori S from only two near-infrared fluxes is not possible, valuable conclusions can be drawn from its photometric properties. In this section, we first discuss the probability of FU Ori S being an unrelated field star, then the possibility of FU Ori S being a late-type main sequence (MS) star, a giant/supergiant or a pre-MS star with Ks-band infrared excess.

The very vicinity of FU Ori S to FU Ori suggests that FU Ori S is most probably a companion of FU Ori: The 2MASS Point Source Catalogue (Cutri et al. 2003) shows that the FU Ori region is not densely populated: in a region with a radius of $8'$ centered on FU Ori there are only 6 stars brighter than FU Ori S (Ks = 9.64 mag) in the K band. In analogy to earlier binarity surveys, we would consider any bright star closer than $\sim 2\overset{''}{.}5$ to

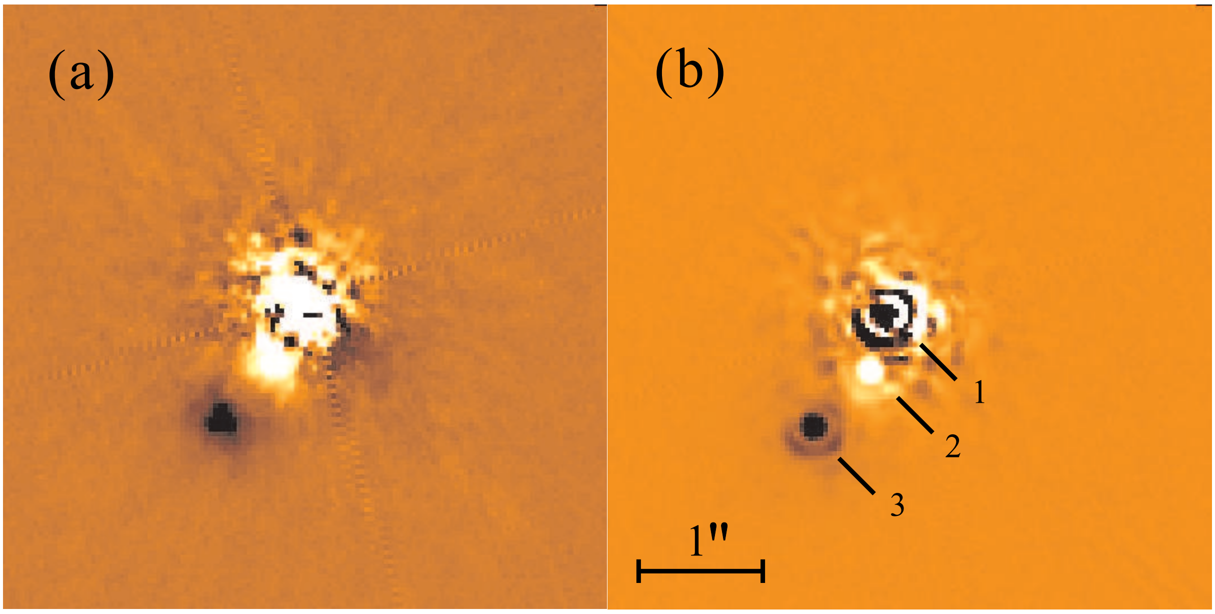

Figure 3.2: PSF-subtracted images of FU Ori, (a) in J and (b) in Ks band. North is up and east is to the left. The positions of FU Ori, FU Ori S, and the visual companion of the PSF reference star are indicated with numbers 1-3 in (b). The image scale is marked in (b).

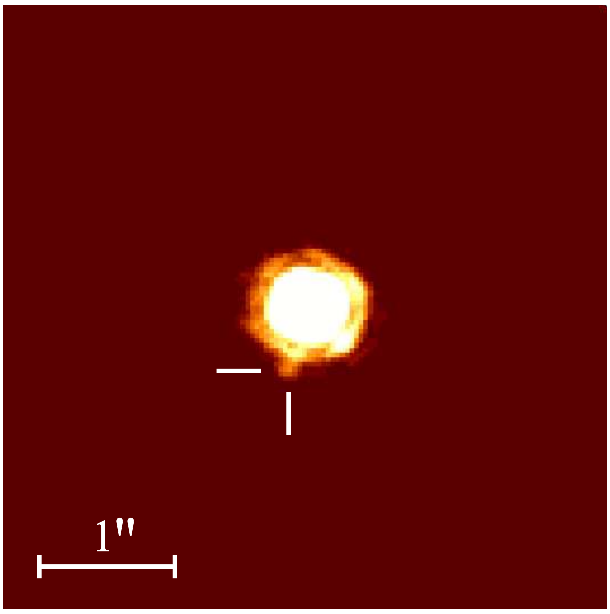

Figure 3.3: CFHT PUEO image of FU Ori through the K continuum filter. The observations were made on 1997 December 22. The total exposure time is 11.2 s and no PSF-subtraction was applied. The position of FU Ori S is indicated.

FU Ori as a companion. Therefore, the probability for a bright field star to be considered as a companion by chance is less than $\frac{6}{(8\times 60)^2\pi} \times 2.5^2\pi = 1.6 \times 10^{-4}$. This estimate strongly supports the view that FU Ori S is a companion of FU Ori.

The photometry and the proper motion data give further constraints on the nature of FU Ori S. If it is a main sequence (MS) star, its spectral type – assuming no extinction – will be later than K4 to match its red colour. A simple comparison of the absolute brightness of MS stars to the apparent brightness of FU Ori S sets the upper distance limits of 120 pc for K4 and 50 pc for M6 spectral types. Such a nearby star, however, is likely to display a measurable proper motion over the 5 years time base between the ALFA and PUEO observations. For example, from the Hipparcos catalogue (Perryman et al. 1997) the average annual proper motion of stars located at distances between 50-120 pc and within a radius of 10° around FU Ori is 38 mas yr^{-1}. In contrast, the absolute proper motion of FU Ori itself is less than 6 mas yr^{-1} (see Tycho catalogue Hoeg et al. 1997). Thus, if FU Ori and FU Ori S are unrelated, their relative separation should have changed by an amount of $0\farcs19$ over 5 years, a clearly detectable shift in the AO images. Comparing the PUEO position to that derived from ALFA we found a position difference of only 10 ± 48 mas (the centering error of the PUEO images is estimated to be 1 pixel). This gives a proper motion limit of 2 ± 10 mas yr^{-1} and indicates that FU Ori S is unlikely to be a nearby MS star.

Such a very small relative proper motion can be consistent with a star co-moving with FU Ori or a distant background object. Considering the option that FU Ori S is a background giant – assuming the case of no extinction for simplicity – we obtain that giants with spectral types between K1 and M7 at distances between 2 to 34 kpc are consistent with the photometry. Additional reddening would decrease the distances but would not change the overall picture.

The third and most exciting possibility is that FU Ori S is a pre-MS star associated to FU Ori itself. A simple comparison to the isochrones of Baraffe et al. (1998) shows that the observed fluxes are in an overall good agreement with the predicted magnitudes of a $\sim 1.1\ \mathrm{M}_\odot$ star of the age of 10^6 yr at the 450 pc distance of FU Ori ($\mathrm{J}_{\mathrm{BCAH}}$=10.61 mag and $\mathrm{K}_{\mathrm{BCAH}} = 9.80$, for [M/H] = 0, Y = 0.275, and $\mathrm{L}_{mix} = \mathrm{H}_p$). Apparently FU Ori S is somewhat redder than these pre-MS isochrones. This could be due to a reddening of $\mathrm{A}_v = 1.1$ mag and/or the infrared excess arising from warm circumstellar material. We point out, that assuming FU Ori S as a pre-MS star provides a natural explanation for the observed brightness, colour and the lack of proper motion relative to FU Ori. Assuming a physical association between FU Ori S and FU Ori, taking the mass of FU Ori S to be 1.1 $\mathrm{M}_\odot$ and the mass of FU Ori to be 0.5 $\mathrm{M}_\odot$, the typical mass of T Tauri stars, the primary in the FU Ori binary system is in fact FU Ori S, rather than FU Ori itself. Moreover, if we assume circular orbits in the plane of sky, the above masses and the linear separation (225 ± 14 AU) yield an orbital period of $\sim$ 2700 yr.

In the case of FU Ori S being physically associated with FU Ori, the properties of the FU Ori binary matches well with those used in the model of Bonnell and Bastien (1992). For example, in their 1G and 1O simulations the mass ratios are 0.67 and 0.42, respectively, and the intervals between the companion periastron passes are around 2500 and 2100 yr (see

Bonnell and Bastien 1992, Figs 2 and 3). In contrast, the mass ratio and the companion separation of the FU Ori binary candidate differs strongly from those used in the Clarke and Syer (1996) model in which a companion of mass of 10^{-2} $M_{\odot}$ at a very close distance ($\sim$ 0.1 AU) to the primary is exploited to trigger the enhanced accretion. We note, that the detection of more and more companions of FUor stars points to the possibility that they may play an active role in triggering the outbursts.

The results on FU Ori in this section has also been presented in international conferences (Apai et al. 2003) and published in the Astrophysical Journal (Wang et al. 2004). Recent, yet unpublished adaptive optics-assisted spectroscopic follow-up observations with the Subaru telescope confirmed the pre-main sequence nature of FU Ori S and thus prove that the two stars are associated (B. Reipurth, priv. comm. 2004).

3.5 Circumstellar Envelopes around AB Aur and SU Aur

The study of circumstellar material and disk accretion was one of the two major goals of our adaptive optics campaign. Beside the discovery of several new companion candidates, we also acquired high-contrast, high-resolution NIR imagery of the young Herbig Ae star AB Aur and in its vicinity the T Tauri star SU Aur (see Fig. 3.4). These observations were carried out under very good weather and instrumental conditions (uncorrected infrared seeing $\sim$ 0.8”, good transparency, 0.14” adaptive optics-corrected seeing and Strehl-ratio of $\sim$ 41% in K-band), in the fashion described in Sect. 3.1.1. These deep images show significant extended excess emission after the the subtraction of the instrumental PSF (see Sect. 3.1.2), which we identify as light scattered from the circumstellar envelope around these two young stars. In the following we briefly overview the rich literature of AB Aur and SU Aur and discuss our results.

3.5.1 The Herbig Ae star AB Aur

The young star AB Aur is one of the closest Herbig Ae star at a distance of 144^{+23}_{-17} pc (van den Ancker et al. 1998). Its age is estimated to be between 2 and 4 ±1 Myr (van den Ancker et al. 1998; Natta et al. 1997) and has a spectral type of A0. AB Aur and the nearby SU Aur are physically related and form a common proper motion pair (Zinnecker and Preibisch 1994). Mannings and Sargent (1997) identified a 450 AU gas and dust disk around AB Aur viewed at i=76°. Multi-epoch spectroscopic observations (Grady et al. 1999a) showed transient infalls and accretion of gas. The Hubble Space Telescope STIS coronographic observations of Grady et al. (1999b) revealed richly structured circumstellar material around AB Aur (see Fig. 3.6).

AB Aur was one of the primary targets of our first ALFA observing run and received the longest integration times among all of our targets. The data reduction described in Sect. 3.1.2 provided the PSF-subtracted J, H and Ks-band images. In Fig. 3.5 we show the J-band residual on which circumstellar scattered light is the most pronounced. Although

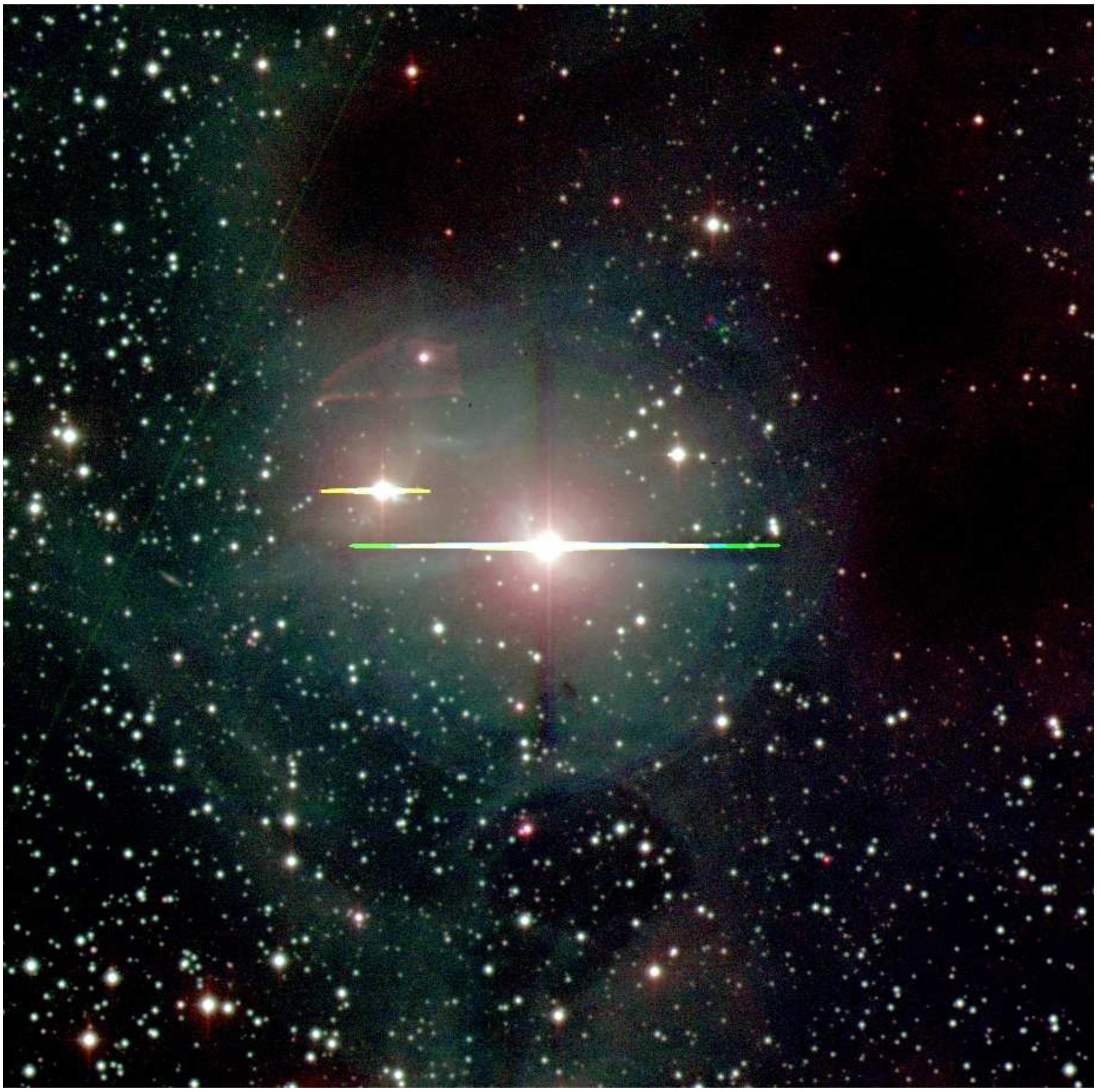

Figure 3.4: Wide field optical view of AB Aur, SU Aur and their environment, obtained by the 2 m Tautenburg telescope. The bright star at the center is the Herbig Ae star AB Aur, while the second brightest is SU Aur, a well-known T Tauri star. The apparent lack of background stars north and west from AB Aur is caused by the light extinction of the dense dust cloud associated to these young stars. The projected distance of AB Aur and SU Aur is about 3.1′, north is up and east is to the left. Image courtesy B. Stecklum.

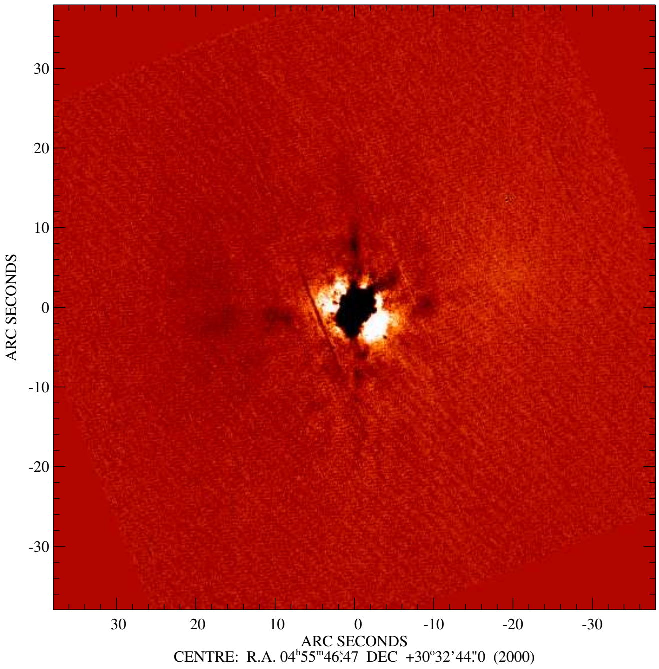

Figure 3.5: J-band PSF-subtracted image of the Herbig Ae star AB Aur obtained by the ALFA adaptive optics system. Extended emission arising from light scattering on the circumstellar envelope is visible around the star, especially to the north-east and south-west directions.

the central regions of the image suffer from the PSF-subtraction noise, extended emission can be traced as far as $\sim 8''$ from the star in the south-west direction. Similar emission is surrounding the star in the north-east direction, too.

The interpretation of the scattered light benefits from the comparison of the ALFA near-infrared images with the optical coronographic data obtained by the Hubble Space Telescope's STIS instrument (see Fig. 3.6). As the STIS coronographic mask is placed directly in the filter wheel, there is no possibility to use an additional, conventional filter in the coronographic mode. The wavelength bandpath is, therefore, set by the sensitivity of the detector to approximately 0.2–1 μm, including both continuum and line emission. For further details on this dataset, see Grady et al. (1999b).

The HST images show an inhomogeneous, possible turbulent emission around AB Aur, which is consistent with the asymmetric circumstellar light seen in the ALFA near-infrared images. The scattered light in the optical HST images extends further out from the star due to the shorter wavelengths and higher instrumental sensitivities.

Figure 3.6: Hubble Space Telescope STIS coronographic image of the circumstellar environment of AB Aur, co-added from two images obtained with different instrument rotations. The irregular polygons are portions of the field that were occulted by the STIS wedge structure or the diffraction spikes in both observations. From Grady et al. (1999b).

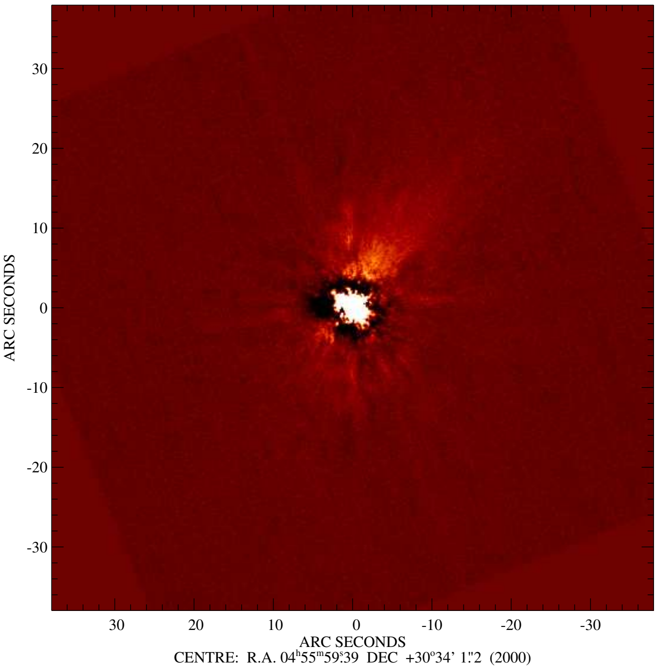

Figure 3.7: J-band PSF-subtracted image of the T Tauri star SU Aur. Extended emission from light scattering on the circumstellar envelope is visible north-west and south-east from the star.

3.5.2 The T Tauri Star SU Aur

The young star SU Aur lies about $3.1'$ from AB Aur. Its distance, derived from its parallax, is 152± 44 pc, very close to that of AB Aur. SU Aur and AB Aur are both members of the Taurus-Auriga star-forming complex and also of the local star-forming region L1517 (Lynds 1962). The extended circumstellar nebulosity around AB Aur suggests a physical link to SU Aur (Grady et al. 1999b).

Similarly to the discussion of AB Aur, we show the J-band residual in Fig. 3.7. The centre of the images ($r < 2''$) is strongly contaminated by the PSF-subtraction residuals. The J, H and Ks images show excess emission close to SU Aur. While in J-band this emission is traceable up to $\sim 15''$ northwest from the star, in Ks-band the emission is detectable only up to $\sim 6''$. This fact shows that the emission is blue, i.e. much stronger at shorter wavelengths.

We use optical, white-light HST/STIS images to complement our NIR observations. In Fig. 3.8 we show the HST/STIS coronographic image of SU Aur (courtesy of C. Grady). This optical image displays a morphology identical to what is seen in our near-infrared images. All images show extended emission to the north-west and a somewhat fainter, less

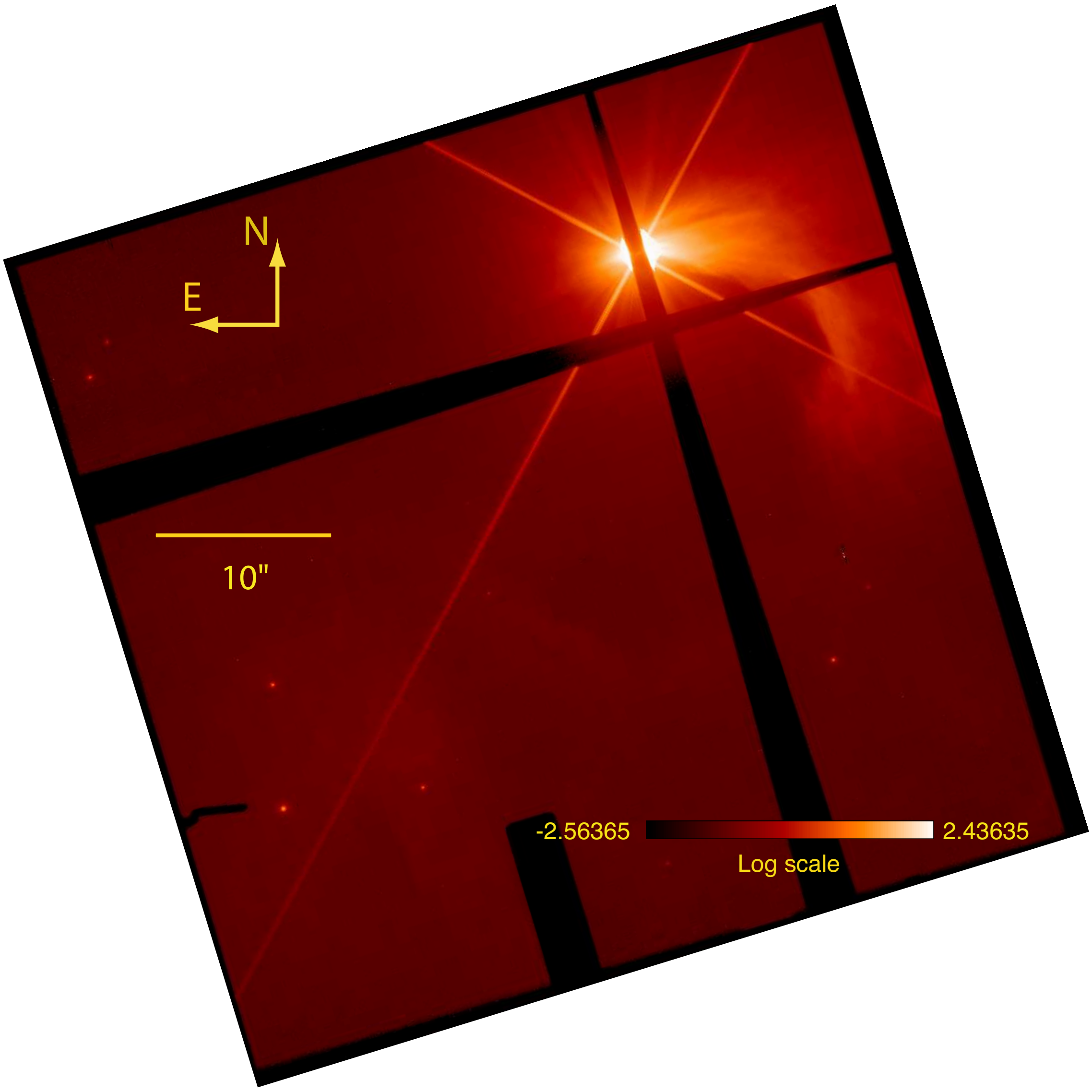

Figure 3.8: HST STIS coronographic image of the circumstellar environment of SU Aur. The orthogonal dark lanes are the coronographic wedges, one of them occulting the bright star. The image is scaled with a radial factor to enhance the contrast of the fainter emission outside the image center. From Grady et al. (1999b).

structured emission lobe in the south-east direction.

The SU Aur images trace the scattered light from ∼3″ from the star westward up to ∼15″. A comparison with the white-light STIS coronographic image reveals the same morphology: a bright lobe of emission is extending westwards up to ∼13″-16″ and then continues further southward. The sharp dark boundary south of SU Aur is presumably the edge of the natal molecular cloud core, from which SU Aur has formed. The morphology of the bright emission lobe strongly resembles the typical shape of molecular outflow cavities often observed in the case of young stars (see, e.g. HH 111 in Reipurth et al. 2000, Mon R2 IRS 3A in Preibisch et al. 2002). In order to prove the existence of an actual outflow, we tried to obtain Fabry-Perot spectral imaging data using the Apache Point 3.5m telescope. Due to unfavourable weather conditions and instrumental problems these observations were not yet successful.

3.5.3 Discussion of the Envelopes around AB Aur and SU Aur

Our ALFA PSF-subtracted adaptive optics images show a new, near-infrared view of the nebulosity around the young stars SU Aur and AB Aur. In both cases we detect extended emission up to at least ∼800 AU from the stars. The extension of the emission is larger than what is expected from the circumstellar disks: In the case of AB Aur the radio observations of Mannings and Sargent (1997) showed that the size of circumstellar disk is ≃450 AU. Based on the linear sizes we argue that the light of AB Aur and SU Aur is scattered back from their circumstellar envelopes rather than their disks.

It it interesting to briefly compare the 2-4 Myr old SU Aur with its older equivalent, the 8 Myr old T Tauri star TW Hya, which we discussed in Chapter 2. While TW Hya is a closely isolated star, SU Aur is still located in a star-forming region, close to young stars, such as AB Aur. The large circumstellar envelope surrounding SU Aur is absent in the case of the older star; similarly, the dark clouds seen in extinction in the vicinity of SU Aur have no counterparts around TW Hya.

3.6 The HD 104237 Association

The young star HD 104237 is the nearest Herbig Ae star. In the frame of a large-scale international campaign to characterize this star, its immediate environment and possible companions or association members, we obtained high-resolution NIR images using the NACO/VLT instrument (see also Chapter 2). Complementary data sets have been obtained by our collaborators using the coronographic mode of the HST/STIS, the International Ultraviolet Explorer (IUE), and the TIMMI2/ESO3.6m mid-infrared instrument. We obtained not only multi-wavelength imaging data but also optical, ultraviolet, and far-ultraviolet spectra. In the following we focus on the NACO/VLT study, its results, and finally we place these results in the global picture deduced from the multi-wavelength campaign.

3.6.1 NACO Observations and Data Reduction

The NACO observations of HD 104237 were carried out on 10th Jun 2003 at ESO's Cerro Paranal Observatory, Chile in the frame of the ESO programme 71.C-0143. During the observations the mean visual seeing at the zenith was $0.6''$ and the object's airmass was about 1.68. Using HD 104237 as the AO wavefront reference star, we obtained diffraction-limited images in the J, H, Ks and L' bands. In the J, H and Ks bands the pixel scale of $0.054''$ was used, allowing a field-of-view (FOV) of $\sim 56''$ for a single exposure. In the L' band the $0.027''$ pix^{-1} camera was applied. Throughout the observations we used the visual dichroic to split the visual light to the visual wavefront sensor.

To remove the sky background a cross-like dithering pattern with $4''$ steps was used. Additionally, two frames, $20''$ east and $20''$ east + $10''$ north from HD 104237 were obtained to enlarge the FOV and improve the sky subtraction. This dithering scheme has been used in the J, H and Ks filters. In the L' band $10''$ north-south chopping throws in combination with $4''$-amplitude random north-south jittering was applied as sky removal technique.

We applied detector integration times (DITs) of 5 s, 2 s, and 2 s in the J, H, and Ks filters with 10 repetitions per dithering position. In order to avoid the saturation of the brighter stars we obtained an additional Ks-band cycle with a DIT of 0.4 s.

For flux calibration in J, H and Ks bands we observed the standard star S677-D = No. 9187 in Persson et al. (1998). In L' band no standard stars were observed with identical instrument configuration to our observations, thus there was no possibility for accurate flux calibration.

The data reduction was carried out by self-developed IDL scripts. After bad pixel filtering, flat field correction and sky removal the individual dithering positions were combined into a mosaic image. The final FOV was approximately $82''\times 63''$.

The resulting images show numerous faint point sources beside the bright star HD 104237. The J-band image and the nomenclature we adopted for the sources in the FOV are shown in Fig. 3.9. In the following we describe the near-infrared photometry and finally the results on the HD 104237 association.

3.6.2 Photometry

We used the DAOPHOT method by Stetson (1987) to obtain an accurate photometry for the stars in our FOV. The formal errors in the flux integration and sky estimation are typically less than 0.02 mag. The saturated star HD 104237 and the two nearby fainter sources (2 and 3) influenced by its halo, however, required special photometric approach. We compared the flux of HD 104237 within an unsaturated annulus (r_{in} $=0.76''$, r_{out} $= 1.08''$) with the fluxes of the unsaturated star 5 within the same annulus. Using this method the relative magnitudes of HD 104237 in the J, H and Ks bands were obtained. In order to derive the absolute fluxes, we compared the flux of star 5 to that of the ESO standard star S677-D-9187 using apertures with radii of $0.76''$, $0.65''$ and $0.65''$ for J, H and Ks-bands, respectively. The fluxes of all other stars in the HD 104237 field were then compared to the flux of star 5.

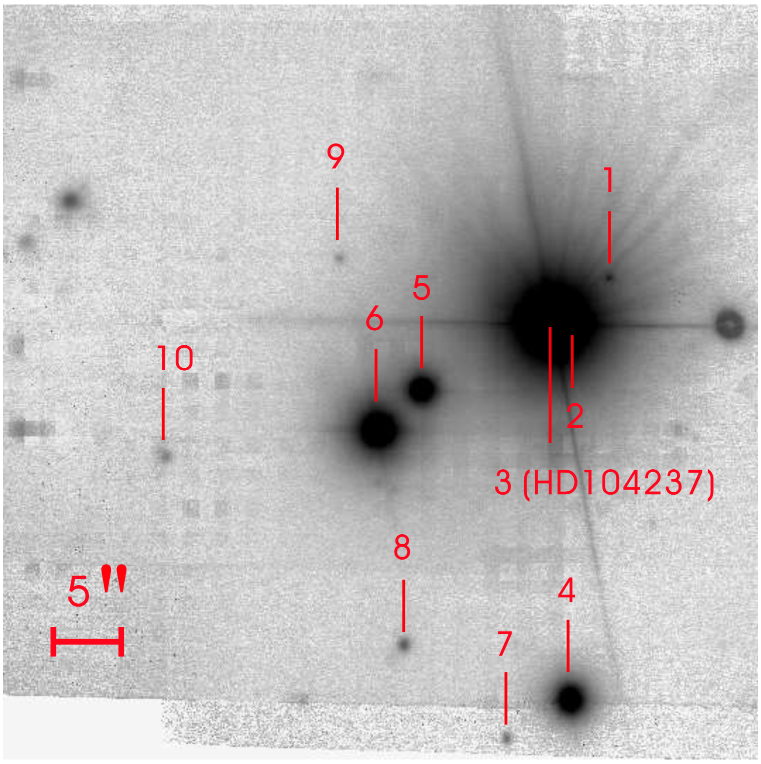

Figure 3.9: NACO J-band image of the Herbig Ae star HD 104237 and an association of nearby young stars. The numbers associated to the point sources show the nomenclature adopted in this section.

Source ID	J	J_{err}	H	H_{err}	Ks	Ks_{err}	Methods[a]
HD 104237	7.30		5.88		6.03		AA
1	15.28	0.03	14.85	0.10	14.48	0.04	SUB
2	11.43	0.08	10.27	0.04	9.52	0.21	SUB
4	10.63	0.02	9.94	0.02	10.00	0.02	PSF
5	10.53	0.02	9.73	0.02	9.67	0.02	PSF
6	9.10	0.02	8.05	0.02	7.70	0.02	PSF
7	16.82	0.02	16.89	0.02			PSF
8	16.03	0.02	15.54	0.02	15.37	0.02	PSF
9	17.07	0.02	16.83	0.02			PSF
10	16.67	0.02	16.11	0.02			PSF

[a] Methods: PSF – DAOPHOT PSF fitting, AA – annulus-aperture photometry, SUB – aperture photometry after PSF subtraction

Table 3.3: Summary of the NACO/VLT broad-band near-infrared photometry of the stars in the vicinity of HD 104237. In addition to the formal photometric errors given here, we estimate a calibration error of 0.08 mag.

The faint star 2 is located only ∼1.3″ west of HD 104237 and was strongly affected by its halo. In order to enhance the contrast of star 2 and measure its brightness, the reduction of HD 104237's contribution was necessary. There was no possibility to obtain an identical or similar PSF from reference star observations. To overcome this problem – assuming mirror symmetry for the PSF – we subtracted the mirrored and aligned eastern half of HD 104237 from the western half. An additional scaling was introduced to minimize the subtraction residuals around star 2. Although the assumption of the mirror symmetry is only an approximation, the subtraction effectively canceled out the strong gradient of the halo of HD 104237. This procedure was repeated for all the images.

Following the subtraction of the halo, in J, H, and Ks bands we integrated the flux of stars 1 and 2 in apertures with a radius of 0.38″. To estimate the aperture correction we compared these fluxes to that derived by placing the same aperture over star 5. The aperture photometry uncertainties due to the subtraction residuals were estimated by integrating the background fluxes in several apertures placed at different position angles than 2 and 3 but to the same distance from HD 104237.

Additionally to the formal photometric errors we estimate a calibration error of 0.08 mags. This estimate is based on the airmass difference between the standard star and star 5, and on an empirical airmass/atmospheric extinction relation for Cerro Paranal. Using that the flux of faint point sources typically dominates a 3 × 3 pixels region in our images, we estimate our 5σ-detection limits in the J, H, and Ks bands to be 22.6, 21.5, and 20.5 mags, respectively.

The summary of the J, H and Ks band photometry from our NACO observations is shown in Tab. 3.6.2.

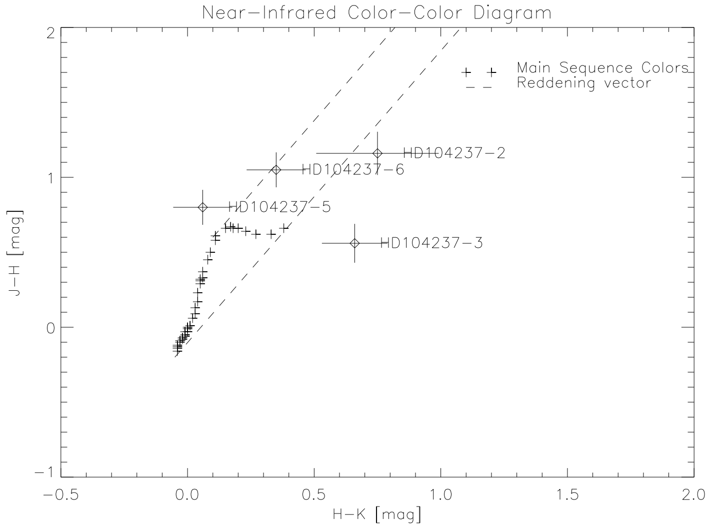

Figure 3.10: Near-infrared colour-colour diagram of the stars around HD 104237. For the figure legend, see Fig. 3.1. The colours of stars 5 and 6 are consistent with being reddened main sequence stars. Stars 2 and 3 display near-infrared excess emission.

3.6.3 Results on the HD 104237 Association

The main result of our NACO observations is the highest resolution and deepest infrared view of environment of the star HD 104237. In these images we identify an association of young stars around the bright Herbig Ae star. Our imaging shows three T Tauri star candidates, the closest being only 1.3″ from the Herbig Ae star. Numerous additional red faint stars are visible in the field of view which might also be associated to HD 104237. In order to determine the nature of these faint sources we show the near-infrared colour-colour diagram in Fig. 3.10. In the interpretation of this diagram we follow Sect. 3.3. The colours of stars 2 and 3 point towards near-infrared excess emission, indicative to young stars, while star 5 and 6 are consistent with a reddened main sequence star. Comparison of the NIR photometry with the theoretical isochrones proves that the age of the aggregate is about 5 Myr. Further evidence for the young age comes also from the complementary data sets.

Mid-infrared observations in our campaign provide additional clues on the existence of circumstellar disks around at least two of the three T Tauri candidate stars. Based on optical HST/STIS spectroscopy we derive the accurate spectral type estimate of A7.5e–A8Ve for HD 104237. The HST/STIS long-slit, low-resolution spectrum reveals a bipolar microjet seen in Lyα driven by HD 104237. Based on the jet geometry we derive an inclination of $i = 18^\circ\ ^{+14}_{-11}$ for the circumstellar disk.

This association of young stars is the second closest after the famous 8 Myr-old TW Hya Association and is, therefore, expected to provide a unique snapshot into the evolution of circumstellar disks and the birth of planetary systems at the 5 Myr-old stage. A more detailed discussion of these results and comparison to other data from our multi-instrument campaign has been published in Grady et al. (2004).

3.7 Conclusions

Nearby young stars serve as laboratories to study the evolution of circumstellar envelopes, disks and the birth of planetary systems. We carried out an adaptive optics-aided survey to study the environment of eleven young stars. These observations proved to be rather successful: we identified six new companion candidates, imaged the circumstellar envelopes of two stars and characterized the newly discovered small cluster around a Herbig Ae star. Probably the most interesting of the new companion candidates is the one close to FU Ori, the prototype of young outburst stars. We discuss the possible nature of this object and conclude that the observed properties are consistent with either a pre-main sequence star at the distance of FU Ori or – with much smaller probability – a red background giant star. We argue that intermediate-resolution optical or infrared spectroscopy can efficiently discriminate between these cases.

As the FUor outbursts may be of central importance for star formation, a possible companion to the prototype object FU Ori can have a major impact on the current outburst models. In particular, the close fly-by of the companion could lead to disk perturbations, therefore, providing an external triggering of the outbursts of FUor stars.

Our ALFA observations also yielded the discovery of additional candidates around the youngest Vega-type star V 372 Ori, the Herbig Be star V 380 Cep and around the less-known candidate young stars HD 31305, HD 282737 and HD 38224. The current imaging data set is insufficient to unambiguously determine the nature of these objects and spectroscopic follow-up observations are planned.

We also obtained the first multi-colour high-resolution near-infrared images of the nebulosity around SU Aur and AB Aur, which provide important information on these circumstellar envelopes. These images will be interpreted together with optical HST/STIS coronographic imagery in order characterize the envelope of these two stars. The morphology of the SU Aur envelope points toward the existence of an outflow cavity north-west from the star.

As a part of an international observing campaign we used the NACO/VLT instrument to obtain the first high-resolution, deep near-infrared images of the environment of the young Herbig Ae star HD 104237. These images show more than ten faint, red sources around the Herbig Ae star. Based on the NIR colours and on additional mid-infrared observations we conclude that at least three of these faint stars have infrared excess emission and thus are likely to be T Tauri stars. A comparison of the near-infrared photometry of these sources to theoretical isochrones suggest an age of $\sim$5 Myr for the association. Thus, the Herbig A star HD 104237 is situated in a loose cluster of young star, the second closest of such agglomerates.

These results also demonstrate, that the majority of the intermediate-mass young stars is not single but is part of loose associations. The most massive members often overshine the lower-mass companions, leaving them undetected and thus leading to a biased picture on the existence and composition of such small clusters. High-resolution, high-contrast infrared observations are, as shown here, necessary to identify the fainter population of stellar or substellar companions.

After studying the environment of some Herbig Ae and Be stars in this chapter, we continue by investigating young, massive OB stars. Their very short lifetimes ($t \sim 10^7$ yr) restricts the locations of the young massive stars to star-forming regions. In the following chapter we present observational results on the structure and properties of a prototypical massive star-forming region.

Chapter 4

Portrait of a High-Mass Star-Forming Region

A massive star of O9 spectral type is about a thousand times more luminous than an intermediate-mass A-type star and about ten thousand times more luminous than a Solar-type star (Lang 1991). In addition to the giant luminosity, the hot massive stars emit most of their radiation at wavelengths short enough to ionize the hydrogen atoms and evaporate dust particles. Therefore, unlike the low- and intermediate-mass stars investigated in the previous chapters, young massive stars strongly influence the regions where they form. On the other hand, the formation of massive stars is determined by the conditions in the parental molecular cloud. Therefore, understanding massive star formation requires detailed studies of the youngest massive stars *in their environment*.

In this chapter, we will study the bright far-infrared source IRAS 09002-4732 (RA: $09^h01^m54^s$ DEC: $-47°43^m59^s$, J2000) as a prototype for a region of massive star formation. This region was selected because of its proximity, brightness and the available high-quality archival near-infrared data. IRAS 09002-4732 is located in the direction of the Vela Molecular Ridge, but recent photometric study by Liseau et al. (1992) estimates a distance of about 700 pc, which places the region closer to us. Throughout this article we assume the conservative distance of 1.3 kpc which is consistent with the kinematic distance estimate provided by Wouterloot and Brand (1989).

The first hints for massive star formation in the region of IRAS 09002-4732 came from an early detection of the strong radio source G268.42-0.85 (Manchester and Goss 1969) which was later classified as an ultra-compact H II region (UC H II). This source coincides with an extremely bright far-infrared source discovered by Furniss et al. (1975). The presence and strength of the [NeII] line (Simpson and Rubin 1990), the radio flux (Walsh et al. 1998) and the high IRAS luminosity points to a spectral type of at least O9 if the ionizing source is a single star. Apart from the luminosity other signs of massive star formation such as water maser emission (Braz et al. 1989) and a massive molecular cloud core of 600 $M_\odot$ (Zinchenko et al. 1995) have been detected.

First evidence for the complexity of this massive star-forming region came from infrared images of the region obtained by Lenzen (1991). The images immediately reveal a very patchy distribution of matter. In addition, he found a cluster of infrared sources with the reddest and strongest mid-infrared object coinciding with the radio position. Using CS molecular line data, Lapinov et al. (1998) revealed a large-scale bipolar structure of the cloud.

The goal of this chapter is to use multi-wavelength data from the near-infrared to the radio regime in order to develop a comprehensive picture of this region of massive star formation. To reach this goal, we use high-resolution data obtained with ISAAC at the VLT, imaging and spectroscopic mid-infrared data, and a millimetre map. Sensitive and high-resolution near-infrared observations are essential to address the stellar census and the nebulosity; mid-infrared data are required to identify the main heating source of the intracluster dust. In the following, we describe the observations and data reduction. Based on the new data, we discuss the morphology, stellar content, reflection nebulosities, the UC H II region, the ionizing star and the spectral energy distribution (SED) of the region. Finally, we assemble a global structural picture of the region and summarize the main conclusions.

4.1 Observations and Data Reduction

The most important parameters of the near-infrared, mid-infrared, and millimetre observations are compiled in 4.1.1. In addition to these data, we will use archival MSX images and photometry (Egan et al. 1999), reprocessed IRAS fluxes (Ghosh et al. 2000), JCMT millimetre observations (Reipurth et al. 1996), and centimetre-wavelength ATCA radio measurements (Walsh et al. 1998).

4.1.1 Near-infrared 1 – 2.2 μm imaging

We used Js, H and Ks data retrieved from the ESO archive (courtesy L. Bronfman) to investigate the stellar content of IRAS 09002-4732. A mosaicing technique has been used to map a $4.25' \times 4.25'$ area centered on the IRAS source 09002-4732. Along the edges ($0.5'$) of the mosaic not every position has been covered. Every on-object frame was followed by an off-object frame with an offset of 30" in both RA and DEC directions to provide reliable background levels. To avoid the contamination of the sky frames by the extended nebulosity and stars, we combined the set of all images into a common sky frame. The combination was done by comparing the values of each pixel in every frame and taking the mean of the lowest 1/3 of them. This procedure effectively removed the imprints of any object brighter than the average sky background and, therefore, led to a homogeneous sky frame.

Additionally, the off-object frames have also been used to extend the available field of view. The detector integration time (DIT) was 1.7 s, i.e. the shortest possible exposure time to avoid saturation by bright stars. On each on-target position the 1.7 s exposure has been repeated 62 times (NDIT) and averaged. Depending on the dithering pattern, some individual positions have been consequently repeated, enhancing the signal-to-noise ratio (S/N) in the centre of the images.

The reduction of the frames and the composition of the mosaic images have been performed by an IDL pipeline (Stecklum et al. 2003). After reducing the individual frames, applying the standard dark current, flat field and bad pixel corrections, the field distortion has also been corrected following the polynomial transformation given in the ISAAC reduction recipe at the ESO web site http://www.eso.org/instruments/isaac/problems_tips.html. Since the flat field correction was not reliable along the edges of the chip, the outermost lines and columns have been ignored.

After the assembly of the mosaic, aperture and PSF photometry has been performed on the Js, H and Ks band images, using the DAOPHOT package of IRAF. Due to the strongly varying background nebulosity and the densely populated innermost regions, the PSF photometry proved to be the most suitable method for measuring the stellar fluxes. The detection levels were fine-tuned and carefully checked to optimize the result.

The PSF was constructed from the best 25 star profiles, where no saturation, chip edge or neighboring star could be seen. During the PSF photometry, the PSF was scaled to the profile of each star; the scaling factor depends linearly on the brightness of the individual sources. Following the PSF photometry of the three frames, the identified stars were cross-checked between the different filters. In order to exclude misidentifications, the maximum allowed shift of a star in the different filters was smaller than 1 FWHM of the PSF. The number of stars measured in all three band amounts to 263. The brightness of the faintest objects identified as stars were 19.5, 18.4 and 17.0 magnitudes in Js, H and Ks, respectively. We take these values as the limiting magnitudes of the observations.

The flux calibration was based on the ESO standard star FS19 (Casali and Hawarden 1992) in the Js and H band and on the standard star S875-C (Persson et al. 1998) in the Ks band. The standard star images were processed using the same pipeline settings as for the science frames. To increase the accuracy of the calibration, aperture photometry was applied to the standard stars and this value was transfered to the PSF photometry of the science frames using an aperture correction. The aperture correction was established by comparing the aperture and PSF photometry for at least 5 stars on each science frame.

The statistical error of the photometry (i.e. fit error of the PSF) is better than 0.1 magnitudes for the majority of the stars; however, the strong fluctuations of the nebulosity throughout the field influenced the local photometric accuracy. Since the standard calibration process provided by ESO placed the standard stars far in time from the science objects, the error of the absolute photometry can be somewhat higher than 0.1 magnitude.

The composed mosaic has been compared to the US Naval Observatory Catalog (Monet et al. 2003) and an astrometrical reference frame has been established using 8 stars, which are both present on the images and in the Catalog. The achieved positional accuracy is typically better than $0.5''$.

Instrument	Wavelength [μm]	FWHM [$''$]	Field of View	Integr. time [s]	Date
ISAAC/VLT	Js = 1.2	0.6”	$4.25' \times 4.25'$	843.2	1st May 1999
ISAAC/VLT	H = 1.6	0.6”	$4.25' \times 4.25'$	1757.8	1st May 1999
ISAAC/VLT	Ks = 2.2	0.4”	$4.25' \times 4.25'$	2636.7	10th April 1999
ISAAC/VLT	L = 1.2	0.5”	$15'' \times 15''$	237.6	1st June 2001
ISAAC/VLT	Brα = 4.09	0.6”	$15'' \times 15''$	431.2	1st June 2001
ISAAC/VLT	M(nb) = 4.66	0.5”	$15'' \times 15''$	415.8	1st June 2001
TIMMI2/3.6m	M = 4.6	0.6”	$40'' \times 40''$	424	14th March 2001
TIMMI2/3.6m	N1=11.9	0.8”	$40'' \times 40''$	807	14th March 2001
TIMMI2/3.6m	12.9	0.8”	$40'' \times 40''$	1451	14th March 2001
TIMMI2/3.6m	Q = 20	1.4”	$40'' \times 40''$	1008	14th March 2001
TIMMI2/3.6m	N-Spectr.	0.8”	$3'' \times 60''$	510	14th March 2001
SIMBA/SEST	1.2 mm	24”	$9.3' \times 15'$	100	16th July 2003

Table 4.1: Log of the observations. The instruments and telescopes, filter names and central wavelengths, FWHM of point sources, final useful field of view, total integration times and the dates of the observations are given.

4.1.2 Near-Infrared 3 – 5 μm imaging

To investigate the warm dust around the UC H II region G 268.42-0.85 region, we carried out imaging at wavelengths between 3 and 5 μm. We applied three filters: L, narrow band 4.07(nb) centered on the Brα line and narrow band M(nb). The central wavelengths/widths are as follows: 3.78/0.58, 4.07/0.08 and 4.66/0.10 μm, respectively. A $15''$ chopping throw in N-S direction was applied.

During the reduction process bad pixel filtering, flat field correction and simple shift-and-add beam combination have been used. The chopping throws were too small to provide good background subtraction and made large parts of the images useless. In the following, we only consider the direct vicinity ($15'' \times 15''$) of the UC H II G268.42-0.85 , which is by far the brightest object in the image and thus can be regarded as undisturbed by the imperfect background subtraction.

For flux calibration we used the standard star HR 5494, which was observed with identical DIT times. However, this star does not have previous flux measurements in the Brα filter nor in the M-band. To overcome the unknown flux problem, we used a blackbody extrapolation to predict the fluxes in question. This method, however, is less reliable for the determination of the emission line flux.

To inspect the distribution of the Brα line emission the subtraction of the continuum from the Brα images is necessary. Because no narrow-band continuum image at wavelengths close to the Brα filter was taken, we composed the continuum image by interpolating between the L and M(nb) filters; this continuum image was then scaled to cancel out the line emission from two stellar objects.

4.1.3 Mid-infrared imaging

The thermal infrared images were acquired during our guaranteed time program on the TIMMI2 camera at the 3.6m ESO telescope. The object was observed in the filters M (4.30 – 4.99 μm), N11.9 (10.61 – 12.50 μm), N12.9 (11.54 – 12.98 μm), and Q+Si (19 μm – atmospheric cut-off). Both the north-south chopping throw and the east-west nodding throw were selected to be 40$''$ in all filters. In addition, a 11.9 μm measurement was performed with 18.5$''$ chopping throws and 20$''$ nodding throws. The pixel size was 0.2$''$/pixels for the 11.9, 12.9 μm and the Q filters and 0.3$''$/pixels for the M-band observations.
During the reduction process the video frames were summed up, neglecting the first three frames after each repositioning to eliminate image distortions from the vibration of the secondary mirror. A sigma-filtering process has been used to remove the bad pixels. Thereafter the positive and negative beams have been extracted and combined. To avoid any overlap between the negative and positive beams of the extended source, subimages with the dimensions of the chopping/nodding throws were extracted. The ESO standard stars HR 91797 and HR 123139 have been used as flux calibrators. The calibration of the 20 μm science frame was not possible because the standard star was not present in the calibration images.

4.1.4 The N-band Spectrum

Spectroscopy of IRAS 09002$-$4732 between 8 and 11.5 μm was performed with TIMMI2 with a spectral resolution of 120. Since the 10 μm grism was not yet available for these observations, the 20 μm grism had to be used in second order. Therefore, the 12.9 μm [NeII] line was not covered by the spectrum. The slit of 3$''$ width was oriented north-south and centered on the mid-infrared peak. A chopper throw of 10$''$ was applied. The star Sirius served as spectroscopic standard star. The spectrum was calibrated using the atmospheric opacity derived from the standard star observation and the ISO SWS full scan spectrum of Sirius retrieved from the ISO archive. For the data reduction we used the TIMMI2 pipeline by Siebenmorgen et al. (2004).

4.1.5 SIMBA 1.2-mm mapping

The 1.2 mm continuum observations were carried out with the 37-channel bolometer array SIMBA (Nyman et al. 2001) at the SEST on La Silla, Chile. SIMBA is a hexagonal array in which the HPBW of a single element is about 24$''$ and the separation between elements on the sky is 44$''$. The observations were made using a fast–mapping technique without a wobbling secondary (Weferling et al. 2002). The raw data were reduced with the MOPSI mapping software package developed by R. Zylka (IRAM, Grenoble, France), using a deconvolution algorithm to remove the contribution of the electronics arising from the fast-mapping observing mode. Maps of Uranus were taken to check the flux calibration

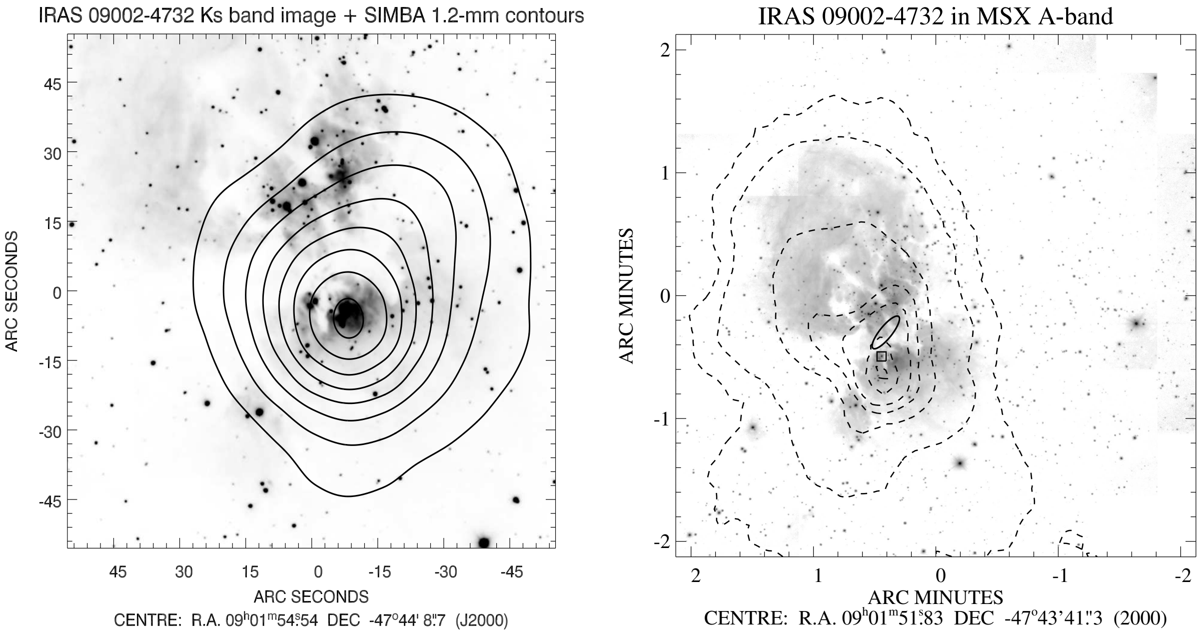

Figure 4.1: *Left Panel:* 1.2 mm SIMBA/SEST contours overlaid on grayscale ISAAC Ks-band image. *Right Panel:* MSX 8.28 μm contours, showing an extended, continuous distribution of warm dust in the star-forming region. The contours mark 5, 10, 50, 100, 150, 250, 300 σ levels; the MSX point source flux is 30.74 Jy. The inverted gray scale ISAAC Ks image shows the stellar population and the short-wavelength nebulosity. The square marks the radio position of the UC H II G268.42-0.85, while the ellipse indicates the positional error ellipse of the IRAS point source 09002-4732. The MSX A-band images are influenced by PAH emission and this explains the offset between the IRAS- and MSX-peaks.

of the resulting data. To correct for the atmospheric opacity, skydips were performed every 2–3 hours. Despite the occurrence of some thin clouds, the observing conditions turned were good which is reflected in zenith opacity values of 0.16 – 0.18. The pointing was checked roughly every two hours and proved to be better than 6″. The combination of three maps with sizes of 560″ × 900″ resulted in a residual noise of about 46 mJy/beam (rms).

4.2 Results

In this section the observational results are described in the following sequence: First the overall morphology and stellar content of the star-forming region (SFR), then the intracluster material, and finally the properties of the UC H II region are presented.

4.2.1 Global Morphology of the Star-Forming Region

We used the infrared observations, ranging from 1.2 μm to 20 μm, the 8.64 GHz radio continuum observations of Walsh et al. (1998), our 1.2 mm SEST map as well as CS J=7-6 line measurements by Lapinov et al. (1998) to analyze the structure of the star-forming region IRAS 09002-4732. Figs. 4.1 and 4.2 summarize the global features of this region.

The near-infrared images of the region show a large number of red stars surrounded by a large bipolar nebula (cf. Fig. 4.1). The two lobes of the nebula are separated by a dark lane extending in east-west direction. The thermal dust emission in the MSX A-band (8.28 μm) resembles the Ks-band morphology. However, the distribution of the 8.28 μm flux does not show any multiple or bipolar structure as does the Ks-band image. This fact could be understood if the prominent dark lane and several other dark patches in the Ks image are introduced by filaments of dense, warm dust in front of the roughly homogeneous nebulosity.

The MSX A filter also includes emission bands of interstellar PAH molecules that are often widely distributed. The MSX E band, however, is not known to include such PAH features. The similar appearance of the A and E band images of IRAS 09002-4732 indicates that the overall morphology of the large–scale MIR emission is not *dominated* by the emission from PAH molecules and hence traces mainly the warm dust. The slight shift of the MSX A peak relative to the UC H II region is certainly the result of the PAH emission: the MSX E-band emission peaks only $\sim 4''$ from the UC H II region, comparable to its resolution.

The 1.2-mm SIMBA map (Fig. 4.1) shows a moderately resolved region of strong emission. The emitting region has an elliptical shape with the major axis oriented in north-NW–south-SE direction similar to what has been measured in the CS (2-1) line by Zinchenko et al. (1995). The emission mainly covers the middle and northwestern part of the dark lane seen in the NIR as well as the southern lobe of the MIR emission. The peak emission at 1.2 mm is located in the southern lobe and is slightly displaced ($13.5''$) from the location of the IRAS peak. Assuming the emission at 1.2 mm wavelength to be optically thin thermal dust radiation and using the canonical gas/dust mass ratio of 100, we can obtain the total mass M of the region:

$$M = \frac{S_\nu D^2}{\kappa_\mathrm{m} \times B_\nu(\nu, T_\mathrm{d})}$$

Here, S_ν is the flux density, D is the distance, T_d the dust temperature and κ_m the mass absorption coefficient per gram gas with a value for T_d of 80 K (see Sect. 4.2.5) of 0.01 cm^2 g^{-1} (Ossenkopf and Henning 1994). We obtain a total mass of about 100 $M_\odot$ which is significantly lower than the 600 $M_\odot$ derived from CS J=2-1 observations Zinchenko et al. (1995). A variety of factors can contribute to this discrepancy, including the dust-to-gas mass ratio, the uncertainty in the mass absorption coefficient, and the CS abundance.

These large–scale observations, however, show that the main heating source of the dust is in the southern lobe. In fact, the most massive star(s), indicated by the presence of an UCH II region, is located close to both the MSX and the SIMBA peak emission (see Fig. 4.1).

Fig. 4.2 shows the Maximum Entropy Method (MEM) deconvolved CS J=7-6 contours which trace relatively warm and dense gas. We now see two very similar clumps which have only a small line-of-sight velocity difference (Lapinov et al. 1998). The southern clump coincides with the extinction lane outlined in the overlaid Ks band image. The lack of stars in this region points to the fact that this extinction structure is located in front of the stellar cluster. In contrast to this situation, the northern CS clump does not appear as an extinction structure in the NIR map, indicating a location behind the stellar cluster.

All the millimetre line and continuum data have a rather coarse resolution of $\sim 24''$. In contrast, the JHKs composite image (see Fig. 4.3) provides a picture of the region with subarcsecond resolution. It immediately shows the inhomogeneous extinction structure around IRAS 09002-4732. We will discuss this structure in more detail in the next section.

4.2.2 Structures on Smaller Scales

Reflection Nebulosity

South-west of the UC H II G268.42-0.85 the optical/near-infrared emission is dominated by blue scattered light. This reflection nebulosity was first identified as Bran 222 by Brand et al. (1986) and has a size of roughly $1' \times 1'$. To find the source that illuminates this nebula, we plotted the observed J-band surface brightness versus the distance from the UC H II G268.42-0.85 in Fig. 4.4. Here the surface brightness was integrated over $1'' \times 1''$ squares and background-corrected. The positions for measuring the surface brightness were selected manually to minimize the contamination by extinction, stars or foreground filaments. Fig. 4.4 clearly shows an increasing surface brightness towards the UC H II G268.42-0.85, which demonstrates that the source of the scattered light lies close to the location of the UC H II. We note that an unambiguous identification of the illuminating source could be provided by polarimetric observations using adaptive optics (see, e.g., Henning et al. 2002).

Dark Filaments and Globules

Numerous dense dust structures are visible as dark silhouettes in front of the bright surface of the reflection nebulosity. Our high-resolution NIR image (see Fig. 4.3) gives a stunning view on the dust content of the region, proving that a significant amount of the dust is concentrated in string-like filaments, criss-crossing the face of the cluster. We outline their positions in Fig. 4.5 with five of the most interesting filaments tagged as S1 to S5. The designation was only chosen to guide the reader. These filaments were selected with the following definition in mind: continuous, elongated areas of high extinction with sharp, well-defined borders. Filaments S1, S2 and S5 are remarkably confined and their typical length/diameter ratio is of the order of 40.

A closer inspection of the NIR surface brightness of the filaments shows strongly varying optical depths along their extent. We observed small ($< 5''$) regions of increased extinction *inside* the dark filaments that we interpret as arising from dense globules (see Fig. 4.3).

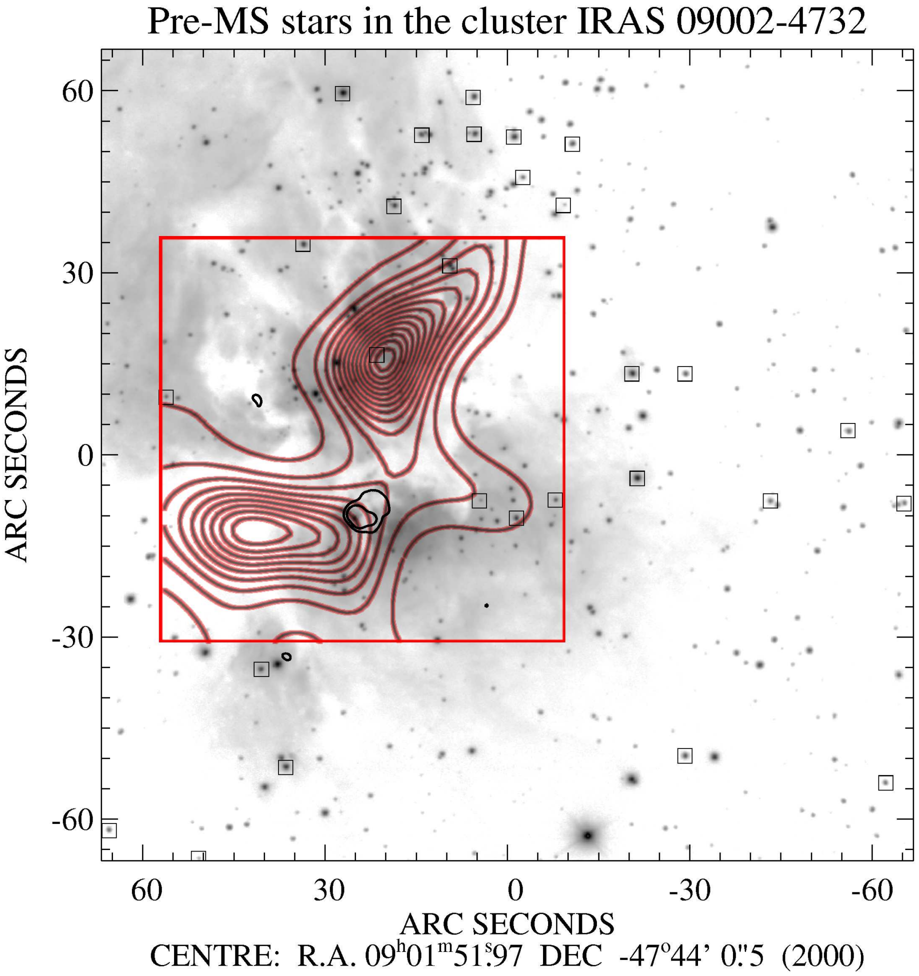

Figure 4.2: MEM deconvolved CS J=7-6 contours (vel. channel 2.75 km/s, Lapinov et al. 1998) overlaid over the central region of the inverted Ks-band ISAAC image. The CS J=7-6 line transition shows two, very similar clumps with only a small line-of-sight velocity difference. The gray scale Ks-image shows similar structure in extinction, but suggests that the SE clump is located in front of the cluster while the NW clump is located behind the embedded stars. The squares mark stars with NIR excess larger than 0.1 mag. The large red rectangle marks the approximate field of view of the CS observations.

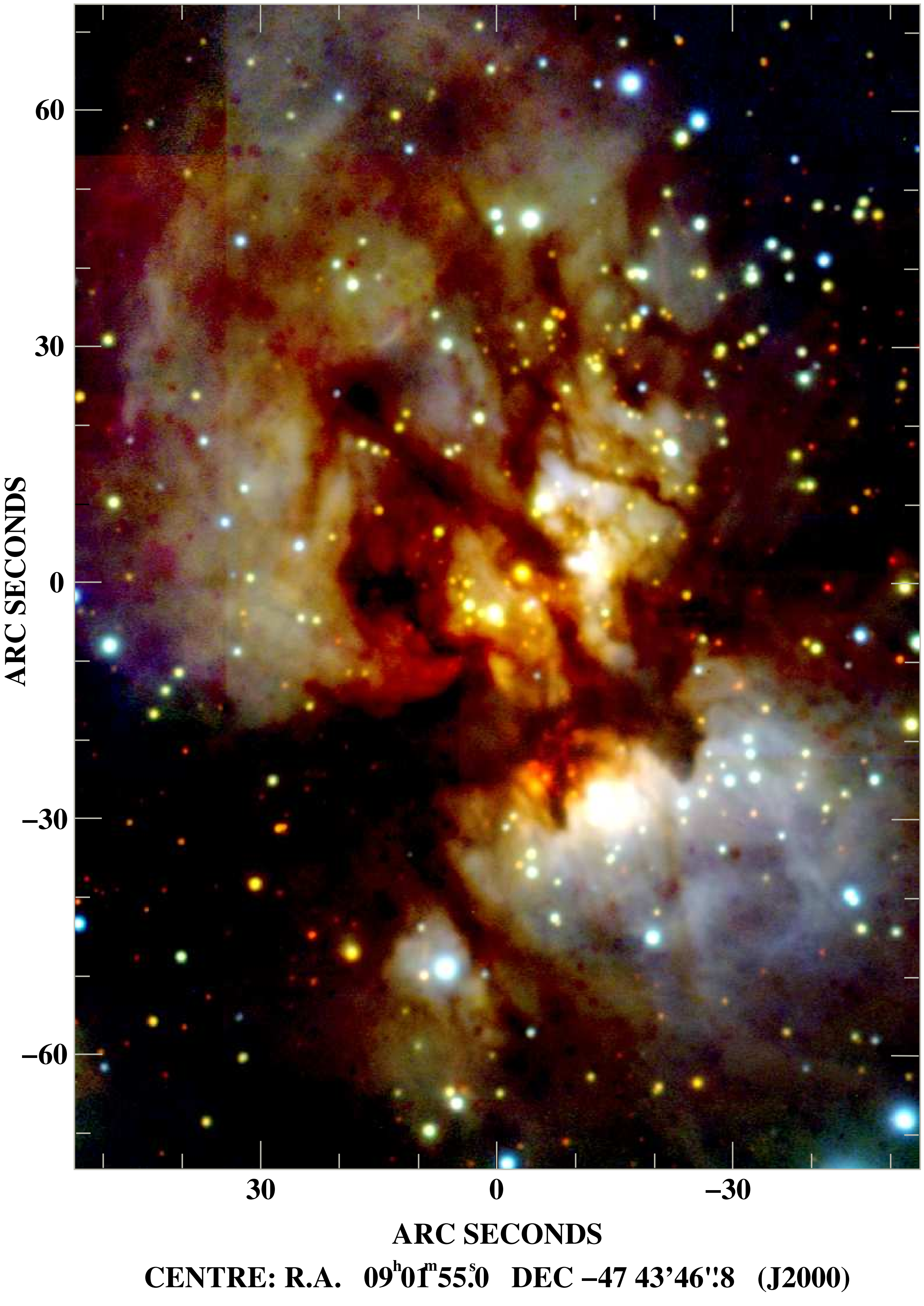

Figure 4.3: False-colour composite image from the near-infrared observations. The Ks band image is coded in red, H in green and J in blue.

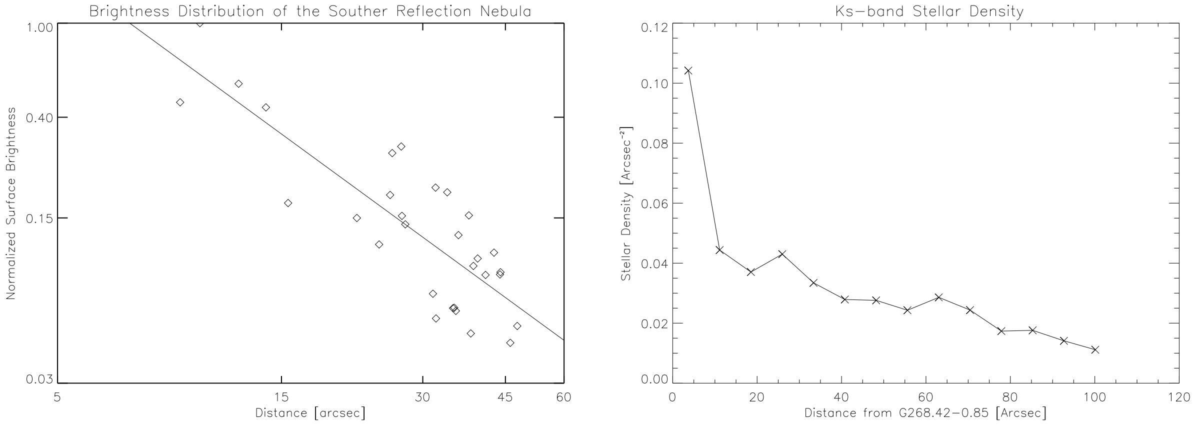

Figure 4.4: *Left Panel:* J-band surface brightness of the reflection nebulosity versus the distance from the UC H II G268.42-0.85 plotted on a logarithmic scale. The best fit gives an $R^{-1.4\pm0.2}$ dependence. *Right Panel:* Ks-band stellar density derived from stellar counts in concentric annuli around the UC H II G268.42-0.85.

After identifying the objects on the colour composite image (Fig. 4.3), Fig. 4.5 outlines the positions of 15 globules identified in the inner part of the star-forming region. Tab. 4.2 gives an overview of their estimated properties. The extinction values given here have been derived from the comparison of the surface brightness inside and outside (averaged at three locations) of the globule. We note that the objective characterization of such dark, diffuse objects is rather difficult; their list is certainly incomplete and the values given in Tab. 4.2 should be taken with caution. Therefore, we have not made an attempt to derive further parameters such as column densities or masses. This remains the task of follow-up projects, possibly using millimetre interferometry.

While most of the dark globules are located inside the filaments and should be considered as part of the overall structure of cold dust, we also see some isolated, compact ($d < 2''$) objects as faint silhouettes against the foreground of the evenly illuminated southern reflection nebula (an example is IS2, compare Fig. 4.3 and Fig. 4.5). In addition, we find a very faint bright-rimmed object (IS1) which looks more similar to a proplyd. Although these small (<1300 AU) and dense isolated objects are similar in appearance to those identified as proplyds in Orion, some important differences have to be noted. The resolution and sensitivity of our current data set does not allow the detection of silhouette structures at scales of the typical Orion proplyds (∼100 AU), but only of significantly larger structures (∼700 AU). Although proplyds of this size are not unheard of (see, e.g. McCaughrean and O'dell 1996; Bally et al. 1995), current evidence does not allow a final conclusion concerning the nature of these objects. High-resolution narrow-band imaging of the region would be necessary to find more of these silhouettes and to explore their nature.

Although the existence of the isolated globules IS1 and IS2 has been confirmed in the individual J, H and Ks band mosaics obtained with different dithering patterns, we can not completely exclude the possibility that they are artifacts from the imperfect sky sub-

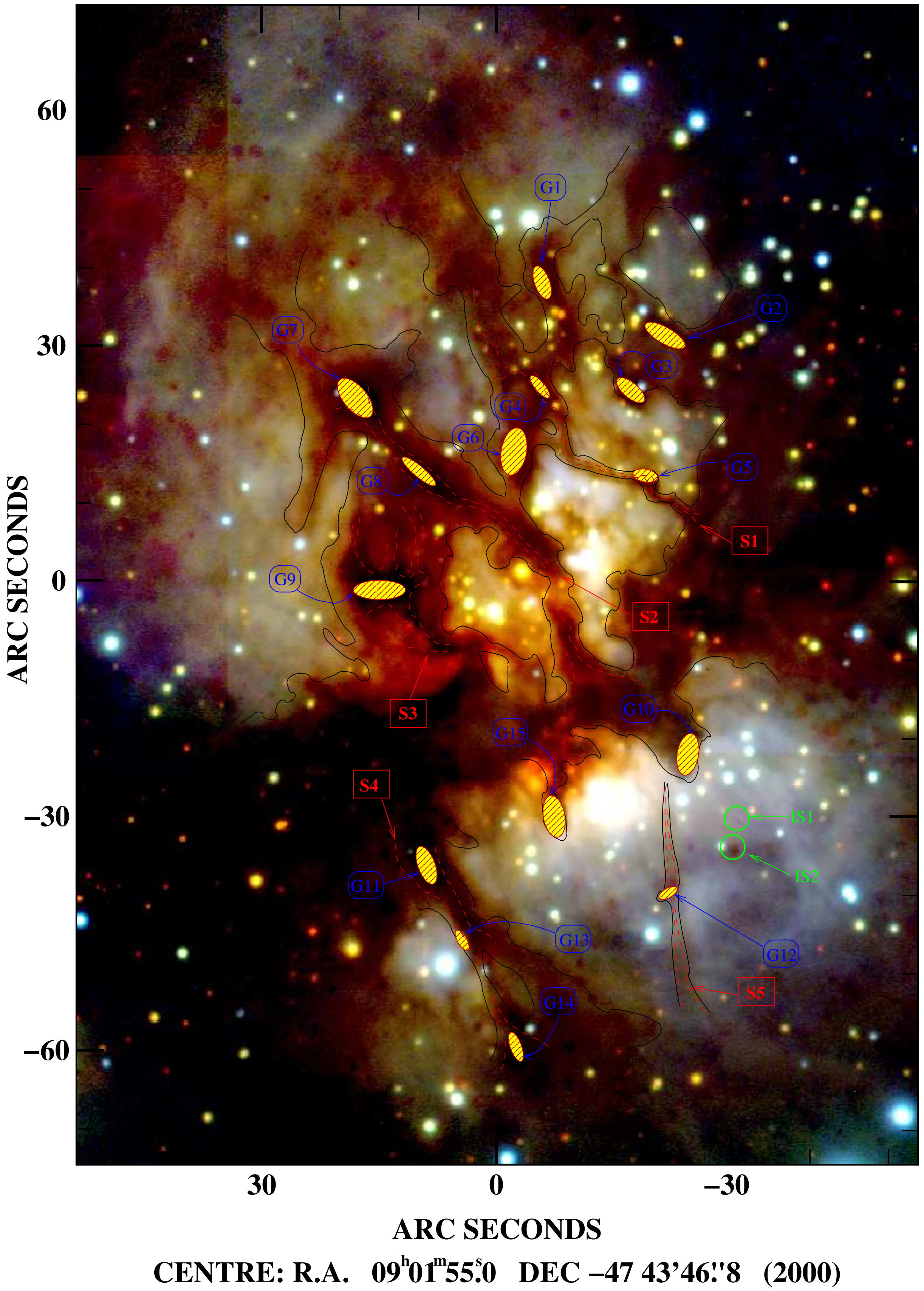

Figure 4.5: Outlines of the filamentary structure of extincting material seen in the NIR images. The solid lines trace the general structure, while the dashed lines indicate the dark filaments (S1-S5). The dense globules inside the filaments are indicated with hatched ellipses and designated as G1-G15. The two circles (IS1 and IS2) mark two isolated silhouette objects.

Globule ID	H_{out}-H_{in} [$\times 10^{-5}$ Jy/arcsec^2]	Extinction [H-mag/arcsec^2]	Dimensions " × "	Axis Ratio	Note
G1	4.0	2.4	4.2 × 1.6	2.6	
G2	2.16	1.3	3.5 × 1.5	2.3	
G3	9.3	3.5	2.6 × 1.0	2.6	
G4	3.8	> 3.7	2.9 × 0.9	3.2	
G5	8.6	2.8	2.6 × 0.9	2.9	
G6	17.3	> 1.6	3.8 × 1.7	2.2	
G7	6.1	> 4.0	4.0 × 2.8	1.4	
G8	4.6	> 3.8	3.9 × 0.8	4.9	
G9	10.0	> 4.6	6.5 × 3.0	2.2	
G10	13.3	2.3	3.3 × 1.2	2.8	
G11	5.0	> 4.0	5.0 × 2.2	2.3	Larger?
G12	7.3	1.5	2.6 × 1.4	1.9	
G13	7.4	3.3	3.3 × 1.4	2.4	
G14	4.5	3.2	5.9 × 2.6	2.3	Double?
G15	28.2	3.2	4.9 × 1.6	3.0	

Table 4.2: Catalogue of the dark globules and their estimated properties. Their assigned number, H-band surface brightness difference inside and outside of the globule, the derived extinction, approximate dimensions and axis ratio together with additional notes are given. For their location and orientation see Fig. 4.5.

traction.

The remarkably long and confined dark filaments in IRAS 09002-4732 are very similar in appearance to the *globular filaments* observed in the field, i.e. not associated to any star-forming region (Schneider and Elmegreen 1979). Similar, but larger-scale filamentary structures also seem to be characteristic to the distribution of both the molecular gas and young stellar objects in the Taurus star-forming region (Hartmann 2002 and references therein). Although the detailed comparison of these filamentary structures of different ages and environments is outside of the scope of this work, we note some interesting points.

The most exciting question concerning these filaments might be their origin. Do they represent an early stage of collapsing cloud material or are they confined and shaped by the influence of the newly born young stars? If the globules embedded in the filaments are indeed collapsing, these chains of protostars could provide the next generation of young stars in the region similar to the situation observed in the Taurus SFR (Hartmann 2002).

The density of the globules/filaments drops in the southern lobe of the reflection nebulosity, which as shown in Sec. 4.2.2 is directly influenced by the massive star ionizing the UC H II G268.42-0.85. Therefore, we speculate that the massive star could have destroyed these structures, while the undisturbed northern filaments could represent the young counterparts of the globular filaments described by Schneider and Elmegreen (1979).

4.2.3 Stellar population of the Star-Forming Region

We identify more than 1100 stars in the vicinity of the IRAS source 09002-4732 in our ISAAC NIR mosaic images over a field, 263 of them having reliable photometry in all three (J, H and Ks) filters.

In order to probe if these stars show any clustering we calculated the stellar density in Ks-band as a function of distance from the UC H II G268.42-0.85 . We used concentric annuli with width of 7.5″ to integrate the stars identified in Sect. 4.1.1. The number of stars in each annulus has been divided by the area of the annulus in arcsec^2 to derive the apparent stellar density. The outer diameter of the area investigated with this method was about 3.3′, excluding the incompletely covered and noisy peripherical areas of our NIR mosaic. The resulting plot is shown in the right panel of Fig. 4.4. An increase in stellar density towards the UC H II G268.42-0.85 is obvious from the plot, with a strong rise in the central 20″. This increase argues towards a clustering of the stellar sources in the vicinity of the IRAS source 09002-4732.

As demonstrated in Chapter 3.3.1 the NIR colour-colour diagram is a useful tool for interpreting the nature of stellar objects. We plot the colours of all stars with reliable NIR photometry in Fig. 4.6. The NIR colours of most of the stars in the diagram are consistent with the colours of heavily reddened main-sequence star, i.e. they lie in the reddening lane. The infrared colour excess E(H−K) of these stars detected in all three NIR filters range from 0.2 to 2.0 mag, corresponding to visual extinctions between $A_V \simeq 3.0$ and 30 mag (Mathis 1990). The upper value here reflects our sensitivity in the J-band. As Fig. 4.6 shows a large fraction of the stars display excess emission in the NIR bands, i.e. they lie below the reddening lane. We identify 63 stars displaying significant (> 0.1 mag) NIR excess emission, indicating their youth and pre-main sequence (PMS) nature (see, e.g. Lada and Adams 1992 or Li et al. 1997). Although the different types of young stellar objects (T Tauri stars, Herbig Ae/Be stars, Class I, etc.) have characteristic positions in the colour-colour diagram, these groups are not distinct. Therefore the classification of these source based only on J-H and H-Ks band colours is not possible (see Lada and Adams 1992). Additional information on the luminosity of these objects is obtainable from their apparent magnitudes, but their unknown distances and reddening makes their classifications ambiguous.

Such a concentration of young PMS stars, supported by the increase in the stellar density, is an evidence of a young stellar cluster, with recent or on-going star formation.

The celestial positions of the stars with known NIR excess emission are shown in Fig. 4.2. Although these stars appear to form two loose associations in front of the northern reflection lobe and in the south-west part of the region, we stress that this distribution is likely to be caused by extinction.

In order to better understand the effects of extinction in Fig. 4.7 we also show the NIR colour-magnitude diagram. The symbols used here are identical to those used in the colour-colour diagram. This diagram compares of the stars' apparent magnitudes and colours to those of zero age main sequence stars seen from 1.3 kpc. The strong reddening of the stellar population in IRAS 09002-4732 is again evident, but the distribution of the reddened stars along the J-K axis is closely continuous and does not reveal clustered reddening.

A comparison of our limiting magnitudes to the 1 Myr old pre-main sequence isochrones of Schaerer et al. (1993) shows that – assuming an extinction of A_K=1 mag and a distance of 1.3 kpc – our sensitivity is sufficient to detect stars with masses down to 0.8 $M_\odot$ in the Ks-band. The sensitivity limit (expressed in solar masses) is slightly worse for main-sequence stars, where our Ks-band imaging reaches the 1 $M_\odot$ limit (Bessell and Brett 1988; Lang 1991).

Assuming that all PMS stars belong to the cluster around IRAS 09002-4732 it is worthwhile to compare their number to the similar values in the well-known young stellar cluster in Orion. Hillenbrand (1997) finds ∼60 stars in the OBAFG spectral type range (in the inner 2.5 pc of the Orion cluster). Our images show in a similar field of view (∼3 pc × 3 pc) similar number of young stars (∼ 63) in this spectral range. The disk lifetimes and cluster ages, as well as the massive and highly varying extinction, however, may strongly influence this comparison.

4.2.4 The UC H II Region

In the following we discuss the infrared morphology of the UC H II region, its spectral energy distribution and investigate the spectral type and luminosity of the ionizing star.

Morphology of the UC H II Region

The direct vicinity of a new-born massive star is one of the most hostile stellar environments. The intense ultraviolet radiation and stellar wind rapidly evaporates the dust particles, dissolves accretion disks and protostellar sources as seen in the case of the Orion Trapezium (O'dell 2001), M16 (Hester et al. 1996) or M8 (Stecklum et al. 1998). However, these processes also render many, otherwise invisible low-mass objects and structures visible. The question of the existence of photoevaporating disks around massive stars is of central importance, since this could support evidence for the disk accretion being possible even for massive stellar objects (see, e.g. Chapter 5 or Yorke and Sonnhalter 2002). Furthermore, the study of the photoevaporating objects can constrain the timescale of the H II region's evolution and its low-mass stellar content. Answering these exciting questions requires multi-wavelength, high-resolution deep imaging.

Our images cover the wavelength range between 1 and 20 μm, giving a detailed look into the stellar content and the circumstellar material. Fig. 4.8 shows the region centered on the radio continuum peak in bands Ks, L, 4.07 μm, M, 11.9 μm, 12.9 μm, with the radio continuum intensity overlaid as contour lines. We identify more than 15 objects in the $20'' \times 20''$ field of view of the images, 9 of them detected in more than one filters. In the following we discuss these 9 objects, assigned with letters A–I. For the nomenclature and locations see Fig. 4.8 and for the summary of the fluxes we refer to Tab. 4.2.4.

Source A: Located 1.7" east and 9.57" south of Source D. This source remains unresolved in all our images, pointing to a diameter of less than 700 AU.

Source B: 2.7" east, 6.5" south of D. Very red (H-K>2.8 mag) point source.

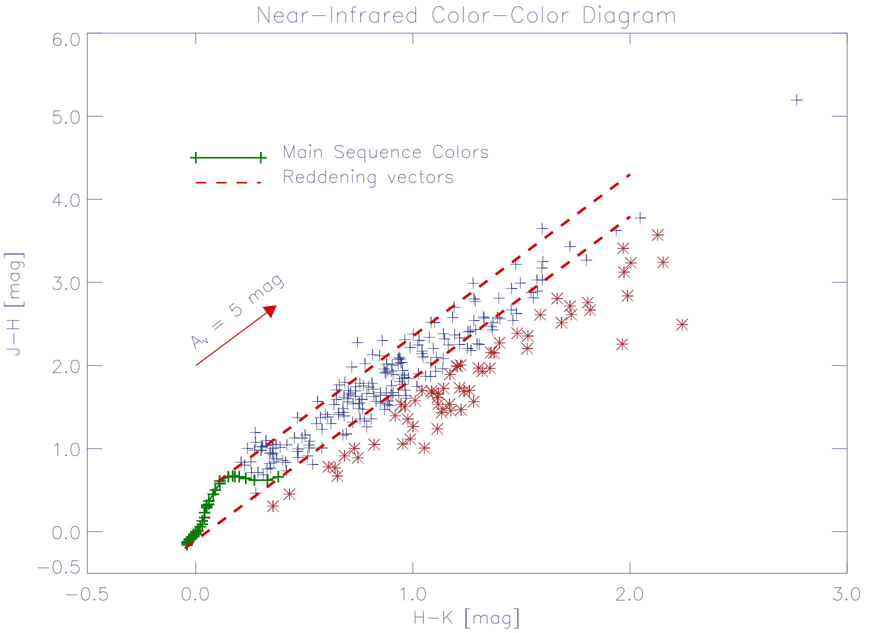

Figure 4.6: Colour-colour diagram of the stellar population around IRAS 09002-4732. The colour index (J-H) is plotted against the (H-K) index. The crosses indicate the colours of stars classified as reddened MS, the asterisks represent the stars NIR excess larger than 0.1 mag, while the dashed lines border the possible colours of the main sequence stars (Bessell and Brett 1988; Wegner 1994).

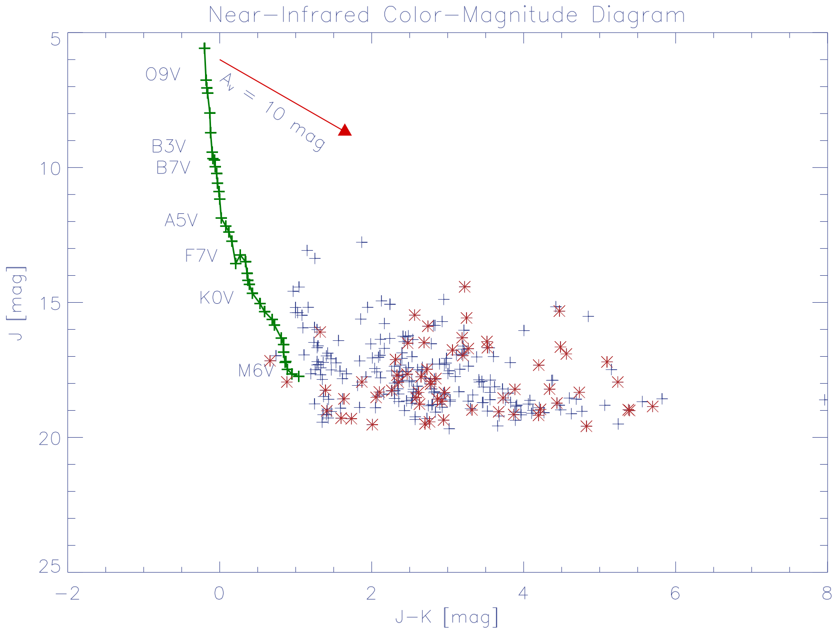

Figure 4.7: Near-infrared colour-magnitude diagram of the same stellar population. The symbols are identical to those used in Fig. 4.6. The assumed distance of the zero age main sequence stars is 1.3 kpc.

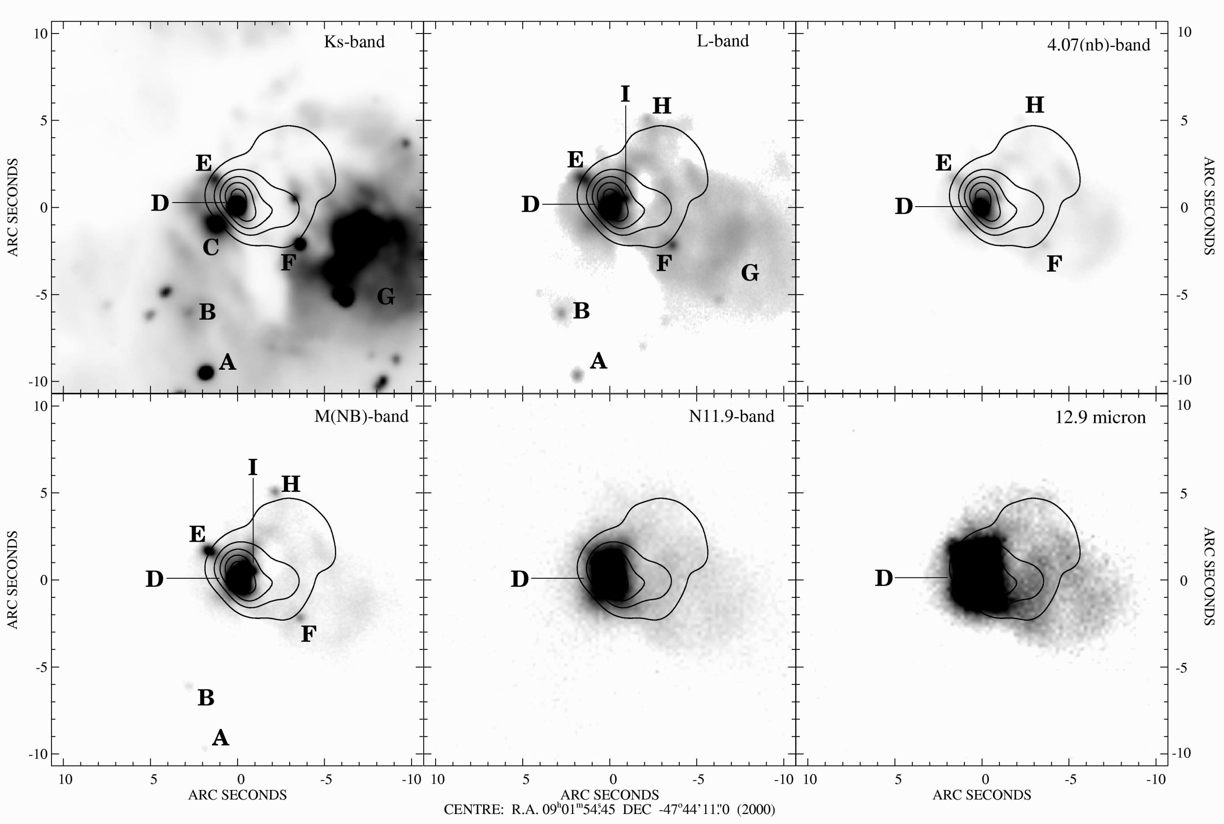

Figure 4.8: The morphology of the UC H II region G268.45-0.85 as seen in Ks, L, M(nb), 4.07(nb), 11.9μm and 12.9μm images. The overlaid contours are 8.64 GHz radio continuum measurements from Walsh et al. (1998). The objects of particular interest are marked with letters from A-I. The resolution of the images are as follows $d(Ks) \simeq 0.44'' = 600$ AU, $d(L) \simeq 0.45'' = 590$ AU, $d(4.07\mu m) \simeq 0.6'' = 780$ AU, $d(M) \simeq 0.47'' = 610$ AU, $d(11.9\mu m, 12.9\mu m) \sim 0.8'' = 1040$ AU.

Source C: 1.1" east, 1.1" south of D. Only present in J, H and Ks images. Extended source, most probably reflection nebula. It is brighter in H and Ks than in Js. This nebula lies in the direction, in which the UC H II region has its strongest decline in intensity and smallest extension (measured from its peak), as well as the direction of increasing CS density (Lapinov et al. 1998, see Fig. 4.2).

Source D: This NIR peak is coinciding with the radio peak G268.42-0.85 within our astrometric accuracy and therefore is expected to be the NIR counterpart of the most massive star. The peak is not separable from the background nebulosity in J, while in H and Ks it appears as a point source surrounded by a fainter halo. In L-, Brα- and M-band this source is extending in north-west direction with an extension up to $5''$. Its emission is increasing towards longer wavelengths. Longwards of 3 μm this thermal emission dominates the region. Source D remains a strong, extended source even in our 11.9 μm images. The spectral energy distribution and the spectral type of the underlying source is analyzed in Sec. 4.2.5.

Source E: 1.2" east, 1.6" north of D; a very red object, elongated in L- and M(nb)-bands. Its dimensions in L-band are 0.8" × 0.5". We note, that diffraction on the supporting structures of the secondary telescope mirror might also contribute to the elongated shape of this object.

The positions of the Ks-, L- and M-band peaks of source E are not coinciding, but are slightly shifted: the shorter the wavelength is, the closer the peak lies to source D, the ionizing source of the region. This shows that the part pointing towards the massive star is the hottest, suggesting the importance of external heating for this clump.

Source F: 3.4" west, 1.7" south of D; red (H$-$K=3.8 mag) point source.

Source G: Large, extended nebulosity close to the western edge of the Fig. 4.8. It is very bright in the J, H and Ks-band, while its intensity drops rapidly towards the longer wavelengths. We note, that the warm dust is extending westward from Source D, but the structure visible at 11.9 μm and 12.9 μm bands has different size and morphology than nebulosity G.

Source H: 5.4" north, 2.0" west of Source D; very red (K$-$L>6.1 mag) source, undetected in Ks-, but strong in L- and M-band.

Source I: ~0.5" north, ~1" west of Source D; an unresolved, very red (K$-$L=7.4 mag) source, which is strong in the L- and M(nb)-bands.

The continuum-subtracted Brα image traces well the nebulosity around the object D and indicate the presence of ionized emission from the Sources D and E (see Fig. 4.8).

Based on these observations we draw the following conclusions:

1. The neighbourhood of the massive star: The direct environment of the star ionizing the UC H II region is not devoid of stars; we identify more than 15 objects in the multi-wavelength images, many of them presumably being stellar sources with infrared excess emission. The most massive star's infrared counterpart has also been identified as Source D. This object dominates the infrared images at wavelengths longward of 3 μm, while its emission is rapidly decreasing towards shorter wavelengths due to the high extinction.

2. Reflection Nebulae: At shorter wavelengths (1-2 μm) our images are dominated by large, extended nebulosities, such as objects G and C. These objects quickly fade away

ID	H [mJy]	K [mJy]	L [mJy]	4.07 [mJy]	M [mJy]	N [mJy]	Note
A	1.4	4.7	7	4	4	–	
B	–	0.33	10	13	8	–	Reflection?
C	1.9	1.5	–	–	–	–	
D^a	0.113	14.8	530	1175	952	10520	UC H II
E	–	0.95	70	167	126	–	Red, elongated
F	0.12	2.4	34	8	47	–	
G	–	–	–	–	–	–	Reflection ?
H	–	–	12	37	29	–	
I	–	–	40	82	89	–	

Table 4.3: Summary of the observed fluxes and errors of objects in the vicinity of the UC H II G268.42-0.85. Only objects that are detected in more than one band are given; for the nomenclature, see Fig. 4.8. Due to the extended nebulosity the objects can not be distinguished in the J-band and therefore no fluxes in this band are provided here. At wavelengths longwards of the M-band only object D is visible. ^{a} – See Tab. 4.2.5 for the complete list of measurements.

with increasing wavelengths and show surface brightness gradients towards object D. We interpret them as reflection nebulae. The actual shape of these objects is defined both by the geometry of the scattering material and the extinction.
3. Other Sources: Objects A, B and F also appear in the L- and M-band images. These objects are most likely stellar objects with significant L- and M-band excess, suggesting recent or ongoing star formation close to the UC H II. The elongated, externally heated source E can either be a photoevaporating dust clump or an elephant trunk, similar in nature but much smaller in size than those seen in M16. Its stellar content is unknown. Object H can be interpreted as a warm dust cocoon, only visible at 3 and 5 μm. For a spherical, totally black dust particle at the projected distance from an O7 star we estimate an equilibrium temperature of at most 80 K. As the flux of Object H peaks in the 3–5 μm regime, we argue for an internal heating source, i.e. for an embedded star.

4.2.5 Spectral Energy Distribution of the UC H II Region

In this section we estimate the extinction towards the UC H II region from the N-band spectrum, summarize the available photometry and discuss the spectral energy distribution of the region.
The N-band spectrum shown in Fig. 4.9 displays a strong 9.7 μm silicate feature in absorption as well as the sharp forbidden emission lines of [ArIII] and [SIV]. The shape and the depth of the silicate absorption feature is characteristic to the absorbing foreground dust. We followed the simple approach described by Pascucci et al. (2004) to fit the feature by a

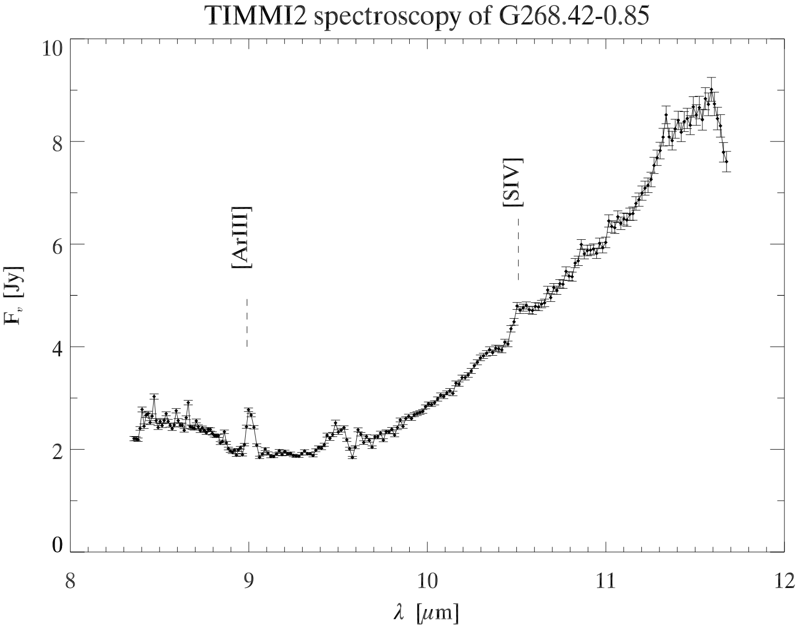

Figure 4.9: TIMMI2 N-band spectrum of the UC H II G268.42-0.85. The spectrum shows broad and deep silicate absorption feature with forbidden line emission from [ArIII] and [SIV].

synthetic absorption profile. This procedure results in a hydrogen column density (atomic and molecular) of $N_H = 3.7\times10^{22}$ cm^{-2}, which corresponds to a visual extinction of about $A_V \simeq 19.5$ mag using the Weingartner and Draine (2001) R=3.1 Milky Way extinction law. The estimated dust colour temperature is about $T_C \simeq 220 \pm 3$K.

In Table 4.2.5 we compiled the flux densities obtained both from our measurements and from the literature. The wavelengths, instruments and apertures as well as the corresponding references are indicated here.

Based on the observational data in Table 4.2.5, in Fig. 4.10 we show the spectral energy distribution of the UC H II. We included here the results of several satellite and balloon missions: The MSX satellite provided data at 8.3 μm, 12.1 μm, 14.7 μm, and 21.3 μm. The TIFR balloon experiment observed our source at 148 μm and 209 μm (Ghosh et al. 2000). The same authors also reexamined the IRAS HIRES 60 μm and 100 μm images, and we use their revised fluxes for these two data points. Furthermore, we included our ISAAC and TIMMI2 measurements between 1 – 13 μm and our new SIMBA 1.2 mm data point.

The SED follows well the main characteristics UC H II regions (see, e.g., Henning et al. 1990, Churchwell 1991): A steep rise of thermal dust emission in the mid- and far-infrared with a peak between 60 and 100 μm, and a decline of the millimetre dust emission with decreasing optical depth (100 - 3000 μm). Although in the case of IRAS 09002-4732 the millimetre regime is poorly sampled, the infrared part is quite well constrained.

Wavelength μm	Flux [Jy]	Error	Aperture Radius [$''$]	Instrument	SED Fit?	Note
1.6	1.1×10^{-4}	±12%	PSF-Fit	ISAAC SWI	No	[1]
2.2	1.5E-02	$^{+3.5}_{-2}$%	PSF-Fit	ISAAC SWI	No	[1]
3.78	0.53	$\simeq$ 8%	4.6	ISAAC LWI	No	[1]
4.09	1.175	$\simeq$ 11%	4.6	ISAAC LWI	No	[1,a]
4.66	0.95	$\simeq$ 8%	4.6	ISAAC LWI	No	[1,b]
11.9	10.52	$\simeq$ 10%	4.6	TIMMI2	No	[1]
12.9	10.7	$\simeq$ 10%	5.5	TIMMI2	No	[1]
Q	> 29.5	–	0.8	TIMMI2	No	[1,c]
8.28	30.74			MSX A	No	[2]
12	203	±9%		IRAS	No	[3]
12.13	103.3	±3%		MSX C	Yes	[2]
14.65	188.8	±4%		MSX D	Yes	[2]
21.34	1301	±6%		MSX E	Yes	[2]
25	2577	±4%		IRAS	No	[3]
60	13611	±8%		IRAS	Yes	[3]
100	14057	±8%		IRAS	Yes	[3]
148	9127	–	180	TIFR	Yes	[3]
209	4753	–	180	TIFR	Yes	[3]
1.2 mm	17.0	±20%	120	SEST	Yes	[1]
1.3 mm	6.0 Jy[6]	–		JCMT	No	[4]
3.5 cm	0.5 $\frac{Jy}{beam}$	±10%		ATCA	No	[5]

Table 4.4: Summary of the observed fluxes and errors of the UC H II G268.42-0.85. As the error of the NIR photometry, we give the statistical error of the PSF fit. The one but last column indicates if the given flux density was included in the SED fitting (see Sect. 4.2.5). Notes: [a] – Filter centered on Br α [b] – Narrow-band filter [c] – Flux standard star not detected, only lower limit can be given. References: [1] – This thesis; [2] – Egan et al. (1999); [3] – Ghosh et al. (2000); [4] – Reipurth et al. (1996); [5] – Walsh et al. (1998); [6] – the peak flux is given

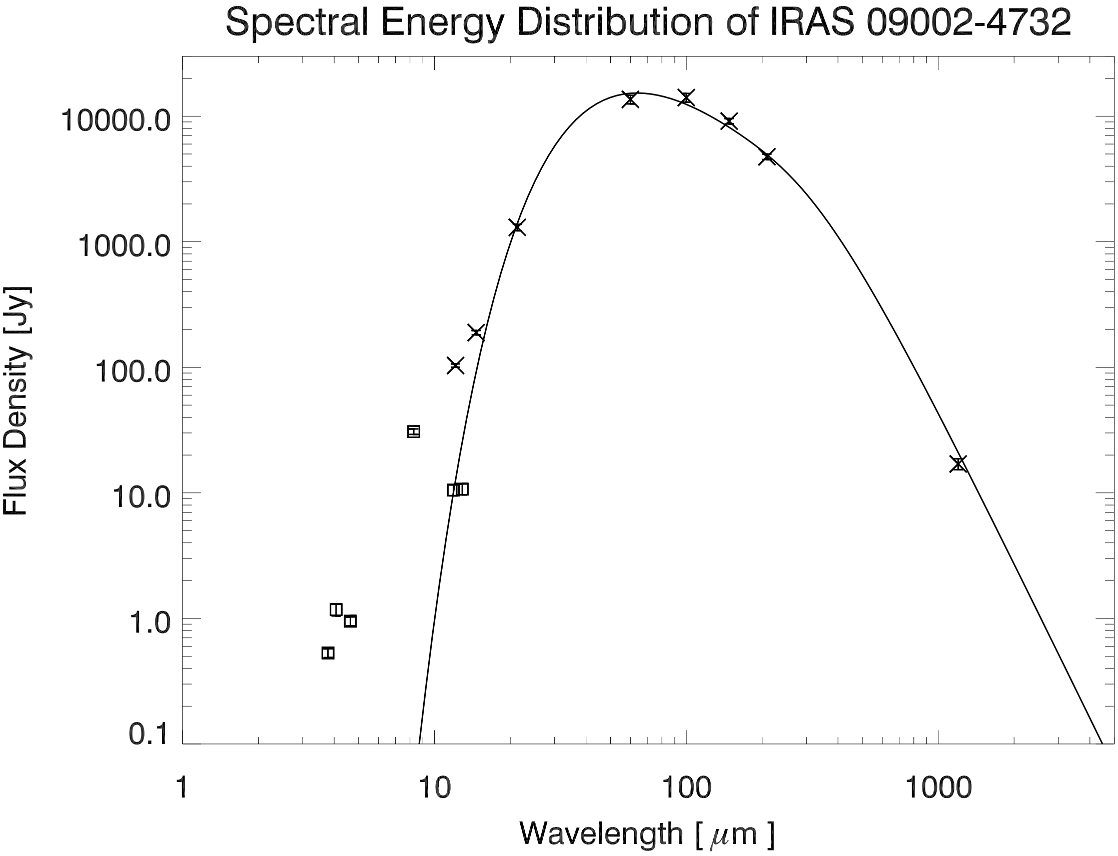

Figure 4.10: Spectral energy distribution of the G268.42-0.85 UC H II region. Crosses mark observations which were used for fitting the SED, squares denote data that are neglected in this regard (see Table 3.6). The curve is a modified black body with 0.014 pc radius, 80 K temperature and a dust emissivity of $\epsilon_\nu \sim \nu^{2.1\pm0.4}$. Error bars are included according to the values given in Table 4.2.5 but remain tiny due to the logarithmic scaling of the plot.

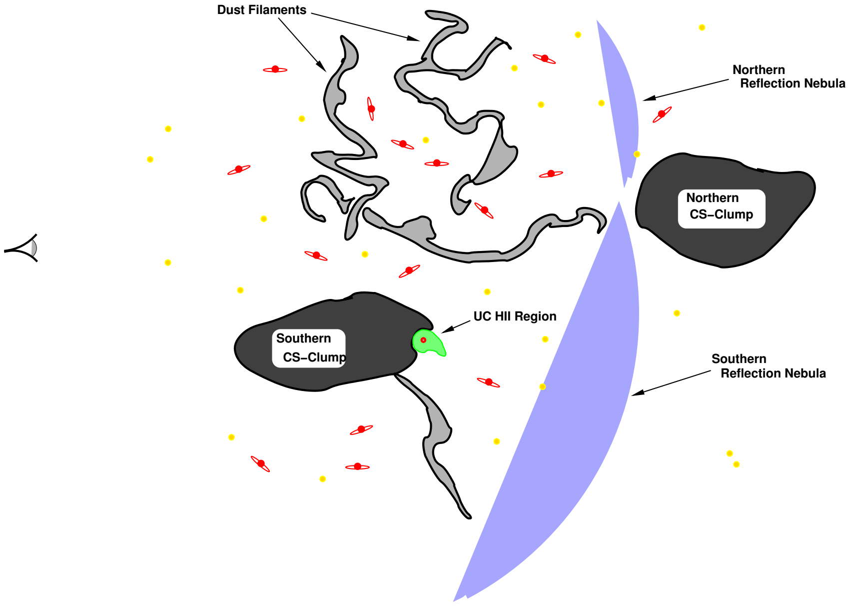

Figure 4.11: Simple sketch of the structure of the star-forming region IRAS 09002-4732. The likely relative line-of-sight positions are mainly deduced from the extinction pattern and different geometrical considerations as described in Sect. 4.3.1. The observer's direction is marked by an eye symbol.

Since the data plotted in Fig. 4.10 have been taken by different instruments with different beam sizes, some flux differences are inevitable. Observations with large beams - such as IRAS or TIFR - are not directly comparable to high-resolution data. A good example for this effect is the large difference around 10 μm in the high-resolution TIMMI2 and the coarser MSX-photometry. However, the fluxes at different beam sizes often include additional spatial information and are important for constraining radiative transfer models.

We fitted the data with a modified Planck curve with frequency-dependent dust emissivity as a free fitting parameter beside the temperature and two scaling factors.

Only data derived from large-beam measurements were used for the fit to assure a more or less homogenized sample (see column 6 of Table 4.2.5). This is also shown in Fig. 4.10, where crosses mark the data we have used for fitting and squares show data we have neglected. We mention that we have not used the MSX A-band data at 8.3 μm. This band is known to be affected by PAH emission. These aggregates are often susceptible to so-called quantum heating and do not necessarily attain an equilibrium temperature. As is evident in the plot, the 8.3 μm point shows clearly excess emission and is thus far above the expected level.

The best-fitting temperature is 80 ± 10 Kelvin. The power-law ansatz for the frequency behaviour of the dust emissivity resulted in $\epsilon_\nu \sim \nu^{2.1\pm0.4}$. Thus, the exponent is near to the canonical value of 2.0 for interstellar grains (e.g. Draine & Lee 1984). The estimated modified Planck curve fits the used data quite well. Obviously, the fit cannot account for the flux levels of the L and M band data (3-5 μm). There strong infrared excess emission was measured, which we interpret as a trace of hot circumstellar material very near to the central heating source.

The bolometric luminosity we infer from our SED fit is $\sim$8 $\times 10^4$ $L_\odot$ at an assumed distance of 1.3 kpc. The bolometric luminosity and the spectral type estimate will be discussed in Sect. 4.2.6.

A somewhat less well-defined SED has been modeled recently by Ghosh et al. (2000), using a self-consistent radiative transfer model that included the angular sizes at different wavelengths, radio continuum data as well as dust composition and grain size distribution. Their best fitting spherically symmetric model, assuming a distance of 1.4 kpc, predicts a single O7 ZAMS star as heating source, providing a bolometric luminosity of $10^5 L_\odot$ to the region.

4.2.6 The ionizing star of the UC H II Region

As shown in Figs. 4.1 and 4.4 the mid-infrared and the millimetre emission, as well as the reflection nebulosity peaks at the location of the UC H II region. Thus, the heating and illumination of the IRAS 09002-4732 star-forming region is dominated by the same single source or compact cluster which ionizes the UC H II G268.42-0.85 region. The fact, that no other locations of radio continuum emission were reported in the region supports the assumption that the most massive young star(s) in the region are located at G268.42-0.85. This UC H II region is one of the few cases where the NIR and MIR counterpart of the ionizing source can be clearly identified (source D in Sect. 4.2.4). Because this counterpart remains unresolved even at a spatial resolution of $\simeq$ 700 AU in the H and Ks filters, discriminating between a compact multiple system of massive stars and a single source requires interferometric or spectroscopic observations (see also Chapter 5). For the purposes of this work we assume that the ionizing source is a single massive star.

In the following we use the flux density of the free-free emission to derive lower limit for the ionizing star's luminosity. The number of Lyman continuum photons (N_e') necessary to maintain the ionization of the nebula is:

$$N_e' \geq 8.04 \times 10^{46}\; T_e^{-0.85}\; U^3,$$

where T_e is the electron temperature and U is the ionization parameter (see, e.g. Kurtz et al. 1994). Following their arguments the ionization parameter can be calculated as

$$U = r n_e^{2/3} = 4.553 \left[\frac{1}{a(\nu, T_e)} \left(\frac{\nu}{GHz}\right)^{0.1} \left(\frac{T_e}{K}\right)^{0.35} \left(\frac{S_\nu}{Jy}\right) \left(\frac{D}{\mathrm{kpc}}\right)^{2} \right]^{1/3},$$

where r is the radius, n_e is the rms electron density, ν is the frequency of the observations, T_e is the electron temperature, S_ν is the flux density and D is the distance. The term $a(\nu, Te)$ is tabulated by Mezger and Henderson (1967) with values close to 1. Corresponding to the 8.64 GHz frequency of the ATCA observations of Walsh et al. (1998), we adopted the value of 0.95.

Using standard AIPS routines, we estimated the total flux density to be 2.67 Jy at 8.64 GHz from the radio interferometric data of Walsh et al. (1998). With the assumptions of 8000 K electron temperature and a distance of 1.3 kpc we derived a Lyman-continuum flux of $N_e' = 5.0 \times 10^{47}$ s^{-1}.

Based on this estimate, the spectral type of the ionizing star has to be at least B0 (Panagia 1973; Schaerer and de Koter 1997). However, this estimate gives only a lower limit for the following three reasons: First, the interferometric observations are insensitive to the extended halo and thus underestimate the total flux. Second, a considerable fraction of the Lyman-continuum photons are absorbed by dust inside the UC H II (see, e.g., Sect. 4.2.4, Mezger et al. 1974, Feldt et al. 1998). Third, the interpretation of the radio fluxes in terms of spectral types of the exciting star(s) is not straightforward, it sensitively depends on the level of sophistication of the underlying stellar models. Recent investigations of O star models demonstrate that considerable shifts in the calibration of the effective stellar temperature can occur when accounting for the combined effects of line and wind blanketing (e.g. Martins et al. 2002). Thus, these models predict a lower number of Lyman continuum photons from the star than the earlier models.

Simpson and Rubin (1990) used a similar method to calculate the Lyman-continuum photons from the radio flux of Caswell and Haynes (1987) with an assumed distance of 1.5 kpc. The deduced value of $N_e' = 7.1 \times 10^{47}$ photons/s corresponds to a spectral type of at least O9.5 and is in good agreement with our previous estimate.

Lenzen (1991) fits the spectro-photometric intensity distribution with an O7 ZAMS star heating an optically thick dust cocoon assuming a distance of 1.8 kpc. Transforming this estimate to the distance of 1.3 kpc used in this work would predict a spectral type between O7 to O8. This is probably due to the fact that Lenzen (1991) based his estimate on the IRAS fluxes, which has been recently found to be overestimated (Ghosh et al. 2000).

Because the heating of the region is dominated by the ionizing source of the UC H II region, the bolometric luminosity of the star-forming region can also be used to assess the spectral type of this star. In Sect. 4.2.5 we found the bolometric luminosity derived from the SED to be $\sim 8 \times 10^4$ L$_\odot$ at the assumed distance of 1.3 kpc, consistent with the N_e' number of Lyman-continuum photons we have found from the radio continuum estimate. This bolometric luminosity thus argues again for a star of a spectral type not later than O9. If the central object was a compact cluster, than the O9 spectral type estimate would be valid for its most massive star because the most massive star always dominates the luminosity of such small clusters.

Thus, the radio continuum measurements, infrared and bolometric luminosity estimates give a coherent picture for the spectral type of the ionizing star as being O9 with an accuracy of 1 subclass.

4.3 Global Picture and Summary

4.3.1 Geometric Model – Completing the Puzzle

In this section, we summarize what we have learned about the individual components of the star-forming region and develop a coherent structural model. Fig. 4.11 illustrates the basic concept of this model.

Hundreds of stars has been identified in the region of IRAS 09002-4732. We find about 60 young pre-main sequence stars, an evidence for recent star-formation. The stellar densities increase towards the location of the UC H II G268.42-0.85. It is worthwhile to compare the stellar cluster with the positions and extensions of the two dense molecular clumps observed in CS by Lapinov et al. (1998) and shown in Fig. 4.2. While the north-western clump has no obvious effect on the stars, at the position of the south-eastern clump high reddening and extinction is present. This implies that the former clump is in the background of the cluster, while the latter is in front of it. Still, both of them should belong to the same complex since the CS maps show a loose connection between the foreground and background clumps. The presence of large masses of dust and dense molecular gas ($M > 600\ M_\odot$, Zinchenko et al. 1995) suggests that the star-formation process has not yet have time to fully disperse the natal molecular cloud and there is still material left for further star formation.

The UC H II region is detected close to the edge of the southern CS clump with all objects in its environment being very red. This suggests that the UC H II region is not in front of the clump. Furthermore, as shown in Sect. 4.2.2, the star ionizing the UC H II region is also causing the southern reflection nebulosity. This, in turn shows that (even the visible) light can to escape backwards from the UC H II region, thus its likely location is at the backside of the molecular clump or behind it. However, the fact that the morphology of the UC H II region is cometary and is compressed roughly towards the CS clump implies that it is no behind the southern CS clump but partly embedded in its rear wall. Furthermore, the tail of the cometary UC H II region points towards the brightest spot of the southern reflection nebula, suggesting that most of the light escapes in the same direction in which the hot gas expands – apparently away from the centre of the CS clump, towards decreasing density. The location and the morphology of the ionized gas suggests that the UC H II G268.42-0.85 is most likely a champagne flow type region (Wood and Churchwell 1989). It seems probable that the NIR-bright object G in Fig. 4.8 is the reflection of light that shines out from the CS clump through this opening.

Thus, the southern reflection nebulosity acts as a screen reflecting back the light of the most massive star, which is almost completely hidden behind a dense molecular clump.

The dark dust filaments must be in the foreground of the northern reflection nebula, in a position where no light from the massive star can illuminate their sides facing us. Apparently the southern reflection nebula has a lower number of such filaments – it is tempting to assume that this is due to the influence of the massive star.

The birth of the massive young star or compact cluster in G268.42-0.85 had a fundamental impact on the whole star-forming region, by re-arranging its illumination and temperature distribution.

4.3.2 Open Questions

Although the basic steps have been performed to understand this region, many more questions are still to be answered by future sensitive high-resolution observations. These are:
Are the filaments left-overs from the contraction of the dust cloud? If so, can this filamentary structure also be seen in the distribution of the young stellar sources? Are the globules in the filaments an early stage of protostellar objects? Does the UC H II region moves at supersonic speeds through the dust clump or do they have a common radial velocity? Are the elongated red objects around the massive star stellar objects with circumstellar material or externally heated and evaporating starless clumps? Is the most massive star single or multiple?

4.3.3 Conclusions

In this chapter, we provided the first global view on star formation around the IRAS point source 09002-4732. Our high-resolution, multi-wavelength (1-20 μm) data gave a detailed insight into the distribution and nature of the young stellar objects as well as into the morphology of the thermal dust emission. We described the large-scale morphology of the star-forming region, the associated young stellar cluster, and silhouettes of filaments and globular structures. We analyzed the most massive object and its surrounding, embedded in an UC H II. The most important conclusions of this chapter are the following:
— The luminous infrared source IRAS 09002-4732 marks recent star formation.
— We identified an embedded cluster of young PMS stars, exhibiting NIR excess. The stellar density shows an increase towards the UC H II.
— We unambiguously identified the star ionizing the UC H II region. Different methods are presented to assess the spectral type of this star, which we found to be consistent with being of ~O9.
— We showed that the heating and illumination of the star-forming region is dominated by the ionizing source of the UC H II region G268.42-0.85. This object is presumably the most massive young star in this star-forming region.
— We proposed the first structural model for the star-forming region. The UC H II G268.42-0.85 is located at the rear side of a dense molecular clump, consistent with the so-called champagne flow configuration. The massive star's light is reflected back from the southern reflection nebula.
— We identified numerous objects inside and in the direct vicinity of the UC H II region at sub-arcsecond resolution. We showed that some of these objects are reflections, some are young stellar objects with NIR excess, while in some cases the external heating by the ionizing star is dominant.
— In the foreground of the reflection nebula's southern lobe a number of dark, high-extinction globular filaments were identified.

The results presented in this chapter have also been submitted for publication in a less detailed form to the journal Astronomy & Astrophysics (Apai et al. 2004a), while the intermediate results have been presented in several conferences (e.g., Apai et al. 2002)
Although our high-resolution imaging proved the existence of a young stellar cluster around the UC H II region G268.42-0.85 and we identified the near-infrared counterpart of the ionizing source, deciding if this star itself is massive binary or even a compact multiple system was not possible. This is a natural limitation of the imaging techniques which prevents us from determining the intrinsic multiplicity rate of massive stars. This information is, however, very important for the verification of the different proposed massive star formation scenarios (see also Chapter 1). In the following chapter we will apply high-resolution near-infrared spectroscopic radial velocity measurements to search for such close, massive binaries among the new-born massive stars.

Chapter 5

Search for the Youngest Massive Binaries

The formation of massive stars is one of the major challenges of galactic astronomy (see also Chapter 1). The root of the problem is the enormous luminosity of these stars, which — when coupled with the accretion luminosity — can efficiently halt any spherically symmetric mass accretion as soon as the mass of the central object reaches ~10 $M_\odot$ (Yorke and Kruegel 1977; Wolfire and Cassinelli 1987). Inspired by the evidence of stars with masses even above ten times of this limit, several scenarios have been proposed to overcome the radiation pressure barrier following two primary concepts:
1, To *suppress the effective luminosity* substantial theoretical effort was put in anisotropical radiative transfer simulations (Yorke and Sonnhalter 2002). In these simulations the formation of a massive, short-lived disk focuses most of the stellar emission towards the rotational axis. This "flashlight effect" (Yorke and Bodenheimer 1999) allows mass transfer to the central regions through the massive disk. Such calculations are able of building up stars with masses of ~30 $M_\odot$ but are limited in grid resolution and assume that all material entering the innermost grid accretes onto a single central object (Yorke 2002).
2, The alternative way of overcoming the radiation pressure is to *reduce the effective dust opacity* (Wolfire and Cassinelli 1987). Simulations aiming to reduce the effective dust opacities through dust grain evolution in a rotating, collapsing protostellar clump found only slight impact on the net radiative forces (Yorke and Bodenheimer 1999). One simple possibility which might work is, however, to accrete optically thick "blobs" of material. A particularly interesting and widely supported model based on this idea is to build up massive stars by coalescence of lower-mass stars (Bonnell et al. 1998). Such stellar collisions can only take place in extremely dense clusters where sufficient circumstellar dust is present to enhance the effective collisional cross-sections of the stars.
Currently no direct evidence could be found to distinguish between the scenarios proposed by Yorke and Sonnhalter (2002) and Bonnell et al. (1998). When discussing the difficulty of observationally testing these scenarios, Bally (2002) points out the difference in the expected multiplicity ratio of the massive stars produced by the two different mechanisms. A high frequency of nearly-equal mass massive binaries should form in the clusters

where stellar collisions are occurring (Bonnell 2002). The massive disk accretion model can currently not produce binary or multiple stars (Yorke and Sonnhalter 2002) and is questionable if the "flashlight" effect could be maintained at all spatial scales when strong gravitational perturbations from a close binary system are present. As we will discuss in Sect. 5.1 optically visible, i.e. more evolved massive stars are frequently identified to be in close binary systems, which can originate from the formation process or can be the result of subsequent dynamic evolution of the dense clusters.

Identifying close, massive binaries as fossils of failed stellar mergers, i.e. proving that also new-born massive stars are often multiple, would provide strong support to the coalescence scenario while facing the massive disk accretion scenario with a difficult test. The goal of this chapter is to present the first multi-epoch radial velocity observations of young, embedded massive stars aiming to probe if their binarity rate is intrinsically high.

5.1 Multiplicity of Massive Stars

Massive stars, following the completion of the formation process become optically visible on timescales $\sim 10^6$ years. Many of the optically visible massive stars are found frequently in multiple systems, a perfect example for them being the nearby Trapezium cluster, where all four high-mass stars are in fact multiple systems themselves (Preibisch et al. 1999).

The close binaries ($a < 2$ AU) remain spatially unresolved with the current imaging techniques even for the Orion Nebula Cluster, the nearest site of massive star formation. Only such close systems, however, constrain the massive star formation scenarios (Zinnecker and Bate 2002). These short-period systems can only be explored via spectroscopic radial velocity (RV) measurements. Up to now, however, only few of these studies have been accomplished. In the following we briefly review the main results of the relevant spectroscopic radial velocity studies.

5.1.1 Massive Binaries in Clusters and OB-associations

The spectroscopic high-mass star catalogue of Gies (1987) pointed out first that binaries are 2 times more frequent among the OB-association stars than among field stars. This result is seen as evidence for the dynamical ejection of the massive field stars from their natal clusters and also underlines the fact that dynamical interactions change the intrinsic binary fraction in timescales of a few million years.

The spectroscopic radial velocity survey of the young open cluster NGC 6231 (García and Mermilliod 2001) yielded important results from this homogenous sample. This cluster, part of the 3–5 Myr old Scorpius OB1 association, contains 12 O9-type stars and the recent RV-survey identified a global binary frequency as high as 82% for the stars with spectral types earlier than B1.5V. It is interesting to note that all but one O-type binaries in NGC 6231 have orbital periods shorter than 10 days with a strong peak at the orbital period of 3 days.

5.1.2 Massive Binaries in Star-Forming Regions

In order to avoid the influence of cluster dynamics on the intrinsic binarity rate, the study of very young (<1 Myr) star-forming regions is necessary. Due to the observational difficulties outlined in the next section, only very few studies have been successful in identifying massive binaries in star-forming regions.

The massive members of the $\sim$ 1 Myr-old Orion Nebula Cluster have at least 1.5 companions per primary star on average, as shown by recent bispectrum speckle interferometry (Preibisch et al. 1999). Although, it is yet unclear, how well this binary rate represent the intrinsic binarity of these massive stars and if cluster dynamics already modified the structure of the Orion Nebula Cluster (see, e.g. Hillenbrand and Hartmann 1998; Bonnell and Davies 1998).

A good target for measuring the binarity rate for large number of massive stars in an identical environment is the massive stellar cluster R136 which ionizes the Large Magellanic Cloud starburst cluster 30 Doradus. This cluster shows three distinct peaks in its star formation history at 5 Myrs ago, 2.5 Myrs and <1.5 Myrs ago (Selman et al. 1999). The recent spectroscopic survey of (Bosch et al. 2001) presented reliable RVs for 55 stars and found a RV dispersion of $\sim$ 35 km/s. This dispersion is much larger than what is estimated from the cluster dynamics and the dispersion is probably entirely dominated by binary orbital motions. Numerical simulations show that the observations are consistent with the hypothesis that all stars in the cluster are binaries.

Although this work provides a strong argument for the intrinsically high binarity ratio, this cluster is not representative for the galactic massive star-forming environments due its violent starburst nature and the multiply-peaked star-formation history. Additionally, because of the multiply-peaked star formation process in this cluster, the dynamically formed binaries may contaminate the intrinsic binarity rate to an unknown extent.

5.1.3 The Observational Challenge

The studies described above proved that massive stars *after the formation process has ceased* have higher binarity rate than low-mass stars. However, to exclude the possibility of binary formation as a result of mass segregation and cluster dynamics, i.e. to find if the multiplicity is an intrinsic property of massive stars, the study of the youngest objects is necessary. As also demonstrated in the previous chapter, ultracompact H II regions provide excellent signposts of newly formed, still embedded massive stars.

However, a multiplicity study of so young stars has to face several serious observational difficulties: First, due to their very short lifetime the youngest massive stars are deeply embedded in their natal gas and dust cloud making them visible only in the infrared regime. As we showed in the previous chapter, such a massive extinction can complicate the study of the region to a large extent. Second, these stars have so few and weak spectral lines, that they are often used as spectroscopic flat field sources. Third, being rapid rotators their spectral lines are broad and occasionally blending.

The recent years, however, proved that their line system in the K-band spectrum, when

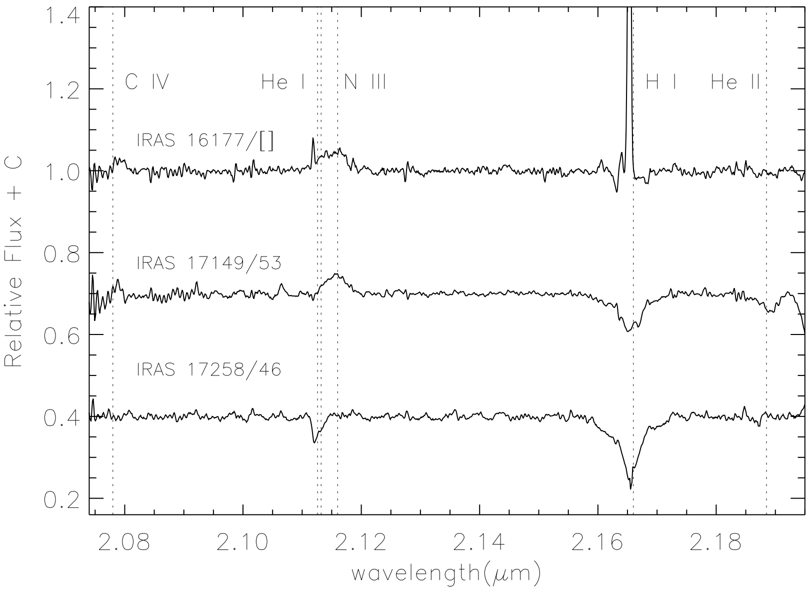

Figure 5.1: Relevant spectral lines of massive stars in the Ks-band spectra. Courtesy: A. Bik.

observed with high-enough signal-to-noise ratio and spectral resolution, can still provide reliable spectral type classification (Hanson et al. 1996). Table 6 of Hanson et al. (1996) gives an overview on the presence and strengths of different spectral lines as a function of the K-band spectral type. Example K-band spectra of three massive stars are shown in Fig. 5.1. The K-band spectral atlas has been applied by Bik et al. (2004) on 40 high-mass stars in or close to ultracompact H II regions using the ISAAC/VLT infrared instrument. This survey yielded a unique spectroscopic data set on the youngest observable massive stars.

Aiming to determine the massive stars' intrinsic multiplicity we obtained a second- and occasionally third-epoch spectra for 16 targets of Kaper et al. (2004) using an identical instrument setup. By identifying the variability of the massive stars' radial velocities we intended to probe the presence of close, massive companions.

5.2 Observations

5.2.1 Target Selection

In order to extend the existing spectroscopic survey of Bik et al. (2004) into a multi-epoch survey the most massive stars were repeatedly re-observed. The long slit of the ISAAC camera allows the simultaneous observations of typically two or three sources: the actual sources are selected by the combination of the field rotator and the telescope pointing. In

IRAS Source	Slit ID	1st Epoch	2nd Epoch	3rd Epoch	Comments
IRAS 10049-5657	Single	00/03/19	02 /06/19	2 × 02/06/20	
IRAS 15408-5356	Single	00/03/20	02 /06/19	02/06/20	
IRAS 16128-5109	Single	02/06/20	—	—	Late-type Star
IRAS 16177-5018	Slit 1	00/05/08	02/06/19	02/06/20	
IRAS 16177-5018	Slit 2	00/05/08	02/06/19	02/06/20	
IRAS 16571-4029	Single	00/05/08	02/06/20	—	
IRAS 17149-3916	Single	00/05/19	02/06/19	—	
IRAS 17175-3544	Single	00/05/19	02/06/20	—	Guiding failed
IRAS 17258-3637	Single	00/05/19	02/06/19	—	
IRAS 18507+0110	Slit 1	00/07/12	02/06/19	—	
IRAS 18507+0110	Slit 2	00/06/20	02/06/19	—	
IRAS 18060-2005	Slit 1	00/05/24	02/06/19	—	
IRAS 18060-2005	Slit 2	00/06/20	02/06/19	—	
IRAS 18006-2422	Single	00/05/24	02/06/20	—	Aborted; Too Bright
IRAS 18449-0158	Slit 1	00/06/20	02/06/19	02/06/20	

Table 5.1: Log of the observations and targets.

order to maximize the homogeneity of the data at different epochs we used the same slit positions for all but three objects. In these three cases only one massive star was covered in the original slit position: the new slit orientation allowed probing additional bright stars in the regions. The coordinates for our sources are presented in Kaper et al. (2004).

5.2.2 ISAAC Observations

The spectroscopic data presented in this chapter were obtained during several runs between March 2000 and June 2002 using the ISAAC detector (Moorwood 1997) mounted at the UT1 of VLT/ESO at Cerro Paranal, Chile. Table 5.1 summarizes the targets and date of observations.

The observations were carried out in a standardized fashion to ensure the homogeneity of the data set. For all objects the observed spectral range extends from 2.075 μm to 2.2 μm, centered on 2.134 μm with three exceptions: During the first epoch observations the objects IRAS 10049-5657 and IRAS 15408-5356 have been observed with a spectral range centered at 2.129 μm, while in the second epoch the object 10049-5657 has been observed additionally with a spectral range centered at 2.138 μm. In order to reach the highest spectral resolution we used the smallest available slit width with $0.3''$. The effective resolution with a resolving power of R $\simeq$ 10000 corresponds to a radial velocity resolution of $\simeq$30 km/s.

In order to free the spectra from the atmospheric influences after each science target we observed a telluric standard with identical airmass. As telluric standards we used A-type stars, which display no lines apart from the Brγ line in the spectral regime in question.

5.3 Data Reduction and Radial Velocity Determination

The data reduction was based on the IRAF/IDL toolbox developed by Arjan Bik. For the sake of completeness we describe here the principles of the original method and our improvements, but for an independent description, see also Bik et al. (2004).
As the first step, the filenames corresponding to the ESO Data Delivery standard (instrument and complete date and time, e.g. ISAAC.2002-06-20T22:53:38.357.fits) were renamed to the original, more informative internal ISAAC filenames (e.g., ISAAC_SWS_0047.fits). This made the operations on group of similar images easier. We used the script *orig_file.cl* for this purpose.

5.3.1 Basic Calibration Files

The second step was the preparation of the calibration data for each night. The dark frames for each integration times used during the observations were taken in daytime or acquired from the ESO archive. The frames with identical integration times were combined and bad pixel corrected using simple sigma-filtering process. As part of the standard procedure the final step was the removal of any electronic ghosts arising from detector cross-talks. We followed the procedure suggested in the ISAAC User's Manual.
We used high signal-to-noise spectroscopic flat fields taken with identical instrument setup to correct for the pixel-to-pixel variations of the instrument sensitivity. In order to avoid any interference pattern arising from minor changes of the light path inside the instrument (*fringing*), we obtained additional night-time spectroscopic flat field images several times during the observations. This allowed the use of the appropriate flat field for each object. The flat field images have also been ghost-filtered using the same algorithm as for the dark frames.
The next step was the derivation of a reliable wavelength calibration, i.e. a function assigning a wavelength to every pixel in x-direction and a two-dimensional transformation to correct for image distortion (e.g., the curved spectral lines are corrected to be straight and then the pixel x-coordinates are converted to wavelength units). This was done by reducing an arbitrary science object with the method described in details in Sect. 5.3.2. The resulting image has the dispersion axis along the x-direction (see, Fig. 5.2). The line system that dominates this frame is the emission from simple atmospheric molecular transitions, mostly of OH. The wavelengths of the OH-lines are very stable compared to our spectral resolution and therefore they are well suited for wavelength calibration. We used the central line of our images to first manually, then automatically identify the OH-lines from the comparison with the catalogue of Rousselot et al. (2000). The derived wavelength solution was typically better than 0.2 pixel. This wavelength solution was then step-by-step shifted and matched in the y-direction. This process thus mapped the

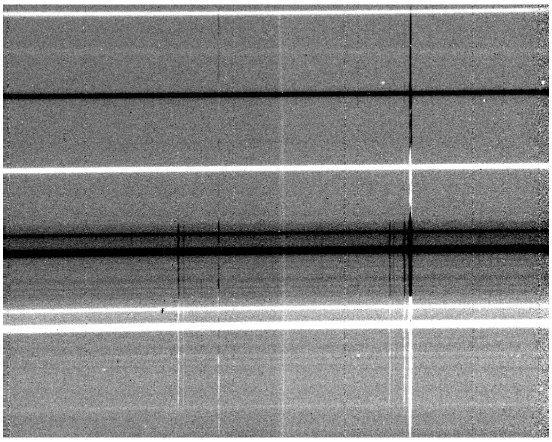

Figure 5.2: ISAAC Spectroscopic image after basic data reduction (dark and flat field correction, deghosting, edges chopped). The dispersion axis is parallel to the x-axis, while the long slit is lying in y-direction. The dominant line system here is that of the atmospheric (telluric) lines, arising mainly from OH transitions (see, e.g. Rousselot et al. 2000). Note, that due to image distortions the spectral lines are curved.

two-dimensional image to a one-dimensional wavelength axis. The IRAF tasks used for these purposes were *identify*, *reidentify* and *transform*. We derived independent wavelength calibration solutions for each night.

5.3.2 Basic Data Reduction

After the preparation of the basic calibration data described above, we processed the science data in the following manner: Ghost removal, dark current subtraction, chopping of the image edges, flat field correction, as discussed before. Following this, we made the difference of the two dithering positions, effectively removing the sky background continuum emission.

After these basic steps we used the appropriate wavelength solution to transform the image into a wavelength-calibrated and distortion-corrected image. All science frames and the telluric standard stars have been processed in an identical way. As the spectroscopic reduction process described here is widely used, our reduction script could be composed of standard IRAF NOAO spectroscopic tasks. The basic data reduction thus resulted in one image for each dithering position.

In a separate step we manually selected the spectra corresponding to the target objects in each dithering position of each science object or standard star. We extracted the spectra of the individual objects and combined all the spectra of the same object from different dithering positions using the IRAF tasks *doslit* and *scombine*.

5.3.3 Telluric Line Removal

As described in Sect. 5.3.1 we used the OH emission line system to wavelength calibrate our spectra. These emission lines in general cancel out nicely when subtracting different spectra taken at different dithering positions. However, an additional, complex absorption line system arising from several, partially identified molecular components is also imprinted in the observed infrared spectra. These telluric lines are difficult to remove, as their relative line fluxes change sensitively with the atmospheric conditions.

The telluric lines mean the biggest difficulty when measuring the spectra of the fainter science targets. In order to free the science spectra from the contaminating telluric lines, an accurate subtraction is necessary. Although the wavelengths of these lines are known, their relative intensities vary irregularly. To overcome this problem we observed an A spectral type star (telluric standard) immediately after each science target. A-type main sequence stars are featureless in this spectral regime except for the Brγ line. The airmass of the telluric standard was matching that of the science target as close as possible (typically better than 0.1). Our experience showed that having as small as possible airmass differences is necessary but not sufficient: telluric standards observed in the same direction as the science targets provided nearly perfect correction, while standards in very different directions often had different line intensities. The telluric line correction is a simple division of the science spectra by those of the telluric standards, however, one difficulty arises: Prior to the division, the single Brγ line in the A-type star spectrum has to be removed. As this line is very broad and deep, its imperfect removal badly affects the science spectrum. To worsen the problem, the line profile also varies somewhat from star to star, therefore no stellar templates can be reliably used.

Due to the varying Brγ profile of the A-stars it was necessary to fit the line in each individual spectra by an analytic expression. We tried to use different line profiles (e.g., Voigt-profile), but found that the best fit can be achieved by the sum of two Gaussian functions. We used the IDL task *amoeba* to optimize the multi-parameter fit. This task is based on the identically named optimization algorithm in the book Numerical Recepies in C: The Art of Programming. To help the Brγ line fitting procedure, a first-order telluric correction was carried out using the the high-resolution telluric spectrum provided by the National Solar Observatory/Kitt Peak Observatories. This correction freed enough the wings of the observed Brγ line from two strong telluric feature to be well fitted by the sum of the two Gaussians.

By subtracting the two-component Gaussians we found that in general this procedure efficiently removes the line leaving residuals typically less than 1% of the peak intensity. We then divided the science spectra with the corresponding Brγ-free telluric spectra and thus canceled the atmospheric lines. This step has been performed using the *telluric* task of IRAF, which aligns and scales the telluric template to the science spectrum.

After the telluric removal we rebinned our oversampled spectra by 3 pixels to remove the high-frequency noise and to approach the nominal resolution of the spectrograph. As a last step a simple continuum normalization took place using standard IRAF routines.

5.3.4 Radial Velocity Measurements

The telluric correction, rebinning and normalization provided us with the final spectra of the science targets. The final step of the procedure is the measurement of the radial velocities of each object at each epoch of the observations. As our science goal is the detection of close binaries, we were focusing on deriving relative radial velocities and did not aim to derive the absolute values. We chose always the first epoch observation (see Tab. 5.1) as the radial velocity zero point and compared the subsequent epoch(s) to this reference value. The comparison was done by using the IRAF package *RV* and the *fxcor* task.

The task *fxcor* is a package widely applied for accurately measuring the radial velocities by means of cross-correlation. As the package have been discussed by Fitzpatrick (1994) and Rodes et al. (1998), we only summarize here a few essential points and non-standard choices of parameters.

The radial velocity is determined by cross-correlating the first epoch measurement to the later epoch ones. However, as only the photospheric lines of the the massive stars carry valuable information on the radial velocity, not the full spectral ranges are compared. We only used the short spectral regions centered on given lines and excluded the very weak lines or continuum, which are often contaminated by the telluric residuals. The individual spectral regions of interest have been selected manually after the inspection of each reduced spectra. In Sect. 5.4 we analyse the effects of these choices on the accuracy of the radial velocity measurements.

The actual radial velocity difference, i.e. the wavelength shift between the two spectra are derived from the cross-correlation function: Its maximum is where the shifted second epoch spectra matches best the first epoch one. Finding the maximum of this the correlation function was done by fitting a Gaussian function on the peak. To adopt our measurement to the rather broad lines of the massive stars we enlarged the default short fitting interval into a maximum of 100 pixel interval. Fig. 5.3 shows an example for the radial velocity determination and the fitting of the cross-correlation function.

When interpreting the wavelength shift between the different epoch spectra as radial velocity shifts, one additional step has to be taken, namely the heliocentric correction. As the orbital velocity of Earth is known to great accuracy, we accepted the automatic heliocentric correction of IRAF (but see also Ref. 5.4.4 for the confirmation of the procedure).

5.3.5 Individual Objects

In the following we list the comments on the individual objects:

IRAS 10049-5657: Star #324 is identified as O7-O8 spectral type (see Fig 5.4). The telluric line removal was efficient but the Brγ line is over-subtracted due to overlapping nebular emission from the other dithering position. As its peak was unreliable, we included only the wings of the Brγ line in our cross-correlation.

Star #411 is of earlier spectral type (O5–O6) and has weaker spectral lines (see Fig 5.5). Although the telluric subtraction is in general good, the Brγ line is contaminated by some

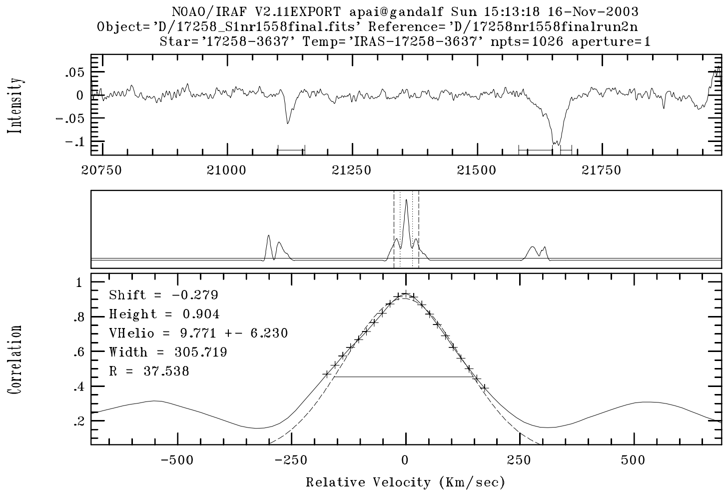

Figure 5.3: Example for the cross-correlation based relative radial velocity determination. The upper panel shows the object spectrum and the horizontal bars mark the wavelength range which was used for the cross-correlation. The middle panel shows the complete cross-correlation function, while the lower one displays a magnified region around the peak. The dashed curve is the fitted Gaussian and the horizontal solid line is its full width at half maximum. This plot is the output of the IRAF script *fxcor*.

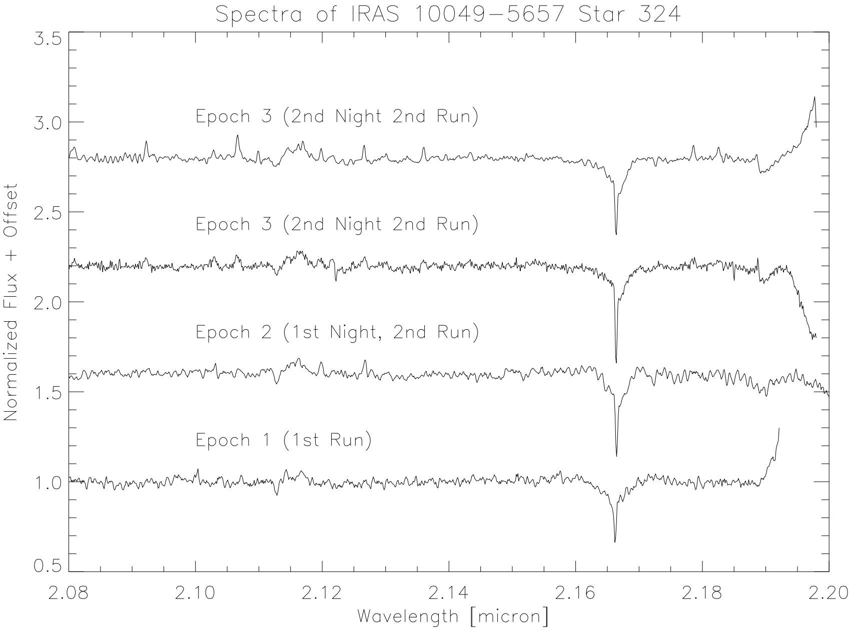

Figure 5.4: ISAAC Ks spectra taken at different epochs for the star #324 in IRAS 10049-5657.

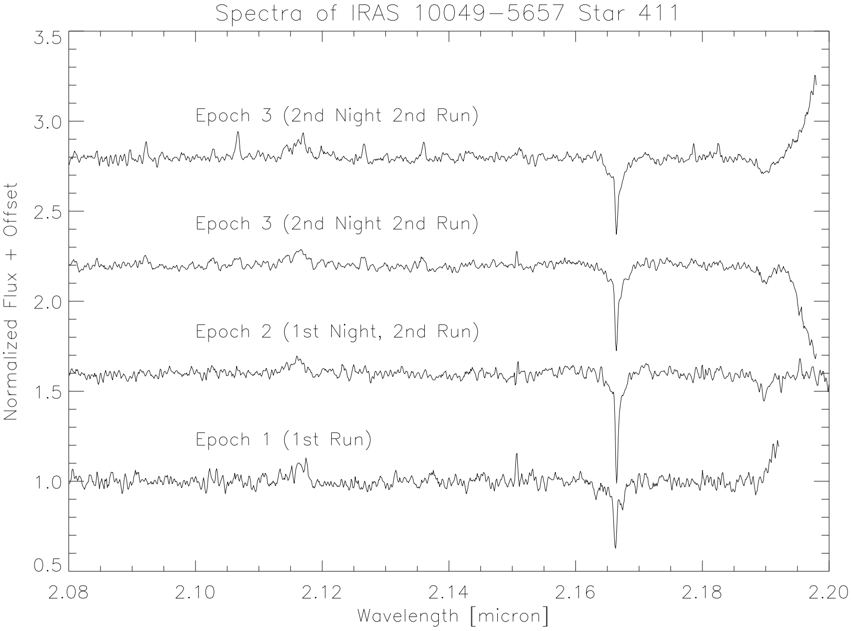

Figure 5.5: ISAAC Ks spectra taken at different epochs for the star #411 in IRAS 10049-5657.

telluric residuals and suffers nebular line over-subtraction. The NIII line is broad and not well-defined. However, cross-correlations of the Brγ wings and the NIII line gives very similar results to that from the correlation of only the NIII line, proving the reliability of the fit. The third epoch measurement gives a relative shift as large as ~88 km/s.

IRAS 15408-5356: Star # 1410 is also an early type star with an estimated spectral type of O5–O6 (see Fig 5.6). Although some fringing and telluric lines are present, the cross-correlation function has a sharp maximum.

Star # 1454 is an O9–B1 spectral type star with the HeI line in absorption (see Fig 5.7). The telluric subtraction is good, but the Brγ line has some nebular line over-subtraction. We used the HeI line and the wings of the Brγ line in the cross-correlation.

IRAS 16128-5109: The spectral classification showed that the objects in this slit positions are late-type stars and were therefore excluded from further discussion.

IRAS 16177-5018: Star # 271 has a spectral type of B2–B3 with weak HeI and Brγ absorption (see Fig 5.8). The wings of the Brγ line are useful for the cross-correlation. The 2nd epoch observations is of somewhat worse quality than the 3rd epoch.

Star #405 is an early-type star with O5–O6 classification (see Fig 5.9). The lack of absorption lines and the weakness of the emission lines makes the radial velocity measurement difficult.

Another very early-type star is # 1020, which classifies as of O5–O6 spectral type (see Fig 5.10). The Brγ line in its spectrum is dominated and filled by nebular line emission and was completely excluded from the fit.

IRAS 16571-4029: Star # 820 is of spectral type O9–B1 (see Fig 5.11). Although the

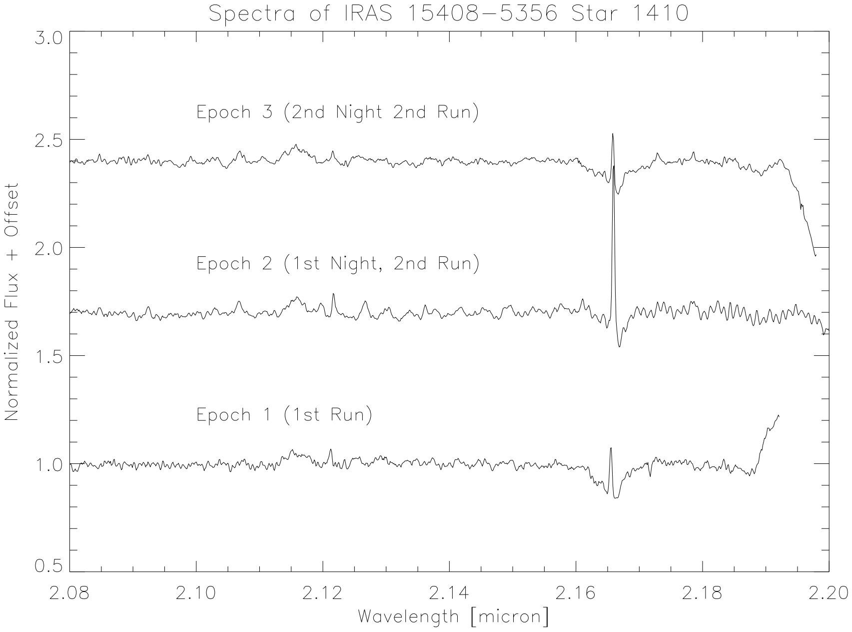

Figure 5.6: ISAAC Ks spectra taken at different epochs for the star #1410 in IRAS 15408-5356.

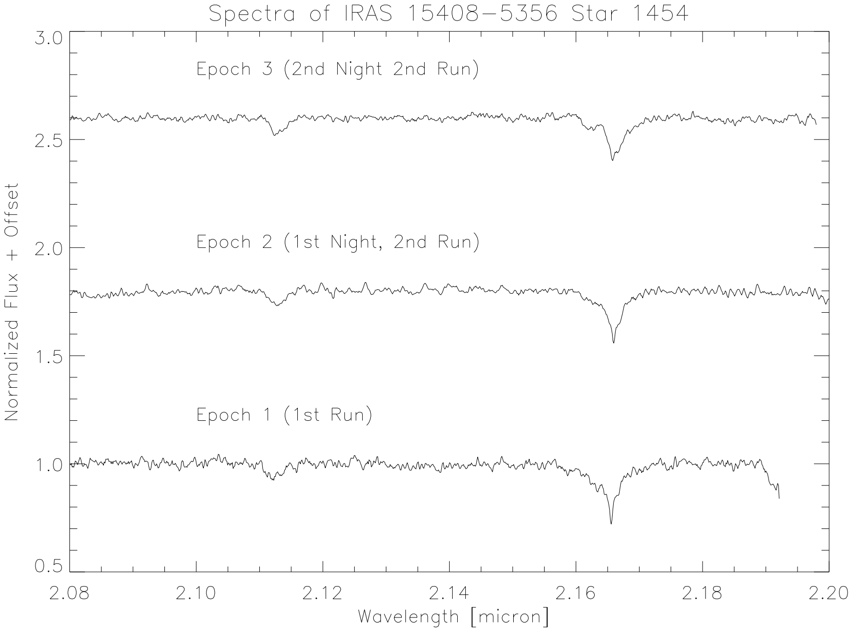

Figure 5.7: ISAAC Ks spectra taken at different epochs for the star # 1454 in IRAS 15408-5356.

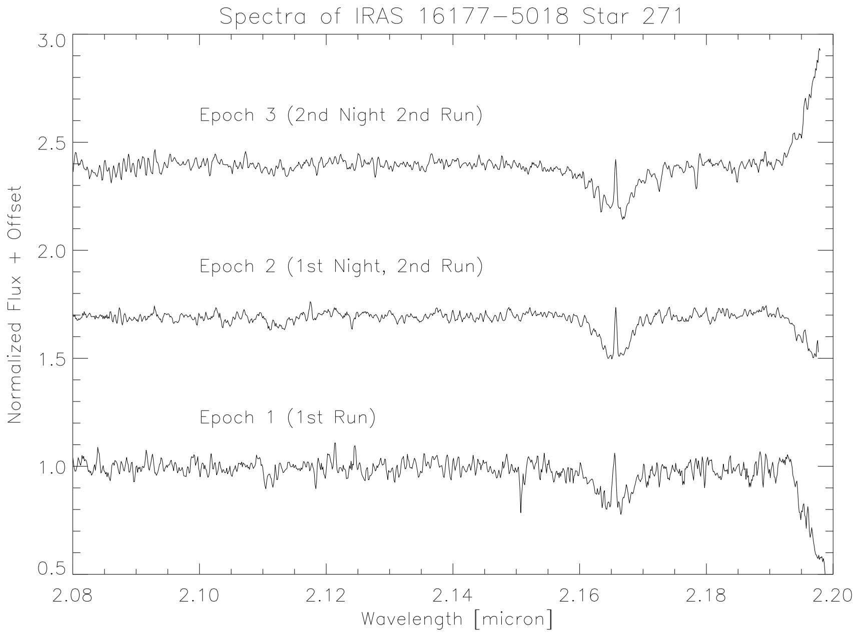

Figure 5.8: ISAAC Ks spectra taken at different epochs for the star # 271 in IRAS 16177-5018.

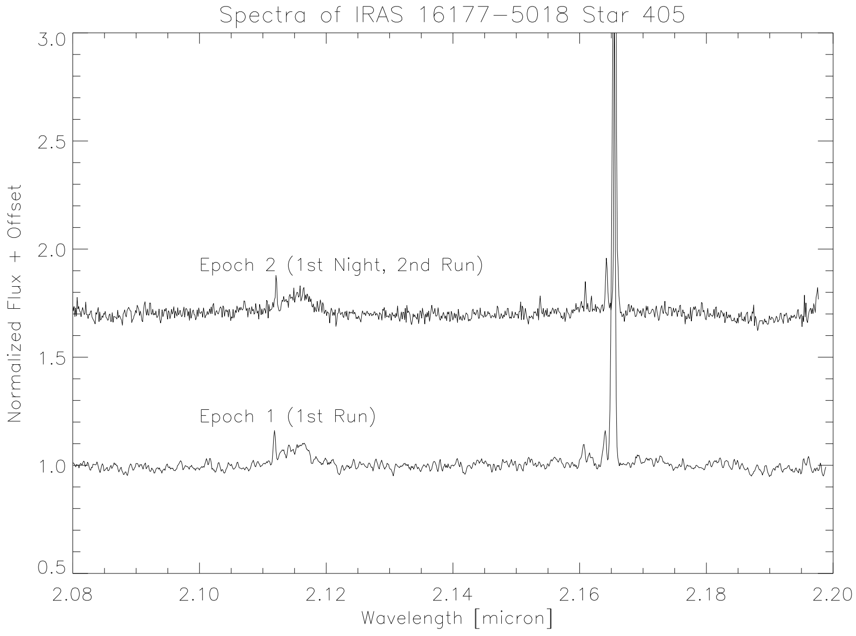

Figure 5.9: ISAAC Ks spectra taken at different epochs for the star # 405 in IRAS 16177-5018.

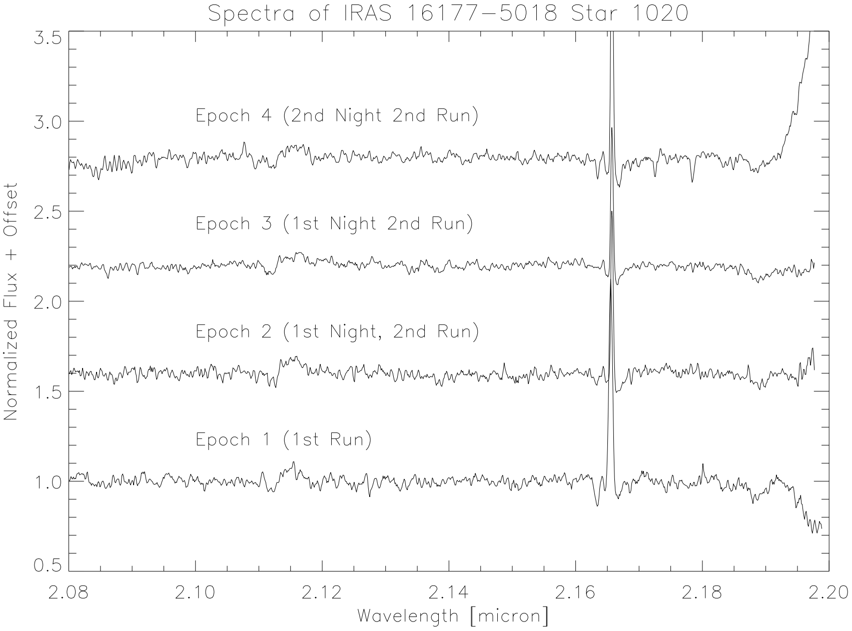

Figure 5.10: ISAAC Ks spectra taken at different epochs for the star # 1020 in IRAS 16177-5018.

spectra suffer from stronger-than-average telluric line residuals, the Brγ and the HeI lines are mostly free. The double-peaked [HeI] line provides firm basis for the cross-correlation.

IRAS 17149-3916: Star # 895 has been classified as of O5–O6 spectral type (see Fig 5.12). The CIV, NIII and the Brγ lines are present.
IRAS 17258-3637: Object # 1558 is an O9–B1 spectral type star (see Fig 5.13). The spectra suffer from telluric residuals; in the second epoch Brγ is contaminated by nebular emission.
Star # 378 is classified as O9–B1 spectral type (see Fig 5.14). Although the telluric line removal is not good, the atmospheric lines are free from residuals. The spectra from the two epochs are obviously shifted, while the telluric lines coincide. This seems to be a strong candidate for being a binary star.
IRAS 18006-2422: Star # 770 is an O9–B1 type star (see Fig 5.15). The spectra are of good quality apart from some telluric residuals.
IRAS 18449-0158: Star # 319 is an earlier type with an O5–O6 classification (see Fig 5.16). The Brγ line has a strange shape, might be affected by telluric residuals. Still, the broad NIII and HeI lines give strong basis for the fit. In the third epoch spectrum the Brγ line looks normal, but the overall telluric residuals are slightly worse.
IRAS 18507+0110: The spectra of star # 262 shows some fringes, but the telluric removal was successful (see Fig 5.17). The spectral classification of this star is O5–O6, and it is likely not a main sequence star but possibly a supergiant.
The star # 373 has been observed two times with two different slit orientations the night

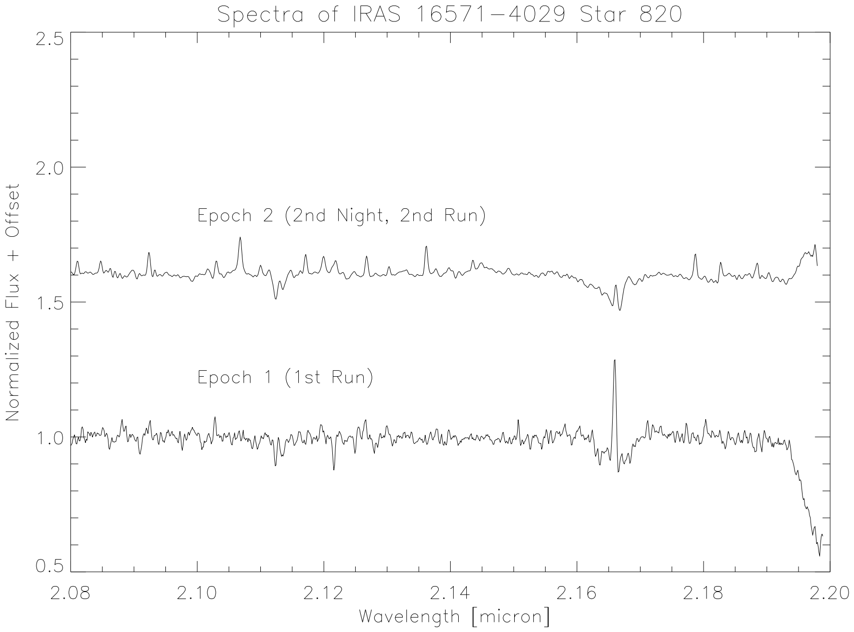

Figure 5.11: ISAAC Ks spectra taken at different epochs for the star # 820 in IRAS 16571-4029.

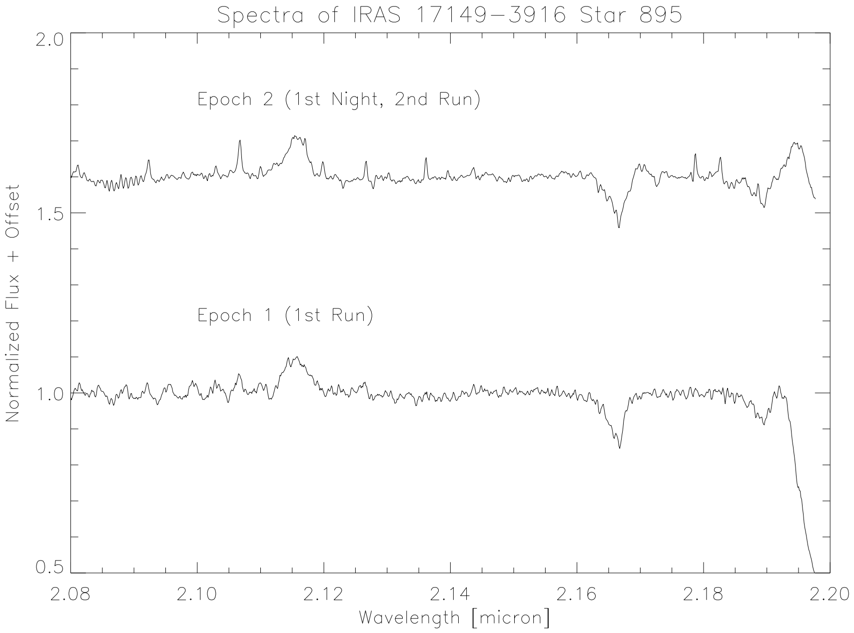

Figure 5.12: ISAAC Ks spectra taken at different epochs for the star # 895 in IRAS 17149-3916.

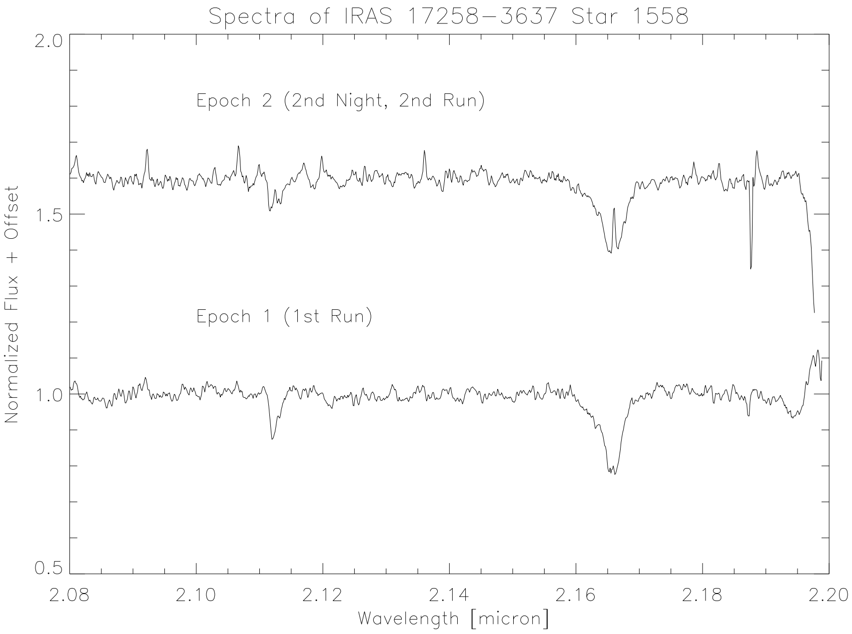

Figure 5.13: ISAAC Ks spectra taken at different epochs for the star # 1558 in IRAS 17258-3637.

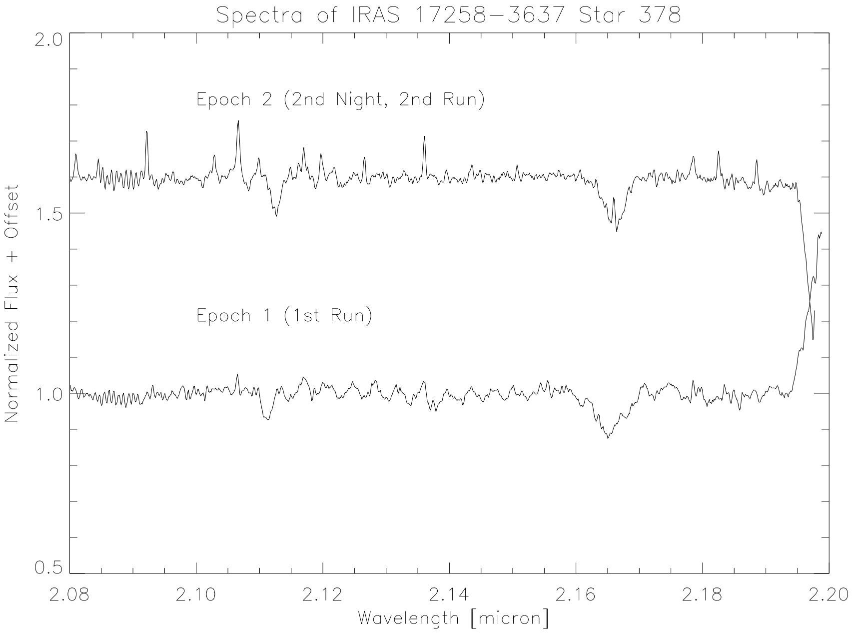

Figure 5.14: ISAAC Ks spectra taken at different epochs for the star # 378 in IRAS 17258-3637.

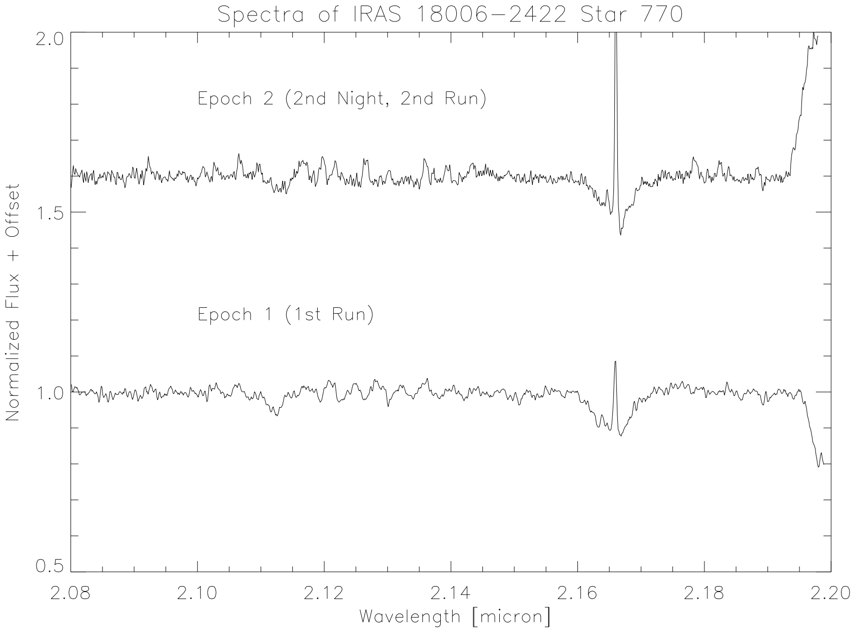

Figure 5.15: ISAAC Ks spectra taken at different epochs for the star # 770 in IRAS 18006-2422.

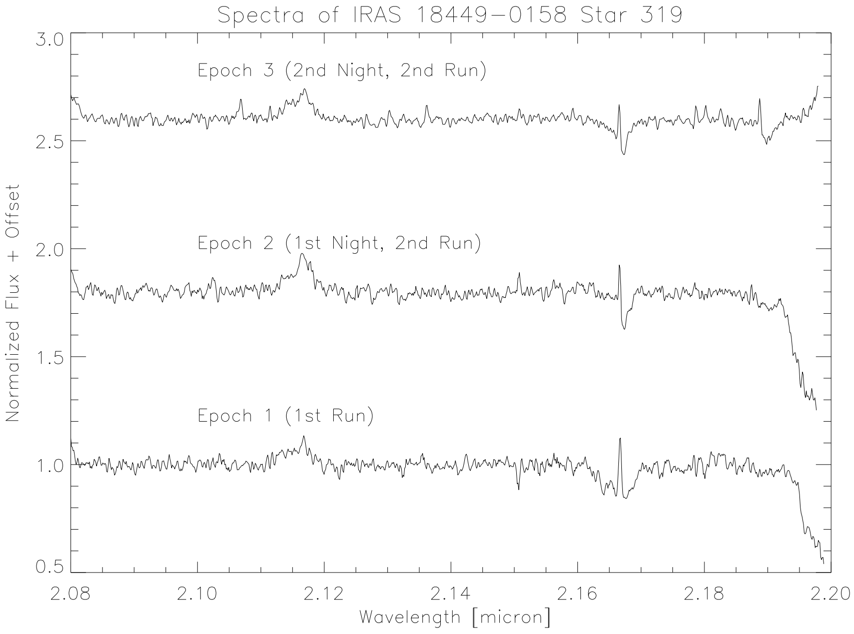

Figure 5.16: ISAAC Ks spectra taken at different epochs for the star # 319 in IRAS 18449-0158.

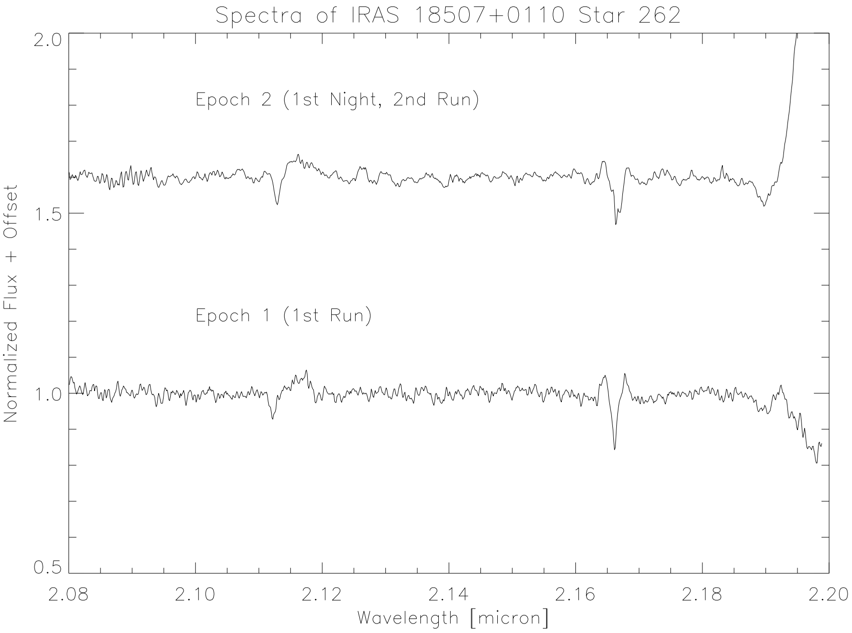

Figure 5.17: ISAAC Ks spectra taken at different epochs for the star # 262 in IRAS 18507+0110.

of 19th June 2002 (see Fig 5.18). This B2–B3 spectral type star provides a relatively weak cross-correlation peak due to the improper telluric line removal.
The second slit orientation on this IRAS source included the B2–B3 spectral type massive star # 389 (see Fig 5.19). Its spectrum shows characteristic HeI absorption lines, which give a firm basis for multi-epoch cross-correlation.

5.4 Error Analysis

The observations described in this chapter represent a pilot effort to derive radial velocity variations for embedded massive stars. These measurements are complicated by extinction, weakness of the lines and the telluric residuals, as explained in Sect. 5.1.3.
In such a complicated case a detailed error analysis is essential for the correct interpretation of the measurements. In the following we discuss the impact of the individual error sources and measure the total error from quasi-simultaneous observations. These error estimates will be used in the Section 5.5 where the observational results will be interpreted.

5.4.1 Peak Fitting Methods and their Errors

The relative radial velocity ΔRV is determined by finding the maximum of cross-correlation function of the spectra from different epochs (see also Sect. 5.3.4). Localizing the maximum is accomplished by fitting the peak of the cross-correlation function. We tested different

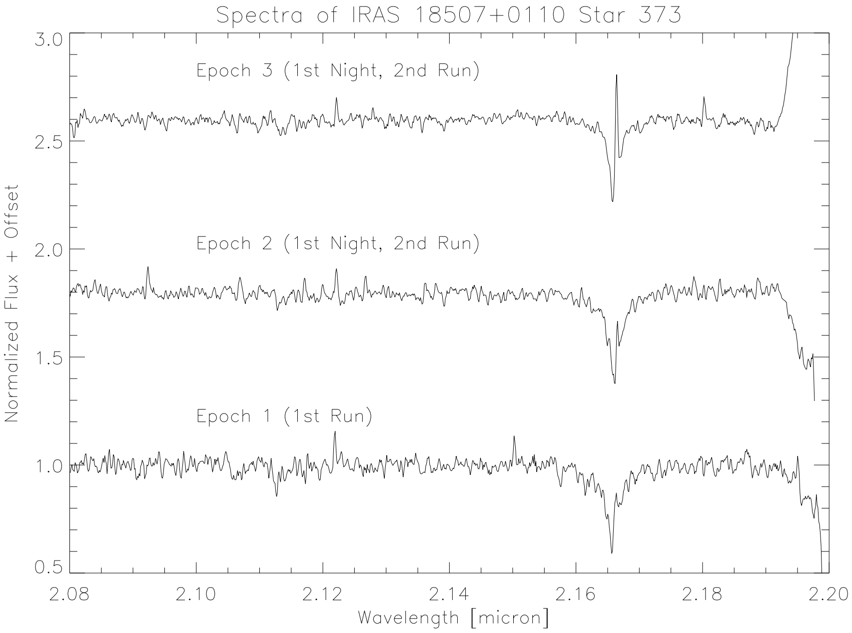

Figure 5.18: ISAAC Ks spectra taken at different epochs for the star # 373 in IRAS 18507+0110.

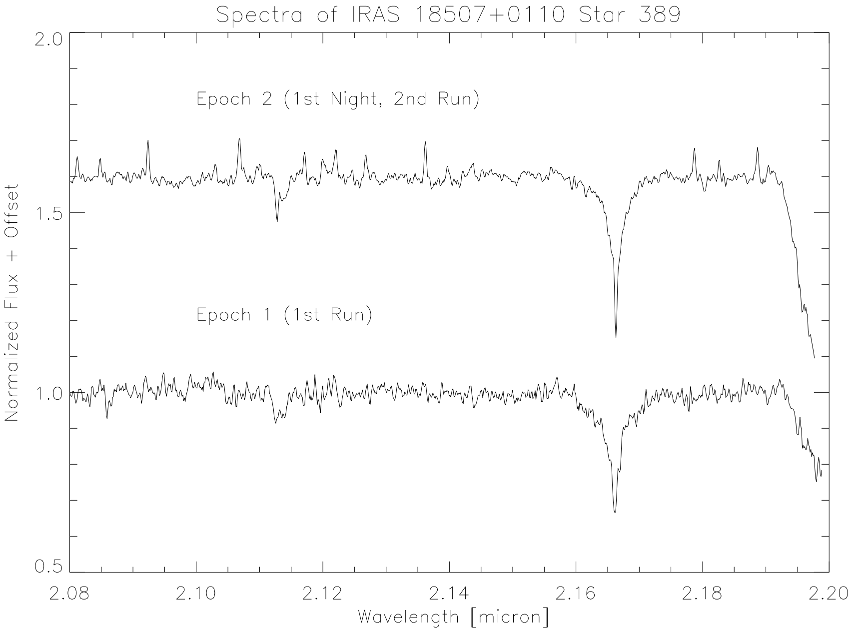

Figure 5.19: ISAAC Ks spectra taken at different epochs for the star # 389 in IRAS 18507+0110.

peak-fitting methods including Gaussian-fits, the IRAF's Center1D routine, parabola-fits and Lorentzian-fits. All algorithms but the Center1D provide formal error estimates for the fit results as the full width at half maximum of the fitted curves.

In general, we found that the Gaussian, Center1D and Lorentzian methods gave statistically very similar results: the absolute mean ΔRV was always lower than 1.5km/s and its standard deviation was between 34.5 and 37.5 km/s. The results on the individual objects were also consistent. Although the parabolic approximation gave as well similar results for most of the objects, in some cases it provided an unstable, out-of-bounds solution.

Throughout the paper we used the Gaussian fitting, as this provided the most robust results. The regime of the fitting has been enlarged to 70 pixels corresponding to about 1200 km/s velocity difference to take also the wings of the cross-correlation peak into account.

5.4.2 Telluric Line Residuals

The relative radial velocity ΔRV measurements are based on the cross-correlation of spectra taken at different epochs. All spectra bear to some extent the imprint of the atmosphere in the form of fixed-wavelengths telluric lines. The influence of these residual lines on the cross-correlation was one of our major concerns; although the individual line residuals have low fluxes, their integrated power could bias the ΔRV measurements towards the zero values.

In order to test this possibility, we repeated the radial velocity measurements but used a photospheric-line-free, pure continuum spectral region between 2.125 – 2.1500 μm for the cross-correlation. This region is dominated by the telluric line residuals. In contrast to the expected closely zero ΔRV values the cross-correlation returns randomly distributed values between $\sim$ 1100 and -1100 km/s.

Therefore we conclude that the telluric line residuals do not introduce any systematic high-power signal to the cross-correlation function.

5.4.3 Wavelength Calibration

As described in Sect. 5.3.1 we derived an individual wavelength calibration for each night of the observations. The error of the wavelength solution is well characterized by the comparison to the OH-line catalogue containing thousands of narrow spectral lines. The wavelength calibration was typically better than 0.2 pixel, corresponding to a RV inaccuracy of 3.4 km/s for unresolved lines.

5.4.4 Heliocentric Corrections

The observed radial velocity of each target includes a significant contribution from the orbital motion of the Earth. This component, which can be as high as $\sim$28 km/s can be accurately calculated from the time of the observations and the celestial coordinates of the targets. The IRAF package contains this calculation, which is part of the radial velocity determination. As Earth's orbital solution, the date and the target coordinates are known to a high accuracy we assume that no significant error can come from the heliocentric radial velocity corrections. In order to ensure that the process itself is used correctly, we applied manually the heliocentric correction on one object and confirmed the automatic correction.

5.4.5 Quasi-Simultaneous Observations

In the case of four objects subsequent spectra were obtained in two slit positions. The typical time difference is about 1 hour. Assuming that the RVs did not change significantly between the two observations, the comparison of these quasi-simultaneous observations gives a good basis for estimating the total error.

Using these observation pairs we tested the consistency of the different RV determination methods. As shown in Table 5.2 we compared the observations from a given night in the second run directly by fitting a Gaussian in the peak of their cross-correlation function. As throughout the paper we use the first epoch observations as the RV reference for all objects, we also compared the second and third epoch observations by cross-correlating them with the reference first epoch spectra. In the indirect method we again tested different peak-fitting functions.

In the ideal case all measured RV differences should be zero. The higher values seen here arise from two effects: the error of the RV determination and the assumption that these stars are not very close massive binaries. In the case if our assumption is true for all four objects, the observed differences are characteristic to the measurement error; otherwise they represent upper limits for the measurement accuracy.

The mean of the absolute values of the differences is 19.0 km/s, 24.2 km/s, 29 km/s and 25.6 km/s for the direct Gaussian, indirect Gaussian, indirect Center1D and the indirect Lorentz comparison, respectively. The direct method has the smallest error, while among the indirect comparisons the Gaussian method is the most accurate and robust. By understanding the differences between the direct and indirect methods we can estimate the error contribution from the different methodical steps: The direct comparison of two quasi-simultaneous spectra contains the statistical errors on 2 measurements and the error of 1 cross-correlation and peak fitting. The indirect Gaussian method is carrying the errors from 3 measurements, 1 calibration difference and 2 correlations.

Our results as presented in Sect. 5.5 use the first epoch spectra as reference for the later observations and therefore contains the errors from 2 measurements, 1 calibration difference and 2 correlations. Their total error is between the errors of the quasi-simultaneous direct and indirect Gaussian methods described above. Thus, the total error on our RV-difference measurements is between 19.0 km/s and 24.2 km/s, somewhat higher than the 14.7 km/s mean of the formal error estimates of the IRAF routine fxcor.

Obs. Pair ID	Direct Gaussian [km/s]	Gaussian [km/s]	Center 1D [km/s]	Lorentz [km/s]
dRV1-dRV2	−18.0	−18.0	−11.2	−15.7
dRV4-dRV5	−4.6	39.9	56.9	40.0
dRV12-dRV13	15.2	3.8	−18.8	−7.1
dRV25-dRV26	38.1	35.1	—[a]	39.4
Mean of Abs. Diff.	19.0	24.2	29.0	25.6

[a] — The Center1D function did not converge in this case.

Table 5.2: Radial Velocity differences of the four quasi-simultaneous observations as measured by different methods. The first column is the identification of the observations as given in Table 5.1, the second column gives the RV difference derived from fitting a Gaussian function on the peak of the cross-correlation function of the two spectra. The other columns are the RV differences obtained by first correlating each second and third epoch spectra to the first epoch one and making the difference of the RV shifts. The last three columns differ in the function used for finding the peak of the cross-correlation function.

5.5 Results and Discussion

5.5.1 Observational Results

The primary result of our RV-campaign is the list of the RV changes between the different epoch observations for embedded massive stars. In Table 5.3 we show the IRAS sources, the ID of the observed stars, the estimated spectral types, the epochs, the RV differences and the error estimates.

The distribution of the RV-differences is plotted in the histograms in Figs. 5.20. The mean value of the 27-point sample is ∼0 km/s. We estimate the average RV-difference error to be between 19 and 24 km/s (see Sect. 5.4.5).

The stars # 378 in IRAS 17258-3637 and # 411 in IRAS 10049-5657 display RV-changes as large as ∼90 km/s between the different epoch measurements, a proof that these star are close massive binaries.

Our observations of these two stars are too sparsely sampled to provide estimates for the orbital parameters but already hint towards close and massive binaries: Considering the case of star #378, we assume a binary system of 15 $M_\odot$ and $9.5_\odot$ on a circular orbit, with the inclination of 70°. Using the Kepler III law we obtain that in order to reproduce the observed ∼100 km/s radial velocity variations the separation of the two bodies have to be less than ∼0.6 AU, i.e. a close and massive binary. Should the mass of the secondary body be less than the assumed value, then even smaller separation would be needed. A highly excentric orbit produces large radial velocity changes; however, the probability of measuring the system in the epoch close to the pericenter is also much lower. Similar

ID	IRAS Source	Star #	Sp. Type ID	Meas. ID	Night	Δ RV [km/s]	Error [km/s]
dRV1	IRAS 10049-5657	324	O7/O8	1	2	14	11
dRV2	IRAS 10049-5657	324	O7/O8	2	2	32	12
dRV3	IRAS 10049-5657	324	O7/O8	3	1	15	14
dRV4	IRAS 10049-5657	411	O5/O6	1	2	27	14
dRV5	IRAS 10049-5657	411	O5/O6	2	2	-13	29
dRV6	IRAS 10049-5657	411	O5/O6	3	1	87	5
dRV7	IRAS 15408-5356	1410	O5/O6	1	1	13	20
dRV8	IRAS 15408-5356	1410	O5/O6	2	2	27	17
dRV9	IRAS 15408-5356	1454	O9/B1	3	1	21	14
dRV10	IRAS 15408-5356	1454	O9/B1	3	2	18	25
dRV11	IRAS 16177-5018	1020	O5/O6	1	2	-13	9
dRV12	IRAS 16177-5018	1020	O5/O6	2	1	-19	14
dRV13	IRAS 16177-5018	1020	O5/O6	3	1	-16	16
dRV14	IRAS 16177-5018	271	B2/B3	1	2	33	10
dRV15	IRAS 16177-5018	271	B2/B3	2	1	16	8
dRV16	IRAS 16177-5018	405	O5/O6	1	1	-2	11
dRV17	IRAS 16571-4029	820	O9/B1	1	2	32	6
dRV18	IRAS 17149-3916	895	O5/O6	1	1	1	10
dRV19	IRAS 17258-3637	1558	O9/B1	1	2	6	8
dRV20	IRAS 17258-3637	378	O9/B1	1	2	-95	12
dRV21	IRAS 18006-2422	770	O9/B1	1	2	-13	15
dRV22	IRAS 18449-0158	319	O5/O6	1	1	-29	24
dRV23	IRAS 18449-0158	319	O5/O6	2	2	-30	24
dRV24	IRAS 18507+0110	262	O5/O6	1	1	-35	14
dRV25	IRAS 18507+0110	373	B2/B3	1	1	-24	24
dRV26	IRAS 18507+0110	373	B2/B3	2	1	-59	18
dRV27	IRAS 18507+0110	389	B2/B3	1	1	-2	10

Table 5.3: Results of the Radial Velocity Cross-Correlation. Column 7 shows the radial velocity change relative to the first epoch measurements, while the other columns provide the ID of the relative measurements, the name of the IRAS source, the number of the stars, estimated spectral types, night of the second epoch in the second observing run and the formal error of the fit.

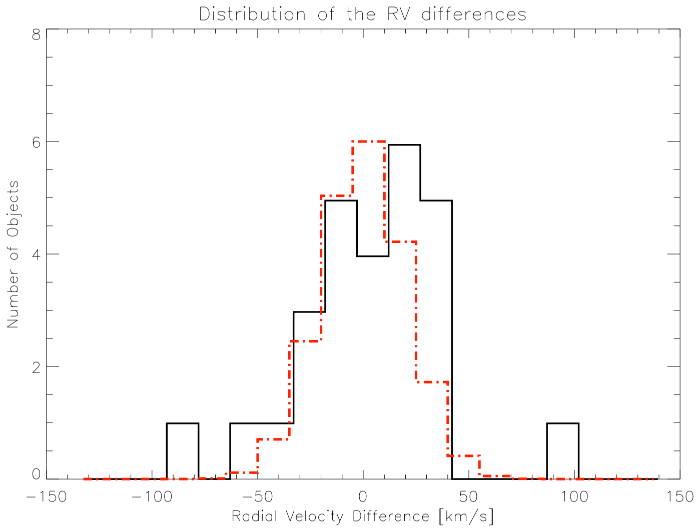

Figure 5.20: Histogram of the observed radial velocity differences of the systems at different epochs plotted with the solid black line. The two outliers are very good candidates for being close binary stars. The dot-dashed red line indicates a hypothetic distribution of a single star population observed with a normally distributed measurement error 20 km/s.

constraints are valid for star # 411. However, # 411 being an even more massive star, explaining the large ΔRV requires a companion more massive or on a shorter-period orbit than that of star # 378.

5.5.2 Binary Population

The standard deviation of the full sample's RV-differences is ∼34.5 km/s, significantly larger than the mean error of the RV-fits. The much larger variation of the RVs indicate intrinsically varying RVs for the targets. We note, that the observations of Bosch et al. (2001) yielded an identical, ∼35 km/s dispersion in the radial velocity of the massive stars in R136 to what our multi-epoch, multi-cluster survey finds. The conclusion of the survey of Bosch et al. (2001) was that the dynamics of the massive stars is dominated by the presence of close binaries.

In order to find out if our results are consistent with the combination of a population of dominantly single massive stars and the observational errors, we overplot the expected curve in Fig. 5.20. The curve has been calculated as the density of 3×10^5 random numbers following a normal distribution with a standard deviation of 20 km/s, our estimate for the typical measurement errors. For the comparison purposes the density has been scaled to the maximum of the observations.

The observational results histogram suffers from the relatively low number of measurements, but several differences from the overplotted single star population can be noted. First, due to the two objects with very high RV-variations, the wings of the observed populations are significantly broader than those of the overplotted case. Second, the observations make a double-peaked distribution more probable than a single-peaked one.

To quantitatively compare the probability that the two populations are drawn from the same sample we applied the two-sided Kolmogorov-Smirnov (K-S) test. The K-S test is working with unbinned data and compares the maximum value of the absolute difference between the two cumulative distribution functions (Press et al. 2002). The K-S test estimates that there is 66% chance that our observations are not consistent with the assumption of the population of single stars, i.e. a significant binary star population has to be considered. We note here, that our error estimates in Sect. 5.4.5 are upper limits with the assumption that the four quasi-simultaneously observed stars are *not close binaries*. If this assumption fails, our actual observational errors are closer to the formal error estimates of ∼14 km/s. This smaller error, in turn would increase the confidence level of a required close binary population to 97%.

In order to constrain the required binarity rate and binary parameters, we are developing a more sophisticated modelling tool. The Monte-Carlo simulation creates synthetic mixed populations of single and binary stars, with masses randomly chosen according to the probability density given by the Salpeter initial mass function, random inclinations and random epochs. A normally distributed error is added to each simulated RV-measurement. Finally, the simulated populations will be compared to the observed radial velocities using the K-S test.

5.6 Conclusions

Our multi-epoch spectroscopic survey tests whether massive stars inside or close to ultracompact H II regions show radial velocity variation indicative of a massive companion. Our 27 relative RV-measurements show a broad ΔRV-distribution, with similar standard deviation ($\sigma \sim 35$ km/s) as was found by the single-epoch optical spectroscopy of the starburst cluster R 136 (Bosch et al. 2001).

We identify an O5/O6 and an O9/B1 spectral type star displaying RV-variations as large as ∼90 km/s and show that they must be close massive binary stars. The observed ΔRV distribution of the population is compared to what is expected from a population of single stars observed with the estimated upper limit errors. We find that the probability of the ΔRV distribution being dominated by a single star population is lower than ∼23% and can be as low as 2.6%.

Thus, a significant rate of close binary stars among the young massive stars is needed to explain the observations. These results are also consistent with RV-surveys of older, optically visible massive stars, where the binarity rate can be as high as ∼80%. This consistency demonstrates that the binarity rate is very probably an intrinsic property of massive stars, characteristic to their formation processes.

We note, that the coalescence scenario proposed by (Bonnell et al. 1998) naturally favors the formation of close, nearly equal-mass massive binaries. The detection of failed stellar mergers among massive stars in or close to ultracompact H II regions is the first strong observational support for the coalescence scenario.

Chapter 6

Summary

In this thesis we studied the environment of young stars aiming to deepen our understanding of the role and properties of stellar companions, disks and envelopes. While the first two chapters deal with low- and intermediate-mass young stars, Chapters 4 and 5 investigate massive young stars.

In Chapter 2 we present observations of the face-on circumstellar disk of a classical young Solar-type star. The target is the 8 Myr-old TW Hya, the closest of such stars. We obtained near-infrared images using the adaptive optics system NACO on ESO's Very Large Telescope in combination with a new technique, the polarimetric differential imaging. The differential imaging allowed us to detect light scattered from the disk as close as $\sim 0.1''$ from the central star. The previous closest detection was $\sim 0.4''$ by HST coronographic imaging. We derived the first Ks-band radial polarized intensity distribution between $0.5''$ and $1.4''$, which resembles well the shorter wavelengths surface brightness distribution. We confirmed the previously reported gradual slope change around $0.8''$. Our observations probed the disk material at $\sim$6 AU, very close to radius of the predicted planet-induced gap. These results provide the sharpest yet look into the disk of a typical young low-mass star at the planet-forming stage. The observations also demonstrate the potential of the new polarimetric differential imaging technique at 8m-class telescopes to map the inner regions of protoplanetary disks at linear scales of our inner Solar System.

In Chapter 3 we present results from our high-resolution, high-contrast imaging campaign targeting 1-4 Myr-old stars in the Taurus-Auriga and Orion star-forming regions. The targets are mainly intermediate-mass Herbig Ae and Be stars, but include also lower-mass objects of particular importance. The observations, conducted using the ALFA adaptive optics system at the 3.5 m telescope of the Calar Alto Observatory, led to the discovery of six new companion candidates and the near-infrared detection of circumstellar envelopes. We identified companion candidates to several interesting objects, including the Herbig Be star V 380 Cep. A new companion candidate has been identified very close to V 372 Ori, the youngest Vega-type star. The most exciting discovery is probably the companion candidate of FU Ori, the prototype of poorly understood outburst stars. The presence of a companion provides support for the theories explaining the outburst by enhanced disk accretion rates induced by the gravitational perturbations of a companion. We also imaged scattered light around the low-mass star SU Aur and the Herbig Ae star AB Aur. On the basis of the morphology and the scale of these emission we argue that we detected light scattered on the dust in the circumstellar envelopes. The cone-shaped emission by SU Aur resembles outflow cavities identified around several other young stars. We will pursue Fabry-Perot imaging to confirm the existence and to determine the direction of the outflow. The near-infrared images of the envelope of AB Aur is consistent with the white-light Hubble Space Telescope coronographic images and provide previously missing color information.

We also used the NACO adaptive optics system to take the highest resolution yet near-infrared images of the closest Herbig Ae star HD 104237. Our images confirm the recent discovery of an association of young stars around HD 104237. The images prove for the first time that circumstellar disks are also present around some of the faint sources, which are likely to be T Tauri stars. Our observations formed a crucial part of an international, multi-instrument campaign characterizing this new association: we found that the cluster is 5 Myr old, being the closest young association after the less concentrated and somewhat older TW Hya association. Thus, follow-up studies of these new disks will provide a unique snapshot in the disk evolution and planet-formation process at the 5 Myr-old stage.

Chapter 4 focuses on the observations of the typical environment of a new-born massive star discussing observations of the nearby star-forming region IRAS 09002-4732. The complexity of the region requires an approach different from the ones previously used: we complemented the high-resolution, sensitive ISAAC/VLT near-infrared broad and narrow-band imagery with mid-infrared imaging and spectroscopy, as well as with single-dish millimetre observations. The near-infrared view of the region identifies a strongly reddened rich cluster of young stars, many of them displaying significant infrared excess emission. We showed that the stellar density increases towards the ultracompact H II region G268.42-0.85, in which we were able to unambiguously identify the near-infrared counterpart of the new-born massive star, its ionizing source. The mid-infrared data proves that this star is the main heating source of the region, as well as the primary source illuminating the large southern lobe of the reflection nebulosity. In the foreground of the reflection nebulosity we identified several very long and confined dust filaments and denser globules embedded in these filaments. Different methods are applied to estimate the spectral type of the ionizing star which we found to be of spectral type O9 with one sub-class accuracy.

We explored the direct vicinity of the massive star at sub-arcsecond resolutions between 1 and 20 μm. The images show numerous very red objects and we are able to prove that at least one elongated object is heated externally by the massive star. We compiled the most complete spectral energy distribution of the region, as well as dust mass estimates from our millimetre observations. Finally, we provided the first structural, global model for the star-forming region taking all major components into account.

Chapter 5 reports on our survey of very young OB-stars aiming to identify spectroscopic binary stars. The radial velocity variations are widely used for binary searches in the optical regime and we apply it for the first time on embedded massive stars at near-infrared wavelengths. We present 28 relative radial velocity measurement of 16 objects and identify two of them as close, massive binaries. The multi-epoch observations show a relative radial velocity distribution significantly broader than what results from the observational inaccuracies. We argue, that the dynamics of these very young massive stars are dominated by the presence of close, massive binaries. These findings are consistent with results on optically visible, older massive stars proving that the high binarity rate is an intrinsic property of massive stars and not the result of dynamical evolution of the close clusters. Such a high intrinsic binarity rate can naturally be explained by the coalescence scenario of massive star formation but not with current simulations of accretion via massive disks.

Bibliography

Alves, J. F., Lada, C. J., and Lada, E. A. (2001). Internal structure of a cold dark molecular cloud inferred from the extinction of background starlight. *Nature*, 409:159–161.

Apai, D., Henning, T., and Stecklum, B. (2002). High-Resolution Near-IR Study of Regions of Massive Star Formation. In *ASP Conf. Ser. 267: Hot Star Workshop III: The Earliest Phases of Massive Star Birth*, page 337.

Apai, D., Linz, H., Stecklum, B., and Henning, T. (2004a). An Infrared Portait of the Star-forming Region IRAS 09002-4732: Visiting a Far-infrared Lighthouse. *submitted to Astronomy and Astrophysics.*

Apai, D., Pascucci, I., Brandner, W., Henning, T., Lenzen, R., Potter, D. E., Lagrange, A.-M., and Rousset, G. (2004b). NACO polarimetric differential imaging of TW Hya. A sharp look at the closest T Tauri disk. *Astronomy and Astrophysics*, 415:671–676.

Apai, D., Pascucci, I., Brandner, W., Wang, H., and Henning, T. (2003). Adaptive Optics Imaging of Circumstellar Disks. In *Proc. IAU Symposium no. 211.*

Bachiller, R. (1996). Bipolar Molecular Outflows from Young Stars and Protostars. *Annual Review of Astronomy and Astrophysics*, 34:111–154.

Bally, J. (2002). Observational Constraints on the Formation of Massive Stars. In *ASP Conf. Ser. 267: Hot Star Workshop III: The Earliest Phases of Massive Star Birth*, page 219.

Bally, J., Devine, D., and Sutherland, R. (1995). Externally Illuminated Young Stellar Objects in the Orion Nebula. In *Revista Mexicana de Astronomia y Astrofisica Conference Series*, page 19.

Baraffe, I., Chabrier, G., Allard, F., and Hauschildt, P. H. (1998). Evolutionary models for solar metallicity low-mass stars: mass-magnitude relationships and color-magnitude diagrams. *Astronomy and Astrophysics*, 337:403–412.

Bell, K. R. and Lin, D. N. C. (1994). Using FU Orionis outbursts to constrain self-regulated protostellar disk models. *Astrophysical Journal*, 427:987–1004.

Bessell, M. S. and Brett, J. M. (1988). JHKLM photometry - Standard systems, passbands, and intrinsic colors. *Publications of the Astronomical Society of the Pacific*, 100:1134–1151.

Bibo, E. A. and The, P. S. (1991). The type of variability of Herbig Ae/Be stars. *Astronomy and Astrophysics Supplement Series*, 89:319–334.

Bik, A., Kaper, L., Hanson, M. M., Comerón, F., and Smits, M. (2004). High resolutions K-band spectroscopy of the deeply embedded ionizing sources of UCHII regions. *to be submitted to Astronomy and Astrophysics.*

Blondel, P. F. C., Talavera, A., and Djie, H. R. E. T. A. (1993). Lyman alpha emission in spectra of Herbig AE stars - an indication of accretion? *Astronomy and Astrophysics*, 268:624–640.

Blum, J., Wurm, G., Kempf, S., Poppe, T., Klahr, H., Kozasa, T., Rott, M., Henning, T., Dorschner, J., Schräpler, R., Keller, H. U., Markiewicz, W. J., Mann, I., Gustafson, B. A., Giovane, F., Neuhaus, D., Fechtig, H., Grün, E., Feuerbacher, B., Kochan, H., Ratke, L., El Goresy, A., Morfill, G., Weidenschilling, S. J., Schwehm, G., Metzler, K., and Ip, W.-H. (2000). Growth and Form of Planetary Seedlings: Results from a Microgravity Aggregation Experiment. *Physical Review Letters*, 85:2426–2429.

Boccaletti, A., Augereau, J.-C., Marchis, F., and Hahn, J. (2003). Ground-based Near-Infrared Imaging of the HD 141569 Circumstellar Disk. *Astrophysical Journal*, 585:494–501.

Bonnell, I. and Bastien, P. (1992). A binary origin for FU Orionis stars. *Astrophysical Journal Letters*, 401:L31–L34.

Bonnell, I. A. (2002). The Formation of Massive Stars through Stellar Collisions. In *ASP Conf. Ser. 267: Hot Star Workshop III: The Earliest Phases of Massive Star Birth*, page 193.

Bonnell, I. A., Bate, M. R., and Zinnecker, H. (1998). On the formation of massive stars. *Monthly Notices of the Royal Astronomical Society*, 298:93–102.

Bonnell, I. A. and Davies, M. B. (1998). Mass segregation in young stellar clusters. *Monthly Notices of the Royal Astronomical Society*, 295:691.

Bosch, G., Selman, F., Melnick, J., and Terlevich, R. (2001). The ionising cluster of 30 Doradus. IV. Stellar kinematics. *Astronomy and Astrophysics*, 380:137–141.

Brand, J., Blitz, L., and Wouterloot, J. G. A. (1986). The velocity field of the outer Galaxy in the Southern Hemisphere. I - Catalogue of nebulous objects. *Astronomy and Astrophysics Supplement Series*, 65:537–550.

Brandner, W., Zinnecker, H., Alcalá, J. M., Allard, F., Covino, E., Frink, S., Köhler, R., Kunkel, M., Moneti, A., and Schweitzer, A. (2000). Timescales of Disk Evolution and Planet Formation: HST, Adaptive Optics, and ISO Observations of Weak-Line and Post-T Tauri Stars. *Astronomical Journal*, 120:950–962.

Braz, M. A., Gregorio Hetem, J. C., Scalise, E., Monteiro Do Vale, J. L., and Gaylard, M. (1989). Search for water vapor masers in the direction of IRAS sources associated with H II regions and molecular clouds. *Astronomy and Astrophysics Supplement Series*, 77:465–469.

Calvet, N., D'Alessio, P., Hartmann, L., Wilner, D., Walsh, A., and Sitko, M. (2002). Evidence for a Developing Gap in a 10 Myr Old Protoplanetary Disk. *Astrophysical Journal*, 568:1008–1016.

Casali, M. M. and Hawarden, T. G. (1992). Technical report, JCMT Newsletter, 3:33.

Caswell, J. L. and Haynes, R. F. (1987). Southern H II regions - an extensive study of radio recombination line emission. *Astronomy and Astrophysics*, 171:261–276.

Chernin, A. D., Efremov, Y. N., and Voinovich, P. A. (1995). Superassociations: violent star formation induced by shock-shock collisions. *Monthly Notices of the Royal Astronomical Society*, 275:313–326.

Churchwell, E. (1991). Newly Formed Massive Stars. In *NATO ASIC Proc. 342: The Physics of Star Formation and Early Stellar Evolution*, page 221.

Clarke, C. J. and Syer, D. (1996). Low-mass companions to T Tauri stars: a mechanism for rapid-rise FU Orionis outbursts. *Monthly Notices of the Royal Astronomical Society*, 278:L23–L27.

Corporon, P. and Lagrange, A.-M. (1999). A search for spectroscopic binaries among Herbig Ae/Be stars. *Astronomy and Astrophysics Supplement Series*, 136:429–444.

Cutri, R. M., Skrutskie, M. F., van Dyk, S., Beichman, C. A., Carpenter, J. M., Chester, T., Cambresy, L., Evans, T., Fowler, J., Gizis, J., Howard, E., Huchra, J., Jarrett, T., Kopan, E. L., Kirkpatrick, J. D., Light, R. M., Marsh, K. A., McCallon, H., Schneider, S., Stiening, R., Sykes, M., Weinberg, M., Wheaton, W. A., Wheelock, S., and Zacarias, N. (2003). 2MASS All Sky Catalog of point sources. *VizieR Online Data Catalog*, 2246.

D'Angelo, G., Kley, W., and Henning, T. (2003). Orbital Migration and Mass Accretion of Protoplanets in Three-dimensional Global Computations with Nested Grids. *Astrophysical Journal*, 586:540–561.

Duquennoy, A. and Mayor, M. (1991). Multiplicity among solar-type stars in the solar neighbourhood. II - Distribution of the orbital elements in an unbiased sample. *Astronomy and Astrophysics*, 248:485–524.

Duquennoy, A., Mayor, M., and Halbwachs, J.-L. (1991). Multiplicity among solar type stars in the solar neighbourhood. I - CORAVEL radial velocity observations of 291 stars. *Astronomy and Astrophysics Supplement Series*, 88:281–324.

Egan, M. P., Price, S. D., Moshir, M. M., and et al. (1999). Msx5c infrared point source catalog. Technical report, Air Force Research Lab., AFRL-VS-TR-1999-1522.

Elmegreen, B. G. (1991). The Origin and Evolution of Giant Molecular Clouds. In *NATO ASIC Proc. 342: The Physics of Star Formation and Early Stellar Evolution*, page 35.

Feldt, M., Stecklum, B., Henning, T., Hayward, T. L., Lehmann, T., and Klein, R. (1998). The ultracompact H II region G45.45+0.06. A pearl necklace in the sky. *Astronomy and Astrophysics*, 339:759–772.

Fitzpatrick, M. (1994). A GUI for the IRAF Radial Velocity Task FXCOR. In *ASP Conf. Ser. 61: Astronomical Data Analysis Software and Systems III*, page 79.

Furniss, I., Jennings, R. E., and Moorwood, A. F. M. (1975). 40-350 micron observations of galactic sources. *Astrophysical Journal*, 202:400–406.

García, B. and Mermilliod, J. C. (2001). High-mass binaries in the very young open cluster NGC 6231. Implication for cluster and star formation. *Astronomy and Astrophysics*, 368:122–136.

Ghosh, S. K., Mookerjea, B., Rengarajan, T. N., Tandon, S. N., and Verma, R. P. (2000). Far infrared observations of the southern Galactic star forming complex around IRAS 09002-4732. *Astronomy and Astrophysics*, 363:744–754.

Gies, D. R. (1987). The kinematical and binary properties of association and field O stars. *Astrophysical Journal Supplement Series*, 64:545–563.

Grady, C. A., Pérez, M. R., Bjorkman, K. S., and Massa, D. (1999a). Transient Infall Events in the Disk of AB Aurigae: The beta Pictoris Phenomenon at 2-4 Megayears. *Astrophysical Journal*, 511:925–931.

Grady, C. A., Woodgate, B., Bruhweiler, F. C., Boggess, A., Plait, P., Lindler, D. J., Clampin, M., and Kalas, P. (1999b). Hubble Space Telescope Space Telescope Imaging Spectrograph Coronagraphic Imaging of the Herbig AE Star AB Aurigae. *Astrophysical Journal Letters*, 523:L151–L154.

Grady, C. A., Woodgate, B., Torres, C. A. O., Henning, T., Apai, D., Wang, H., Rodmann, J., Stecklum, B., Linz, H., and Williger, G. (2004). The Environment of the Herbig Ae Star HD 104237. *Astrophysical Journal, in press.*

Graves, J. E., Northcott, M. J., Roddier, F. J., Roddier, C. A., Potter, D., O'Connor, D. J., Rigaut, F. J., and Chun, M. R. (2000). First light for Hokupa'a 36 on Gemini North. In *Proc. SPIE Vol. 4007, p. 26-30, Adaptive Optical Systems Technology, Peter L. Wizinowich; Ed.*, pages 26–30.

Gullbring, E., Hartmann, L., Briceno, C., and Calvet, N. (1998). Disk Accretion Rates for T Tauri Stars. *Astrophysical Journal*, 492:323.

Hanson, M. M., Conti, P. S., and Rieke, M. J. (1996). A Spectral Atlas of Hot, Luminous Stars at 2 Microns. *Astrophysical Journal Supplement Series*, 107:281.

Hartmann, L. (2002). Flows, Fragmentation, and Star Formation. I. Low-Mass Stars in Taurus. *Astrophysical Journal*, 578:914–924.

Hartmann, L. and Kenyon, S. J. (1985). On the nature of FU Orionis objects. *Astrophysical Journal*, 299:462–478.

Hartmann, L. and Kenyon, S. J. (1996). The FU Orionis Phenomenon. *Annual Review of Astronomy and Astrophysics*, 34:207–240.

Hartung, M., Bizenberger, P., Boehm, A., Laun, W., Lenzen, R., and Wagner, K. (2000). First test results and calibration methods of CONICA as a stand-alone device. In *Proc. SPIE Vol. 4008, Optical and IR Telescope Instrumentation and Detectors, Masanori Iye; Alan F. Moorwood; Eds.*, pages 830–841.

Henning, T., Launhardt, R., Stecklum, B., and Wolf, S. (2002). Continuum Polarization as a Tool: A Perspective for VLT and ALMA. In *The Origins of Stars and Planets: The VLT View. Proceedings of the ESO Workshop held in Garching, Germany, 24-27 April 2001, p. 79.*, page 79.

Henning, T., Pfau, W., and Altenhoff, W. J. (1990). Infrared and radio emission from very young and massive stellar objects. *Astronomy and Astrophysics*, 227:542–552.

Herbig, G. H. (1966). On the interpretation of FU orionis. *Vistas in Astronomy*, 8:109–125.

Herbig, G. H. (1977). Eruptive phenomena in early stellar evolution. *Astrophysical Journal*, 217:693–715.

Hester, J. J., Scowen, P. A., Sankrit, R., Lauer, T. R., Ajhar, E. A., Baum, W. A., Code, A., Currie, D. G., Danielson, G. E., Ewald, S. P., Faber, S. M., Grillmair, C. J., Groth, E. J., Holtzman, J. A., Hunter, D. A., Kristian, J., Light, R. M., Lynds, C. R., Monet, D. G., O'Neil, E. J., Shaya, E. J., Seidelmann, K. P., and Westphal, J. A. (1996). Hubble Space Telescope WFPC2 Imaging of M16: Photoevaporation and Emerging Young Stellar Objects. *Astronomical Journal*, 111:2349.

Hillenbrand, L. A. (1997). On the Stellar Population and Star-Forming History of the Orion Nebula Cluster. *Astronomical Journal*, 113:1733–1768.

Hillenbrand, L. A. and Hartmann, L. W. (1998). A Preliminary Study of the Orion Nebula Cluster Structure and Dynamics. *Astrophysical Journal*, 492:540.

Hillenbrand, L. A., Strom, S. E., Vrba, F. J., and Keene, J. (1992). Herbig Ae/Be stars - Intermediate-mass stars surrounded by massive circumstellar accretion disks. *Astrophysical Journal*, 397:613–643.

Hippler, S., Glindemann, A., Kasper, M., Kalas, P., Rohloff, R., Wagner, K., Looze, D. P., and Hackenberg, W. K. (1998). ALFA: the MPIA/MPE adaptive optics with a laser for astronomy project. In *Proc. SPIE Vol. 3353, p. 44-55, Adaptive Optical System Technologies, Domenico Bonaccini; Robert K. Tyson; Eds.*, pages 44–55.

Hoeg, E., Bässgen, G., Bastian, U., Egret, D., Fabricius, C., Großmann, V., Halbwachs, J. L., Makarov, V. V., Perryman, M. A. C., Schwekendiek, P., Wagner, K., and Wicenec, A. (1997). The TYCHO Catalogue. *Astronomy and Astrophysics*, 323:L57–L60.

Huard, S. (1997). *Polarization of Light.* John Wiley & Sons.

Huélamo, N. and Brandner, W. (2004). Dual Imaging Polarimetry Observations of Circumstellar Disks in TW Hydrae: The NACO View. In *Proc. Toward Other Earth – Darwin/TPF and the Search for Extrasolar Terrestrial Planets, M. Fridlund & Th. Henning; Ed.*

Joint IRAS Science Working Group (1988). Infrared Astronomical Satellite Catalogs, 1988. The Point Source Catalog, version 2.0, NASA RP-1190. In *IRAS Point Source Catalog (1988).*

Kaper, L., Bik, A., Comerón, F., and Hanson, M. M. (2004). A near-infrared survey of southern (ultra-)compact h II regions: a search for the deeply embedded, ionizing young massive stars. *to be sumbitted to Astronomy and Astrophysics.*

Kastner, J. H., Zuckerman, B., Weintraub, D. A., and Forveille, T. (1997). X-ray and molecular emission from the nearest region of recent star formation. *Science*, 277:67–71.

Kawazoe, E. and Mineshige, S. (1993). Unstable accretion disks in FU Orionis stars. *Publications of the Astronomical Society of Japan*, 45:715–725.

Kenyon, S. J., Hartmann, L., Gomez, M., Carr, J. S., and Tokunaga, A. (1993). RNO 1B/1C - A double FU Orionis system. *Astronomical Journal*, 105:1505–1510.

Kenyon, S. J., Hartmann, L., and Hewett, R. (1988). Accretion disk models for FU Orionis and V1057 Cygni - Detailed comparisons between observations and theory. *Astrophysical Journal*, 325:231–251.

Koresko, C. D., Beckwith, S. V. W., Ghez, A. M., Matthews, K., and Neugebauer, G. (1991). An infrared companion to Z Canis Majoris. *Astronomical Journal*, 102:2073–2078.

Krist, J. E., Stapelfeldt, K. R., Ménard, F., Padgett, D. L., and Burrows, C. J. (2000). WFPC2 Images of a Face-on Disk Surrounding TW Hydrae. *Astrophysical Journal*, 538:793–800.

Kuhn, J. R., Potter, D., and Parise, B. (2001). Imaging Polarimetric Observations of a New Circumstellar Disk System. *Astrophysical Journal Letters*, 553:L189–L191.

Kurtz, S., Churchwell, E., and Wood, D. O. S. (1994). Ultracompact H II regions. 2: New high-resolution radio images. *Astrophysical Journal Supplement Series*, 91:659–712.

Lada, C. J. (1999). The Formation of Low Mass Stars: An Observational Overview. In *NATO ASIC Proc. 540: The Origin of Stars and Planetary Systems*, page 143.

Lada, C. J. and Adams, F. C. (1992). Interpreting infrared color-color diagrams - Circumstellar disks around low- and intermediate-mass young stellar objects. *Astrophysical Journal*, 393:278–288.

Lang, K. R. (1991). Springer, Berlin, p. 138.

Lapinov, A. V., Schilke, P., Juvela, M., and Zinchenko, I. I. (1998). Studies of dense cores in regions of massive star formation. VI. Multitransitional CS and CO observations of G 261.64-2.09, G 268.42-0.85, G 270.26+0.83 and G 301.12-0.20. *Astronomy and Astrophysics*, 336:1007–1023.

Lenzen, R. (1991). IR-study of IRAS09002 - 4732 and the surrounding HII region. *Astronomy and Astrophysics*, 244:477–482.

Levato, H. and Abt, H. A. (1976). Spectral types in the ORI nebula cluster. *Publications of the Astronomical Society of the Pacific*, 88:712–714.

Li, W., Evans, N. J., and Lada, E. A. (1997). Looking for Distributed Star Formation in L1630: A Near-Infrared (J, H, K) Survey. *Astrophysical Journal*, 488:277.

Lin, D. N. C. and Papaloizou, J. (1985). On the dynamical origin of the solar system. In *Protostars and Planets II*, pages 981–1072.

Liseau, R., Lorenzetti, D., Nisini, B., Spinoglio, L., and Moneti, A. (1992). Star formation in the VELA molecular clouds. I - The IRAS-bright Class I sources. *Astronomy and Astrophysics*, 265:577–596.

Lissauer, J. J. (1993). Planet formation. *Annual Review of Astronomy and Astrophysics*, 31:129–174.

Lynden-Bell, D. and Pringle, J. E. (1974). The evolution of viscous discs and the origin of the nebular variables. *Monthly Notices of the Royal Astronomical Society*, 168:603–637.

Lynds, B. T. (1962). Catalogue of Dark Nebulae. *Astrophysical Journal Supplement Series*, 7:1.

Malbet, F., Berger, J.-P., Colavita, M. M., Koresko, C. D., Beichman, C., Boden, A. F., Kulkarni, S. R., Lane, B. F., Mobley, D. W., Pan, X. P., Shao, M., van Belle, G. T., and Wallace, J. K. (1998). FU Orionis Resolved by Infrared Long-Baseline Interferometry at a 2 AU Scale. *Astrophysical Journal Letters*, 507:L149–L152.

Manchester, B. A. and Goss, W. M. (1969). An 11 cm map of a region in Vela. *Australian Journal of Physics Astrophysical Supplement*, 11:35.

Mannings, V. and Sargent, A. I. (1997). A High-Resolution Study of Gas and Dust around Young Intermediate-Mass Stars: Evidence for Circumstellar Disks in Herbig AE Systems. *Astrophysical Journal*, 490:792.

Manoj, P., Maheswar, G., and Bhatt, H. C. (2002). Non-emission-line young stars of intermediate mass. *Monthly Notices of the Royal Astronomical Society*, 334:419–425.

Martins, F., Schaerer, D., and Hillier, D. J. (2002). On the effective temperature scale of O stars. *Astronomy and Astrophysics*, 382:999–1004.

Mathis, J. S. (1990). Interstellar dust and extinction. *Annual Review of Astronomy and Astrophysics*, 28:37–70.

McCaughrean, M. J. and O'dell, C. R. (1996). Direct Imaging of Circumstellar Disks in the Orion Nebula. *Astronomical Journal*, 111:1977.

Mekkaden, M. V. (1998). Photometric and polarimetric variability of the isolated T Tauri star TW Hydrae. *Astronomy and Astrophysics*, 340:135–142.

Meyer, M. R., Adams, F. C., Hillenbrand, L. A., Carpenter, J. M., and Larson, R. B. (2000). The Stellar Initial Mass Function: Constraints from Young Clusters, and Theoretical Perspectives. *Protostars and Planets IV*, page 121.

Mezger, P. G. and Henderson, A. P. (1967). Galactic H II Regions. I. Observations of Their Continuum Radiation at the Frequency 5 GHz. *Astrophysical Journal*, 147:471.

Mezger, P. G., Smith, L. F., and Churchwell, E. (1974). IR-excess Radiation and the Absorption Characteristics of Dust in Galactic H II Regions. *Astronomy and Astrophysics*, 32:269.

Millan-Gabet, R., Schloerb, F. P., and Traub, W. A. (2001). Spatially Resolved Circumstellar Structure of Herbig AE/BE Stars in the Near-Infrared. *Astrophysical Journal*, 546:358–381.

Monet, D. G., Levine, S. E., Canzian, B., Ables, H. D., Bird, A. R., Dahn, C. C., Guetter, H. H., Harris, H. C., Henden, A. A., Leggett, S. K., Levison, H. F., Luginbuhl, C. B., Martini, J., Monet, A. K. B., Munn, J. A., Pier, J. R., Rhodes, A. R., Riepe, B., Sell, S., Stone, R. C., Vrba, F. J., Walker, R. L., Westerhout, G., Brucato, R. J., Reid, I. N., Schoening, W., Hartley, M., Read, M. A., and Tritton, S. B. (2003). The USNO-B Catalog. *Astronomical Journal*, 125:984–993.

Moorwood, A. F. (1997). ISAAC: a 1- to 5-um imager/spectrometer for the VLT. In *Proc. SPIE Vol. 2871, Optical Telescopes of Today and Tomorrow; Ed.: Ardeberg, A. L.*, pages 1146–1151.

Natta, A., Grinin, V. P., Mannings, V., and Ungerechts, H. (1997). The Evolutionary Status of UX Orionis-Type Stars. *Astrophysical Journal*, 491:885.

Nyman, L.-Å., Lerner, M., Nielbock, M., Anciaux, M., Brooks, K., Chini, R., Albrecht, M., Lemke, R., Kreysa, E., Zylka, R., Johansson, L. E. B., Bronfman, L., Kontinen, S., Linz, H., and Stecklum, B. (2001). SIMBA explores the southern sky. *The Messenger*, 106:40.

O'dell, C. R. (2001). The Orion Nebula and its Associated Population. *Annual Review of Astronomy and Astrophysics*, 39:99–136.

Ossenkopf, V. and Henning, T. (1994). Dust opacities for protostellar cores. *Astronomy and Astrophysics*, 291:943–959.

Panagia, N. (1973). Some Physical parameters of early-type stars. *Astronomical Journal*, 78:929–934.

Pantin, E., Waelkens, C., and Lagage, P. O. (2000). ADONIS observations of the HD 100546 circumstellar dust disk. *Astronomy and Astrophysics*, 361:L9–L12.

Pascucci, I., Apai, D., Henning, T., Stecklum, B., and Brandl, B. (2004). The hot core – ultracompact H II region connection in G 10.47+0.03. *submitted to Astronomy and Astrophysics.*

Perryman, M. A. C., Lindegren, L., Kovalevsky, J., Hoeg, E., Bastian, U., Bernacca, P. L., Crézé, M., Donati, F., Grenon, M., van Leeuwen, F., van der Marel, H., Mignard, F., Murray, C. A., Le Poole, R. S., Schrijver, H., Turon, C., Arenou, F., Froeschlé, M., and Petersen, C. S. (1997). The HIPPARCOS Catalogue. *Astronomy and Astrophysics*, 323:L49–L52.

Persson, S. E., Murphy, D. C., Krzeminski, W., Roth, M., and Rieke, M. J. (1998). A New System of Faint Near-Infrared Standard Stars. *Astronomical Journal*, 116:2475–2488.

Potter, D. (2003a). Imaging Polarimetry of TW Hya, *submitted to Publications of the Astronomical Society of the Pacific.*

Potter, D. E. (2003b). A search for debris disks with a dual channel adaptive optics imaging polarimeter. *Ph.D. Thesis, Univ. of Hawaii.*

Preibisch, T., Balega, Y., Hofmann, K., Weigelt, G., and Zinnecker, H. (1999). Multiplicity of the massive stars in the Orion Nebula cluster. *New Astronomy*, 4:531–542.

Preibisch, T., Balega, Y. Y., Schertl, D., and Weigelt, G. (2002). High-resolution study of the young stellar objects in Mon R2 IRS 3. *Astronomy and Astrophysics*, 392:945–954.

Press, W. H., Teukolsky, S. A., Vetterling, W. T., and Flannery, B. P. (2002). *Numerical Receipies in C: The Art of Programming.* 2nd Edition, Cambridge University Press.

Racine, R., Walker, G. A. H., Nadeau, D., Doyon, R., and Marois, C. (1999). Speckle Noise and the Detection of Faint Companions. *Publications of the Astronomical Society of the Pacific*, 111:587–594.

Reipurth, B. and Bally, J. (2001). Herbig-Haro Flows: Probes of Early Stellar Evolution. *Annual Review of Astronomy and Astrophysics*, 39:403–455.

Reipurth, B., Nyman, L.-A., and Chini, R. (1996). Protostellar candidates in southern molecular clouds. *Astronomy and Astrophysics*, 314:258–264.

Reipurth, B., Yu, K., Heathcote, S., Bally, J., and Rodríguez, L. F. (2000). Hubble Space Telescope NICMOS Images of Herbig-Haro Energy Sources: [Fe II] Jets, Binarity, and Envelope Cavities. *Astronomical Journal*, 120:1449–1466.

Robberto, M., Song, J., Beckwith, S. V. W., and Panagia, N. (2003). A HST Study of Mass Accretion Rates in the Trapezium Cluster. In *Proc. IAU Symposium no. 211.*

Rodes, J. J., Bernabeu, G., and Fabregat, J. (1998). Radial Velocity Measurements with FXCOR. *Astrophysics and Space Science*, 263:259–262.

Rodriguez, L. F., D'Alessio, P., Wilner, D. J., Ho, P. T. P., Torrelles, J. M., Curiel, S., Gomez, Y., Lizano, S., Pedlar, A., Canto, J., and Raga, A. C. (1998). Compact protoplanetary disks around the stars of a young binary system. *Nature*, 395:355–357.

Romaniello, M., Robberto, M., and Panagia, N. (2004). Low-Mass Pre-Main Sequence Stars in the Large Magellanic Cloud - III: Accretion Rates from HST-WFPC2 Observations. *ArXiv Astrophysics e-prints.*

Rousselot, P., Lidman, C., Cuby, J.-G., Moreels, G., and Monnet, G. (2000). Night-sky spectral atlas of OH emission lines in the near-infrared. *Astronomy and Astrophysics*, 354:1134–1150.

Rousset, G., Lacombe, F., Puget, P., Hubin, N. N., Gendron, E., Fusco, T., Arsenault, R., Charton, J., Feautrier, P., Gigan, P., Kern, P. Y., Lagrange, A., Madec, P., Mouillet, D., Rabaud, D., Rabou, P., Stadler, E., and Zins, G. (2003). NAOS, the first AO system of the VLT: on-sky performance. In *Proc. SPIE, Vol. 4839, Adaptive Optical System Technologies II. Ed. Wizinowich, P. L.; Bonaccini, D.*, pages 140–149.

Schaerer, D. and de Koter, A. (1997). Combined stellar structure and atmosphere models for massive stars. III. Spectral evolution and revised ionizing fluxes of O3-B0 stars. *Astronomy and Astrophysics*, 322:598–614.

Schaerer, D., Meynet, G., Maeder, A., and Schaller, G. (1993). Grids of stellar models. II - From 0.8 to 120 solar masses at Z = 0.008. *Astronomy and Astrophysics Supplement Series*, 98:523–527.

Schneider, G., Smith, B. A., Becklin, E. E., Koerner, D. W., Meier, R., Hines, D. C., Lowrance, P. J., Terrile, R. J., Thompson, R. I., and Rieke, M. (1999). NICMOS Imaging of the HR 4796A Circumstellar Disk. *Astrophysical Journal Letters*, 513:L127–L130.

Schneider, S. and Elmegreen, B. G. (1979). A catalog of dark globular filaments. *Astrophysical Journal Supplement Series*, 41:87–95.

Selman, F., Melnick, J., Bosch, G., and Terlevich, R. (1999). The ionizing cluster of 30 Doradus. III. Star-formation history and initial mass function. *Astronomy and Astrophysics*, 347:532–549.

Shu, F. H. (1977). Self-similar collapse of isothermal spheres and star formation. *Astrophysical Journal*, 214:488–497.

Shu, F. H. (1991). The Formation of Low Mass Stars: Theory. In *NATO ASIC Proc. 342: The Physics of Star Formation and Early Stellar Evolution*, page 365.

Siebenmorgen, R., Krügel, E., and Spoon, H. W. W. (2004). *Astronomy and Astrophysics, in press.*

Simpson, J. P. and Rubin, R. H. (1990). IRAS low-resolution spectral observations of H II regions. *Astrophysical Journal*, 354:165–183.

Skinner, S. L. and Walter, F. M. (1998). ASCA Observations of the T Tauri Star SU Aurigae and the Surrounding L1517 Dark Cloud. *Astrophysical Journal*, 509:761–767.

Spangler, C., Sargent, A. I., Silverstone, M. D., Becklin, E. E., and Zuckerman, B. (2001). Dusty Debris around Solar-Type Stars: Temporal Disk Evolution. *Astrophysical Journal*, 555:932–944.

Stecklum, B., Henning, T., Feldt, M., Hayward, T. L., Hoare, M. G., Hofner, P., and Richter, S. (1998). The ultracompact H II region G5.97-1.17 - an evaporating circumstellar disk in M8. *Astronomical Journal*, 115:767.

Stecklum, B., Henning, T. F. E., Apai, D., and Linz, H. (2003). VLT-ISAAC observations of massive star-forming regions. In *Proc. SPIE, Vol. 4834, Discoveries and Research Prospects from 6- to 10-Meter-Class Telescopes II. Ed. Guhathakurta, P.*, pages 337–344.

Steinacker, J. and Henning, T. (2003). Detection of Gaps in Circumstellar Disks. *Astrophysical Journal Letters*, 583:L35–L38.

Stetson, P. B. (1987). DAOPHOT - A computer program for crowded-field stellar photometry. *Publications of the Astronomical Society of the Pacific*, 99:191–222.

Testi, L., Palla, F., and Natta, A. (1999). The onset of cluster formation around Herbig Ae/Be stars. *Astronomy and Astrophysics*, 342:515–523.

van den Ancker, M. E., de Winter, D., and Tjin A Djie, H. R. E. (1998). HIPPARCOS photometry of Herbig Ae/Be stars. *Astronomy and Astrophysics*, 330:145–154.

Walsh, A. J., Burton, M. G., Hyland, A. R., and Robinson, G. (1998). Studies of ultracompact HII regions - II. High-resolution radio continuum and methanol maser survey. *Monthly Notices of the Royal Astronomical Society*, 301:640–698.

Wang, H., Apai, D., Henning, T., and Pascucci, I. (2004). FU Orionis: A Binary Star? *Astrophysical Journal Letters*, 601:L83–L86.

Webb, R. A., Zuckerman, B., Platais, I., Patience, J., White, R. J., Schwartz, M. J., and McCarthy, C. (1999). Discovery of Seven T Tauri Stars and a Brown Dwarf Candidate in the Nearby TW Hydrae Association. *Astrophysical Journal Letters*, 512:L63–L67.

Weferling, B., Reichertz, L. A., Schmid-Burgk, J., and Kreysa, E. (2002). Principles of the data reduction and first results of the fastscanning method for (sub)millimeter astronomy. *Astronomy and Astrophysics*, 383:1088–1099.

Wegner, W. (1994). Intrinsic Colour Indices of OB Supergiants Giants and Dwarfs in the UBVRIJHKLM System. *Monthly Notices of the Royal Astronomical Society*, 270:229.

Weinberger, A. J., Becklin, E. E., Schneider, G., Chiang, E. I., Lowrance, P. J., Silverstone, M., Zuckerman, B., Hines, D. C., and Smith, B. A. (2002). Infrared Views of the TW Hydra Disk. *Astrophysical Journal*, 566:409–418.

Weingartner, J. C. and Draine, B. T. (2001). Dust Grain-Size Distributions and Extinction in the Milky Way, Large Magellanic Cloud, and Small Magellanic Cloud. *Astrophysical Journal*, 548:296–309.

Whitney, B. A. and Hartmann, L. (1992). Model scattering envelopes of young stellar objects. I - Method and application to circumstellar disks. *Astrophysical Journal*, 395:529–539.

Wichmann, R., Bastian, U., Krautter, J., Jankovics, I., and Rucinski, S. M. (1998). HIPPARCOS observations of pre-main-sequence stars. *Monthly Notices of the Royal Astronomical Society*, 301:L39.

Wolfire, M. G. and Cassinelli, J. P. (1987). Conditions for the formation of massive stars. *Astrophysical Journal*, 319:850–867.

Wood, D. O. S. and Churchwell, E. (1989). Massive stars embedded in molecular clouds - Their population and distribution in the galaxy. *Astrophysical Journal*, 340:265–272.

Wouterloot, J. G. A. and Brand, J. (1989). IRAS sources beyond the solar circle. I - CO observations. *Astronomy and Astrophysics Supplement Series*, 80:149–187.

Yorke, H. W. (2002). Theory of Formation of Massive Stars via Accretion. In *ASP Conf. Ser. 267: Hot Star Workshop III: The Earliest Phases of Massive Star Birth*, page 165.

Yorke, H. W. and Bodenheimer, P. (1999). The Formation of Protostellar Disks. III. The Influence of Gravitationally Induced Angular Momentum Transport on Disk Structure and Appearance. *Astrophysical Journal*, 525:330–342.

Yorke, H. W. and Kruegel, E. (1977). The dynamical evolution of massive protostellar clouds. *Astronomy and Astrophysics*, 54:183–194.

Yorke, H. W. and Sonnhalter, C. (2002). On the Formation of Massive Stars. *Astrophysical Journal*, 569:846–862.

Zinchenko, I., Mattila, K., and Toriseva, M. (1995). Studies of dense molecular cores in regions of massive star formation. II. CS J=2-1 survey of southern H_2_O masers in the longitude range l=260-310deg. *Astronomy and Astrophysics Supplement Series*, 111:95.

Zinnecker, H. and Bate, M. R. (2002). Multiplicity of Massive Stars – a Clue to their Origin? In *ASP Conf. Ser. 267: Hot Star Workshop III: The Earliest Phases of Massive Star Birth*, page 209.

Zinnecker, H. and Preibisch, T. (1994). X-ray emission from Herbig Ae/Be stars: A ROSAT survey. *Astronomy and Astrophysics*, 292:152–164.

Zuckerman, B. (2001). Dusty Circumstellar Disks. *Annual Review of Astronomy and Astrophysics*, 39:549–580.

Acknowledgement

Completing my research and shaping the results into a homogenous thesis took about three and a half years, which I spent partly in Jena and partly in Heidelberg, far from my family and my old friends. Living and working in a foreign country is never easy, but there were many people whose support, help and friendship have made this experience a nice memory.

I am thankful for many of my friends both in Jena and Heidelberg. I am especially indebted to some of them: László Veisz for his purely rational situation analysis and infinite curiosity; Igor Tóth and Zsófia Herbert for their help; Belen López-Marti for the ”group therapies” and for the help after my eye accident; Jürgen Weiprecht for the jenaer tea-breaks; Hendrik Linz, for camping through the deserts of the Northern Territory and the forests of Sächsischer Schweiz; Dmitry Semenov for the sixteen whiskeys in the Theatercafee. Roland Vavrek was the person who was always ready to help with any problems or questions I had, whether it was a faulty random number generator or a steaming car engine. Hongchi Wang for being the quickest of my collaborators; Arjan Bik for the Dutch pancakes and for taking the risk that Rens Waters catches him secretly reading the draft of my thesis.

And of course the ”Coffee-people” of the MPIA: Sebastiano Ligori, Nadine Haering, Jakob Walcher, Olivier Chesnau, Elena Puga, Joana Costa, Carlos Alvarez, Jens Rodmann, Boris Hausler, Johny Setiawan, who were a reliable daily source of jokes, sympathy, the freshest rumors and a lot of noise.

The help and advices of Carol Grady on the ”dark side of science” like job search and scientific survival proved to be crucial and I am deeply thankful to her.

I would also like to acknowledge the professional support of Wolfgang Brandner: it is rare to find someone with such a broad knowledge and willingness to help to other people.

I was impressed and motivated by the professional dedication of Kees Dullemond and Antonella Natta — two people who just love doing science.

During the first two years I often visited the Thüringer Landessternwarte in Tautenburg, whose staff – both the scientists and the technical personnel – welcomed me warmly. I would especially like to mention Bringfried Stecklum, Eike Günther and Artie Hatzes.

Thanks is also due to people who supported the scientific research in the ”background”. The most important aspect – after the cantines, which I do not discuss here – is the computer department, which provided competent, quick and friendly service in AIU Jena, TLS Tautenburg and MPIA Heidelberg. Special thanks for Jürgen Weiprecht, Uli Hiller and Frank Richter.

Half of my research period was made possible by the financial support of the German Academic Exchange Office (DAAD), while my original visit was funded by the ERASMUS program. It is not possible to overestimate the importance of such international exchange programs and I am indebted to them.

I thank Prof. Matthias Bartellmann and Prof. Thomas Henning for refereeing my thesis, as well as Markus Feldt for helping with the German translation of the abstract.

I am thankful for my supervisor Prof. Thomas Henning for his help and guidance during

these years. I found motivating his interest for every field of astronomy. Being the busiest of all the astronomers I met, it is remarkable that he was also the quickest in reading and correcting any of my drafts repeatedly. I benefited from his astrophysical expertise, optimism and I am thankful for providing me the tools and the opportunity to work on some of the most exciting, although rather diverse topics of astronomy.
This work could have hardly been completed without the strong support of my family in Budapest, Szeged and Civitanova Marche. Special thanks goes to Vincenzo and Daniela for understanding our enthusiasm for this profession and enduring the long periods far from Ilaria and me. I found it very kind, that Daniela and Valeria even translated our first paper to Italian. I am most thankful for my parents, who were always there, when I needed them. The long telephone discussions with them helped me through on countless physical or moral problems.
Finally, I thank my wife and best collaborator Ilaria Pascucci. All details will be forwarded personally.